DEVELOPMENT OF A SINGLY-RESONANT OPTICAL PARAMETRIC OSCILLATOR FOR CARBON CYCLE SCIENCE

by

Briana Lynn Jones

A thesis submitted in partial fulfillment
of the requirements for the degree

of

Master of Science

in

Electrical Engineering

MONTANA STATE UNIVERSITY
Bozeman, Montana

November, 2015

©COPYRIGHT

by

Briana Lynn Jones

2015

All Rights Reserved

ACKNOWLEDGMENTS

The completion of this thesis was not a product of my work alone, but a combination of the effort from many wonderful people who helped me find success in this project. I am grateful to everyone who made this chapter of my life such an enriching experience. I am fortunate to have Dr. Kevin Repasky as a mentor and my advisor for this research project. This project would not have been possible without him and I owe so much of the success of this work to him. My co-advisor, Dr. Phil Battle, taught me so much about the experimental side of nonlinear optics. I am grateful for his patience, support, and enthusiasm for this project. He gave me the opportunity to work with the talented people at AdvR, Inc., including Dr. Matt Bigelow who also had an important role in this project. Additionally I would like to thank Dr. John Carlsten and Dr. Joe Shaw for being a part of my committee and helping me see the broad applications of this work. And finally, I want to thank my family for their continued support throughout my education. In particular my husband, Lucas, for helping me stay strong when I doubted myself, and my sisters, Alyssa and Courtney, for giving me guidance and support to get through graduate school.

Funding Acknowledgment

This work was kindly supported by AdvR, Inc., whose expertise in nonlinear optics and production of the periodically-poled nonlinear crystals used in this research helped make this project a success. Additional support was provided by the Montana space grant consortium.

TABLE OF CONTENTS

1. INTRODUCTION 1

Climate Change and Methane 1
DIAL 3
DIAL Laser Transmitter 7

2. THEORY 9

Introduction to Nonlinear Optics 9
Qualitative Description of Nonlinear Interactions 9
Mathematical Description of Nonlinear Interactions 10
Derivation of Nonlinear Optical Processes from Maxwell's Equations 14
Solutions for Optical Parametric Amplification 17
Non-depleted Pump 18
Phase-matching 19
Depleted Pump 23
Solutions for Optical Parametric Oscillation 27
Modeling Nonlinear Proceeses 28
Comparison of Matlab Numerical Integration to SNLO Model 29

3. OPTICAL PARAMETRIC AMPLIFICATION 32

Methods and Setup 32
Results 37

4. LOCKING THE OPO CAVITY 48

Dither Locking Theory 50
Methods for Dither Locking 56
Results from the Locking System 60
Limitations of the System and Future Work 62

5. OPTICAL PARAMETRIC OSCILLATOR 64

Methods and Setup 64
Results 70
Measured and Expected Cavity Transmission 70
Cavity FSR Plot with Comparison to Theory 70
Unseeded Unlocked OPO Data with OPG Comparison 72

TABLE OF CONTENTS - CONTINUED

Seeded Unlocked OPO Data..... 75
Seeded Locked OPO Data with OPA Data Comparison 76

6. CONCLUSION 89

REFERENCES CITED 92

APPENDIX A: Matlab OPA Program 94

LIST OF FIGURES

Figure Page

1.1 Atmospheric methane concentrations from NOAA's monitoring station at Mauna Loa. Data in blue represent seasonal changes in the methane concentration and the data in red represent the yearly averages. Pre-industrial era concentrations averaged around 715 pbb, with the most recent data indicating that concentrations have exceeded 1800 ppb, indicating that the increase is driven by human activity. 2

1.2 DIAL return signals at the online (red) and offline (blue) wavelengths from a CO_2 DIAL. Range is determined from travel time of the online and offline pulses. Initial data are used for background subtraction that assists in calibration of the system. The difference between the online and offline return signals can be used to determine the concentration of the molecule of interest as a function of distance from the system. 4

1.3 CO_2 concentration map created using a DIAL system. The two-dimensional plot was created by taking one-dimensional data across another spatial dimension. The measured spatial concentration of CO_2 is superimposed over a map from where the data were collected. Blue represents low concentrations of CO_2 and red represents high concentrations. 6

1.4 Methane absorption lines near 1.65 μm from the HITRAN database, which are ideal for methane DIAL measurements. 8

2.1 Virtual energy level diagram for OPG. At its most basic, the OPG process breaks down a pump photon and two longer wavelength photons are created, one called the signal and one called the idler. 13

2.2 Signal, pump, and idler outputs from OPA produced in Matlab using the coupled wave equations (see Appendix A). Figure (a) shows the signal and idler outputs that increase exponentially at low pump energies. Figure (b) shows a larger range of input pump energies and full depletion of the pump near 20 mJ, illustrating the limitations of the non-depleted pump approximation. 25

LIST OF FIGURES - CONTINUED

Figure Page

2.3 Comparison of the signal output from OPA in the depleted and non-depleted pump approximation. Figure (a) shows the output from the OPA model in the case of a depleted pump input. Notice that the output signal energy reaches a peak value then begins to drop due to the conversion process working in reverse. Figure (b) shows the OPA signal output in the non-depleted pump approximation. The signal energy reaches unrealistic values where it gains significantly more energy than the input pump, demonstrating why the non-depleted pump approximation is only valid for small pump inputs. Figure (c) shows both the depleted and non-depleted pump solutions plotted together. It is evident that the two results begin to diverge from each other near 25 mJ of pump energy, and various factors determine where this divergence occurs. Figure (d) shows the difference between the two solutions. 26

2.4 Image of the SNLO interface for modeling the output from OPA for a 2D (gaussian) beam. A plane wave was modeled by setting the radius of curvature of the beams to very large values in order to compare the SNLO model to the numerical integration of the coupled wave equations. 30

2.5 Comparison of the Matlab program to SNLO for OPA with the same parameters for each of the waves at the output. As seen in figures (a) and (b), the outputs for each of the programs are slightly different but follow the same trend. In figure (c), the pump output calculated with each program shows no discernible difference between the two methods. Overall, the two methods provide comparable results. 31

3.1 Setup for the OPA and OPG measurements. Note that for the OPG measurements, the seed laser is turned off. The half-wave plate and polarizer in the pump beam path are used to adjust the pump energy. For the highest conversion in OPA, the pump and seed beams need to be collinear within the crystal. Two Pellin-Broca prisms (one shown) after the crystal separate the signal beam from the pump beam and any other generated wavelengths. 33

LIST OF FIGURES - CONTINUED

Figure Page

3.2 Gaussian beam profile and image of pump beam at the focus. 34

3.3 The nonlinear crystal is shown inside the brass heater. The heater completely encloses the crystal except the input and output faces in order to ensure minimal temperature gradients within the crystal. 35

3.4 Output spectra showing poor spectral overlap (a), and poor spatial overlap (b). Poor spectral overlap occurs when the peak of the OPG spectrum does not coincide with the peak of the seed laser spectrum. Poor spatial overlap broadens the output OPA spectrum so that it is nearly as broad as the OPG spectrum. Ideally the OPA spectrum should be narrow..... 38

3.5 Output spectra showing good spectral and spatial overlap. The peak of the OPG spectrum (green) coincides with the peak of the seed laser spectrum (red), resulting in a narrow OPA output spectrum (blue). The FWHM of the OPA spectrum is on the order of the measurement resolution of the OSA. 39

3.6 Notice how the OPA spectra in (b) is wider than in (a). This is due to the increased pump energy and the seed power, which isn't high enough to saturate the gain at higher pump energies. Increased seed laser power is expected to make the spectrum narrow again. 40

3.7 OPA and OPG peak power outputs at 41°C and 48°C plotted on a log scale. The OPA output at 41°C, where it is phase-matched, has the largest output of the three. The output from OPA is always larger than OPG since OPA is an amplification process and OPG arises from spontaneous generation. 41

3.8 Use of the plane-wave model to fit to experimental data can create inaccuracies due to the fact that the beam is actually focusing as it propagates through the crystal. Therefore the SNLO model will provide more accurate data since it accounts for focusing of the pump and seed beams. The plot in (b) shows three models from SNLO that are used to estimate d_{eff} and Δk that will be used as inputs for the SNLO model of the OPO. 43

LIST OF FIGURES - CONTINUED

Figure Page

3.9 Output energy for OPA and OPG at high pump energies. These data show the OPG data in blue and the OPA data in green. Notice the relatively large difference between the OPG and OPA output at low energy, which decreases as the pump energy is increased. This is due to the relatively large impact of seeding the crystal at low pump energies. 45

3.10 Conversion efficiency for OPA and OPG at high pump energies. The OPG data are shown in blue and the OPA data are shown in green. As in the output energy plot of figure 3.9, the difference between OPG and OPA is larger at lower energies due to the larger impact of seeding at low pump energies. 46

4.1 Output wavelength of the laser diode as a function of time. The dither signal from the function generator sinusoidally changes the output wavelength of the laser diode at frequency ω_d. 50

4.2 When the cavity is resonant at λ_0, the cavity transmission signal will oscillate at $2\omega_d$ because of the dithering of the laser diode. This is verified by following the sequence of numbers in figure 4.1 and in the left and right images. 51

4.3 When the cavity is off resonance, the cavity transmission signal will oscillate at ω_d. In this case, where $\lambda > \lambda_0$ the cavity transmission signal is in phase with the dither signal. 53

4.4 Again when the cavity is off-resonance, the cavity transmission signal oscillates at ω_d, however since $\lambda < \lambda_0$, the output is out of phase with the dither signal. This is useful because we can determine the side of the resonant peak where λ_o is located. 54

4.5 Error signal as a function of cavity resonance. Notice when the cavity is resonant at λ_0 ($\lambda = \lambda_0$) the error signal is zero. Inspection of the previous images reveals that in order for the locking system to be able to maintain resonance, the wavelength must stay within the shaded region, which corresponds to $\Delta\lambda$ of less than the half width of the resonance feature. 55

LIST OF FIGURES - CONTINUED

Figure Page

4.6 Block diagram of the dither locking setup for the OPO. The seed laser operates at 1654 nm and the wavelength is dithered with an AOM and function generator. One mirror of the cavity is mounted on a PZT for fine adjustment of the cavity length. The signal transmitted through the cavity is measured on an InGaAs detector. This information is sent to a lock-in amplifier which extracts the amplitude of signals oscillating at the dither frequency to create the error signal. The error signal is proportional to the cavity length change required to keep the cavity on resonance at 1654 nm. 56

4.7 Image of the packaged shutter circuit with the connections for the locking circuit. The circuit is powered with a standard power supply and three coaxial connectors are used for the inputs and outputs, which include the Q-switch (input), detector signal (input), and the corrected cavity transmission signal (output) which is used as the input to the lock-in amplifier. 58

4.8 Output from the shutter circuit with a sine wave input. The circuit triggers on the Q-switch pulse (blue) and the output from the shutter circuit (green) holds the input at the value that occured at the start of the Q-switch pulse. The amount of time that the output is held at this value depends on the resistance and capacitance in the circuit. This plot shows that the shutter circuit works as expected. 59

4.9 As the cavity length is changed by changing the PZT voltage (green) the cavity transmission (blue) moves through a resonant feature. The cavity begins off-resonance, then to the side of the resonant feature, through zero (which indicates the peak of the resonant feature), to the other side of the resonant feature, and finally back to zero where it is off-resonance again. 61

LIST OF FIGURES - CONTINUED

Figure Page

4.10 Test of the locking system showing the cavity transmission and PZT voltage over a long time scan with external disturbances. The cavity transmission (blue) starts off-resonance and quickly moves to its maximum value, indicating it is on-resonance. With external disturbances like touching a mirror mount or pressing on the optical table, the locking circuit is able to recover and maintain locking. 62

5.1 Image of the OPO cavity. The flat mirror (right) is mounted on a PZT and has nominally 95% reflectivity at the signal wavelength. The output mirror (left) is a curved mirror with radius of curvature 0.5 m and 45% reflectivity at the signal wavelength. The nonlinear crystal is enclosed in a brass heater (center) with only the input and output faces of the crystal exposed. 66

5.2 Block diagram of the OPO setup. The Nd:YAG laser at 1064 nm is the pump for the OPO and a glan-laser polarizer and half wave-plate are used to set the energy. The pump beam is focused into the optical cavity with the goal of matching the seed laser profile. A DFB diode laser at 1654 nm is used as the seed laser, which passes through an AOM to modulate the wavelength for the locking circuit. The beam is focused into the cavity with the goal of matching the lowest-order mode of the cavity. The Mg:PPLN crystal is located inside the cavity and a PZT is mounted onto one of the cavity mirrors for the locking circuit. A Pellin-Broca prism separates the outputs from the OPO by wavelength and a filter is used to ensure all pump light is extinguished. A beamsplitter sends 30% of the signal beam to the locking circuit with the remainder used for measurements of the OPO performance. 67

LIST OF FIGURES - CONTINUED

Figure Page

5.3 Image of the full setup used for the OPO measurements. The pump and seed lasers are located on the left side of the image, along with the controls for the lasers and the crystal heater. Various optical components, shown in more detail in figure 5.2, direct the beams to the OPO cavity, pictured near the center of the image. Prisms and filters separate the various output beams by wavelength so that only the signal wavelength is measured at the output, shown on the right side of the image. 69

5.4 Cavity transmission from the OPO cavity with the seed laser coupled. The smaller peaks in the plot indicate imperfect coupling and the seed laser resonating at modes other than the lowest-order mode. Ideal coupling would result in a cavity transmission plot that only included the tallest peaks. 71

5.5 Measured cavity transmission from the OPO plotted with the theoretical cavity transmission from the Airy function. The theoretical cavity transmission shows what the output would look like if only the lowest-order mode was resonant in the OPO cavity. 71

5.6 Spectrum from the unseeded unlocked OPO with pump energy of 1.5 mJ. Since the signal wavelength in an unseeded OPO is generated through spontaneous emission, the output is broadband..... 72

5.7 Spectrum from the unseeded unlocked OPO with pump energy of 2.5 mJ. The spectrum shown here is much broader than the spectrum in figure 5.6 due to the increased pump energy. 73

5.8 Unseeded unlocked OPO spectrum with 2.5 mJ pump energy and OPG spectrum with 2.8 mJ pump energy. The crystal temperature for OPG is 42°C and 44°C for the OPO. Both spectra show the bandwidth of signal wavelengths that can be generated based on phase-matching. 74

5.9 Unseeded unlocked OPO and OPG output energy. The OPO energy is about two times larger than the OPG energy, indicating that the optical cavity is causing an increase in output energy. 75

LIST OF FIGURES - CONTINUED

Figure Page

5.10 Seeded unlocked OPO spectrum. The output is narrower at the center than the unseeded OPO, but is still broad because the cavity is not locked and therefore the cavity length can change due to temperature fluctuations. Here the pump energy is 2.5 mJ and the FWHM of the OPO spectrum is 0.16 nm 76

5.11 Seeded locked OPO output (blue), unseeded unlocked OPO output (green), and seed laser (red) spectrum. The pump energy into the OPO for both the seeded locked and unseeded unlocked output spectra is 1.5 mJ. By locking the OPO cavity, a very narrow spectral output can be achieved. The FWHM of the seeded OPO spectrum is 0.096nm, which is near the 0.06 nm resolution of the OSA. 77

5.12 Seeded locked OPO output (blue), unseeded unlocked OPO output (green), and seed laser (red) spectrum. The pump energy into the OPO for both the seeded locked and unseeded unlocked output spectra is 2.5 mJ. The FWHM of the unseeded OPO is 1 nm larger than in figure 5.11 because of the increased pump energy. The FWHM of the seeded OPO is the same as in figure 5.11 at 0.096 nm, which is near the 0.06 nm resolution of the OSA. 77

5.13 Seeded locked OPO output (blue), unseeded unlocked OPO output (green), and seed laser (red) spectrum. The pump energy into the OPO for both the seeded locked and unseeded unlocked output spectra is 4.5 mJ. Both the seeded and unseeded OPO spectra are broader at this higher pump energy. Here the unseeded OPO FWHM is 2.304 nm and the seeded OPO FWHM is 0.120 nm. 78

5.14 Seeded locked OPO output (blue), unseeded unlocked OPO output (green), and seed laser (red) spectrum. The pump energy into the OPO for both the seeded locked and unseeded unlocked output spectra is 7 mJ. The seeded OPO spectrum is beginning to broaden like the unseeded OPO spectrum. Higher seed power is necessary to keep the seeded OPO spectrum narrow. 78

LIST OF FIGURES - CONTINUED

Figure Page

5.15 Seeded OPO spectrum shown with poor spatial overlap of the seed and pump beams. The result of poor spatial overlap is seen in the seeded locked OPO spectrum (blue), where the side mode suppression is small. Good spatial overlap would result in a narrow output at the seed laser wavelength. In this case however, there is good spectral overlap since the peak of the unseeded OPO spectrum (green) coincides with the peak of the seed laser spectrum (red). 79

5.16 Seeded locked OPO spectrum exhibiting poor spectral overlap. The peak of the unseeded unlocked OPO spectrum (not shown) does not line up with the peak of the seed laser spectrum, resulting in a seeded locked OPO spectrum that has a broad side feature. The asymmetry in the seeded locked OPO spectrum demonstrates the poor spectral overlap in the setup. 80

5.17 Inputs for the SNLO modeling program for 2D gaussian beam mixing in an OPO cavity. The supplied parameters were determined with the best measured and estimated data from the system. The values for d_{eff} and Δk were found from the best-fit to the OPA data from chapter 3. 81

5.18 Measured output signal energy as a function of input pump energy for the three OPO's. The SNLO model is also shown as the solid line. Initially the seeded locked OPO has the highest output energy, but at higher input pump energies it has the lowest output energy. This is likely due to the broadening of the spectra at higher pump energies, which may be corrected with a higher-power seed laser. The SNLO model is about two times larger than the measured outputs, which is reasonable since SNLO assumes a best-case output based on the supplied parameters. 82

LIST OF FIGURES - CONTINUED

Figure Page

5.19 Measured conversion efficiency of the unseeded unlocked OPO, seeded unlocked OPO, and seeded locked OPO compared to the SNLO model. Conversion efficiency was calculated from the data from figure 5.18. Here we see the SNLO conversion efficiency reaches about 16% and the experimental results reach about 8%, which is reasonable since SNLO provides a best-case output. 83

5.20 Seeded locked OPO spectrum (blue) and OPA spectrum (green). The FWHM of each spectrum is on the order of the measurement resolution. Note that the seed laser power for OPA is 4.5 mW and only 1 mW for the OPO, which may indicate that the OPO requires less seed power to achieve a narrow spectrum. The input pump energy for the OPO is 2.5 mJ and is 2.75 mJ for the OPA. 84

5.21 Measured output energy from the seeded locked OPO (red) and the OPA (blue). The OPO output energy is about two times greater than the OPA energy, indicating that the optical cavity leads to increased conversion at the signal wavelength. 85

5.22 Measured conversion efficiency of the seeded locked OPO and the OPA, taken from the data in chapter 3. The conversion efficiency of the OPO reaches a maximum near 7% and levels out, while the OPA conversion efficiency reaches a maximum near 4%. Higher input pump energies are necessary to determine the maximum level that the OPA can achieve. 86

5.23 Optical damage to the PPLN crystal in an OPO. The input pump energy was about 15 mJ when the damage occured. 87

ABSTRACT

The human impact on the global carbon cycle is affecting the health of the environment by changing the balance between incoming and outgoing radiation as well as altering other geochemical cycles such as the nitrogen and water cycles. Although carbon dioxide makes up most of the greenhouse gas emissions, methane has a much greater impact on climate change due to its warming potential on a per molecule basis. Improved understanding of the spatial distribution of methane is necessary to quantify the anthropogenic impacts and mitigate future damage. A differential absorption lidar (DIAL) is proposed for spatially mapping methane concentrations. The system requires a laser transmitter that can produce over 3 mJ of pulse energy with a repetition rate of 1 kHz and output wavelength of 1.654 μm as well as a narrow linewidth on the order of 3 MHz. Modeling predicts that a system with these specifications can achieve measurement error of less than 2% relative to ambient levels of methane. Laser sources with these specifications are not commercially available, and the goal of this work is to evaluate the potential for a singly-resonant optical parametric oscillator (OPO) for the DIAL laser transmitter. The OPO is based on large-aperture periodically-poled magnesium-oxide-doped lithium niobate as the nonlinear optical material. Results from the OPO indicate that energies on the order of 1 mJ are possible with the experimental setup presented when operating at 20 Hz repetition rate. The OPO produced a linewidth of 10.5 GHz, measured on a system with resolution of 6.6 GHz. Future work includes optimization of the OPO to increase the output energy from the system to 3 mJ by improving mode-matching into the cavity and increasing the energy into the system. Additionally a method to precisely measure the linewidth of the OPO output is necessary as well as a pump laser that operates at 1 kHz to test the performance of the OPO at 1 kHz. The initial results show promise for the use of the OPO as the DIAL laser transmitter and with improvements, the OPO should meet the requirements for the DIAL system.

INTRODUCTION

Climate Change and Methane

Methane (CH_4) is the second most prevalent long-lived greenhouse gas, making up approximately 10% of the total greenhouse gas emissions as of 2013 with carbon dioxide (CO_2) making up 82% of the total, according to the EPA [1]. With carbon dioxide making up the majority of the long-lived greenhouse gas emissions, much effort has been put into researching and measuring CO_2's effect on climate change and the carbon cycle in general. Because of this interest, there is a lot of certainty of the sources and sinks of CO_2 and the concentration of CO_2 in the atmosphere. However, the same cannot be said about methane. Comparing CO_2 and CH_4 emissions on the basis of quantity alone indicates that CO_2 has a greater impact on climate change. However if we also take into account how effectively each gas can retain heat, and therefore increase surface temperatures, it is evident that methane's impact is much higher than carbon dioxide's on a per molecule basis [2].

Radiative efficiency is a measure of how much energy a molecule re-radiates back into space on a part per billion (ppb) basis relative to how much energy is incident on the earth's atmosphere, measured in units of $Wm^{-2}ppb^{-1}$. A positive number indicates a net increase in energy and therefore a net temperature increase, while a negative number indicates a net loss in energy. According to the IPCC fourth assessment [2], the radiative efficiency of methane is $3.7*10^{-4}$ $Wm^{-2}ppb^{-1}$ and the radiative efficiency of carbon dioxide is $1.4*10^{-5}$ $Wm^{-2}ppb^{-1}$. The relative impact on climate change due to the warming properties of the two molecules indicates that methane has a 25 times greater impact on climate change than carbon dioxide

on a per molecule basis. Therefore, understanding methane emissions is crucial to understanding climate change.

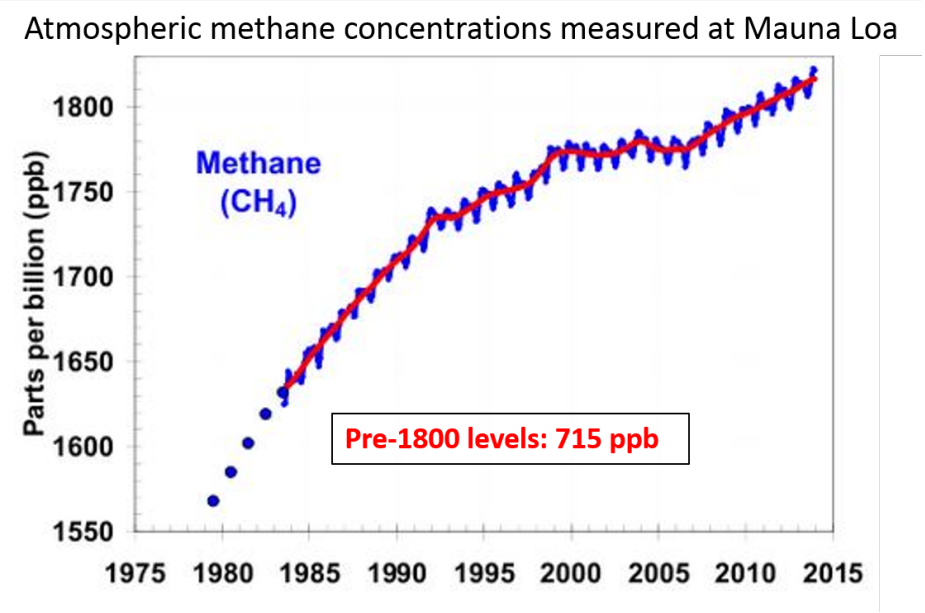


Figure 1.1: Atmospheric methane concentrations from NOAA's monitoring station at Mauna Loa. Data in blue represent seasonal changes in the methane concentration and the data in red represent the yearly averages. Pre-industrial era concentrations averaged around 715 pbb, with the most recent data indicating that concentrations have exceeded 1800 ppb, indicating that the increase is driven by human activity.

Methane emissions are produced by both natural and human-caused (anthropogenic) sources. The largest natural source of methane is wetlands, and other sources include oceans and termites that produce methane [2]. Pre-industrial era measurements of methane sources suggest that natural sources made up over 80% of the total methane emissions while research into present-day sources indicates that at least 60% of methane emissions are anthropogenic [2]. Data from NOAA's monitoring station at Mauna Loa [3] shown in figure 1.1 indicate that atmospheric methane levels have been steadily increasing since the 1980's. The blue data represent the seasonal methane concentrations and the red data represent the yearly average, reaching a

peak above 1800 ppb around the year 2015. Compared to the pre-industrial era levels of around 715 ppb [2], it is clear that levels have been rising, indicating that the increase is driven by human activity. Therefore, mitigation efforts should focus primarily on anthropogenic sources.

The data in figure 1.1 show in situ measurements, which are direct samples of atmospheric concentrations of methane at a specific location on earth. Although many stations like the one at Mauna Loa exist across the globe, the network is insufficient for precisely understanding the sources and sinks of methane. Ideally a system that can measure spatial distributions of methane concentrations would provide the most useful information for this measurement. Some of these systems exist [4,5], but they lack the precision needed to measure the concentrations of atmospheric methane. Improvements to instruments capable of spatial-resolved measurements are necessary for understanding the sources and sinks of methane.

DIAL

In situ measurements, like the data from NOAA at Mauna Loa, make precision measurements of methane concentrations in the atmosphere, but they lack information on the spatial distribution. Another method is with passive satellites, which can be employed to map the spatial distribution of methane; however, they provide column-integrated measurements that lack detail about concentrations at the earth's surface. Additionally, passive satellites have poor spatial resolution in the lower atmosphere where measurements of methane concentrations are needed for determining sources and sinks. The method we propose for making this spatial measurement of methane concentrations with sufficient precision at the earth's surface is called differential absorption lidar (DIAL).

DIAL is a form of active remote sensing that uses two closely-spaced laser wavelengths to increase measurement precision and decrease calibration times. One of the laser wavelengths, called the online wavelength, is centered on an absorption feature of the molecule of interest, in this case methane. The other laser wavelength, called the offline, has a wavelength that is very close to the online wavelength but where the molecule has negligible absorption. Light from the online and offline wavelengths are emitted from the DIAL system in pulses in order to determine the distance traveled based on the return times. A comparison of the online and offline return signals can be used to determine the concentration of the molecule of interest along the path of travel. These data produce a measurement of concentrations as a function of distance from the DIAL system.

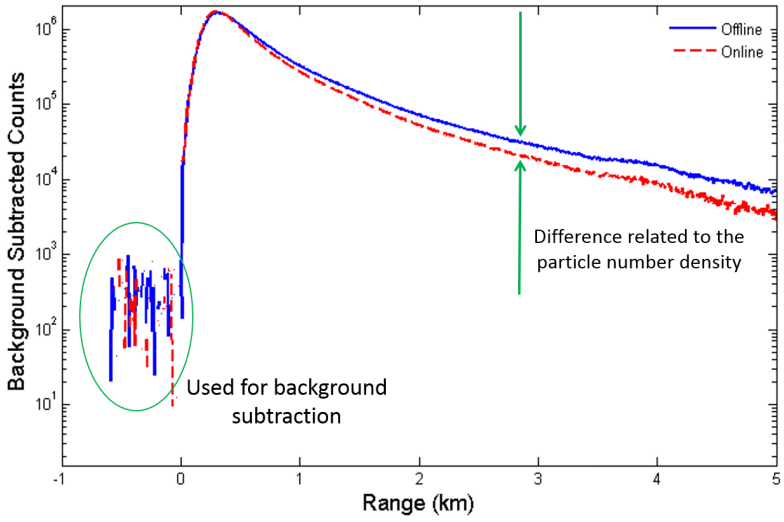


Figure 1.2: DIAL return signals at the online (red) and offline (blue) wavelengths from a CO_2 DIAL. Range is determined from travel time of the online and offline pulses. Initial data are used for background subtraction that assists in calibration of the system. The difference between the online and offline return signals can be used to determine the concentration of the molecule of interest as a function of distance from the system.

The plot in figure 1.2 shows data from a CO_2 DIAL system. Data shown as a solid line represents the offline return signals and the data in the dashed line represent the online return signals. When a concentration of the molecule of interest is located along the line of sight of the DIAL instrument, the online return signal will be smaller than the offline return signal due to absorption along the path by the concentration of molecules. The difference between the online and offline returns is proportional to the density of the molecule of interest. Data shown with less than zero range is for calibration of the system prior to the measurement. Range is determined by the time it takes for the return signals to reach the system after the original online or offline pulse leaves the system. This creates a one-dimensional measurement of molecular concentration.

Consider that if the data in figure 1.2 represent the molecular concentration along one spatial dimension, then this measurement could be repeated along another dimension in space to create a two-dimensional concentration map, as shown in figure 1.3. This figure shows the concentration of CO_2 in space, superimposed over a map of the area from which the data were collected, using the same DIAL system data as in figure 1.2. The two-dimensional plot was created by taking one-dimensional data with the system and repeating the measurement at three different angles, in the plane of the page. This creates a two-dimensional profile of the CO_2 concentrations. This is the method we propose for measuring the spatial distribution of methane.

Development of tools for atmospheric remote sensing of methane are just beginning and have long been limited by lack of detectors and lack of high-power lasers at the necessary wavelength. An avalanche photo-diode (APD) is necessary for measuring the return signals from DIAL, and these detectors have only recently become sensitive enough at 1654 nm, the wavelength needed for a methane DIAL. The laser transmitter is the largest limiting factor. Lasers that operate at 1654 nm are

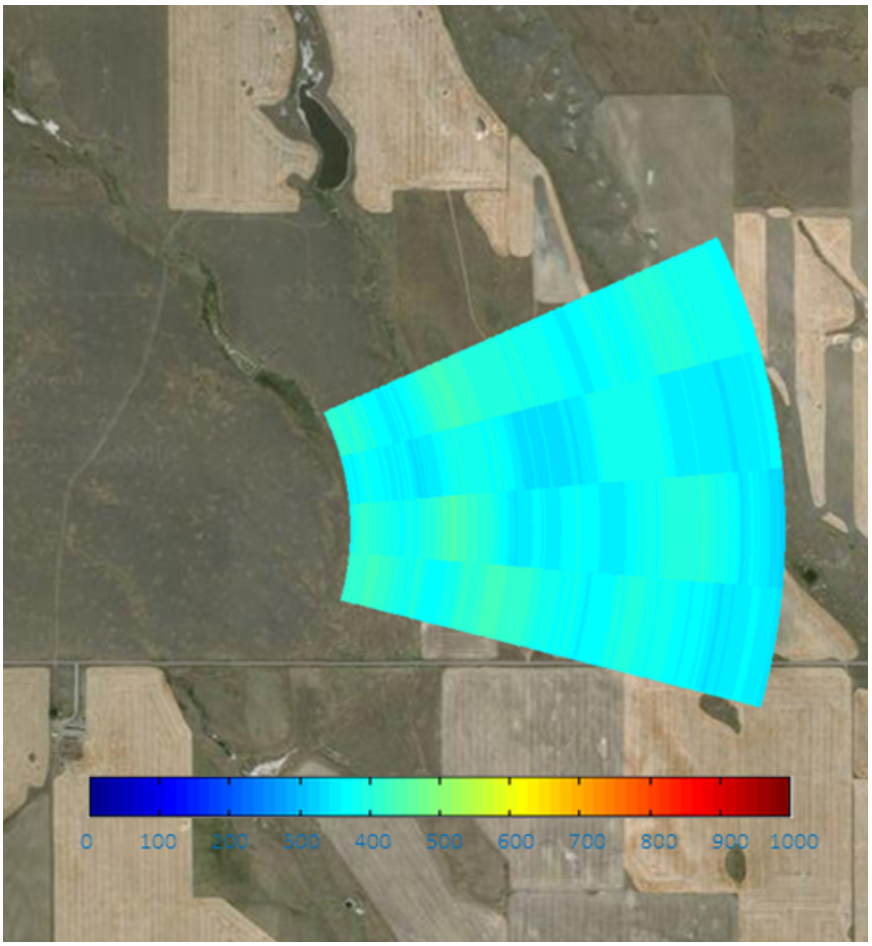


Figure 1.3: CO_2 concentration map created using a DIAL system. The two-dimensional plot was created by taking one-dimensional data across another spatial dimension. The measured spatial concentration of CO_2 is superimposed over a map from where the data were collected. Blue represents low concentrations of CO_2 and red represents high concentrations.

commercially available; however, they do not have all of the specifications required for the methane DIAL. The goal of this research project is to explore the possibility of using a nonlinear frequency conversion technique to produce a laser transmitter for a methane DIAL instrument.

DIAL Laser Transmitter

Modeling indicates that a DIAL system for atmospheric methane detection can operate at 1654 nm, where methane has strong absorption features that do not overlap with water vapor lines or other common absorption lines [6]. For fast integration times, the laser transmitter must have a high repetition rate, on the order of 1 kHz. To get the necessary precision in the measurements, the laser transmitter needs a high-power output, and when pulsed the laser needs about 3 mJ of pulse energy to meet this requirement [7]. The detector system must be sensitive enough to measure small, time-resolved return signals. Figure 1.4 shows the absorption features of methane near 1654 nm from the HITRAN database [6]. Absorption is shown normalized, where 1 is complete absorption by the molecule at a given wavelength. These absorption features are narrow, on the order of GHz at the full width at half maximum (FWHM). For simple data processing, a laser line that is much narrower than the absorption feature being targeted is necessary, and ideally on the order of MHz.

Nonlinear optics are employed to develop this laser source with the specifications mentioned previously. This thesis explores the initial development of a laser source for a methane DIAL, starting with the theory of nonlinear processes in chapter 2, the results of optical parametric amplification in chapter 3, the technique used to lock an optical cavity in chapter 4, and results from the optical parametric oscillator in chapter 5.

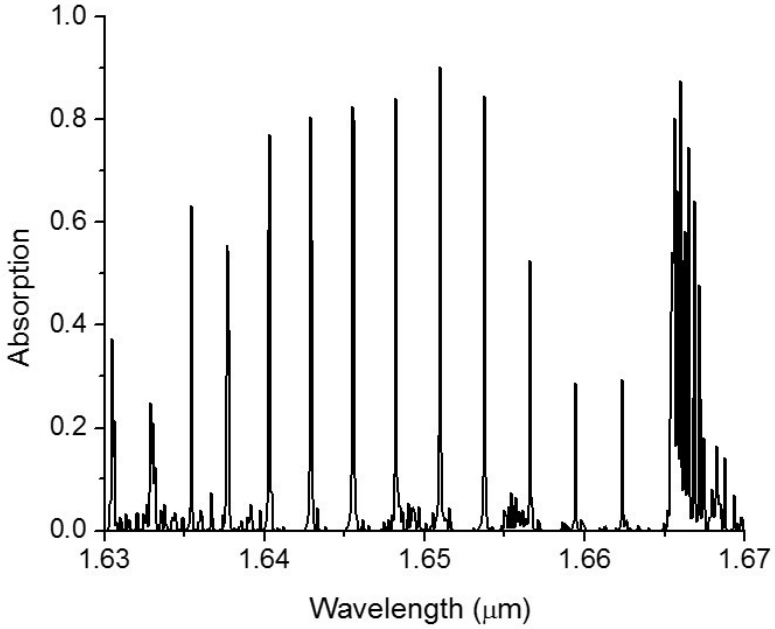


Figure 1.4: Methane absorption lines near 1.65 μm from the HITRAN database, which are ideal for methane DIAL measurements.

THEORY

Introduction to Nonlinear Optics

Nonlinear optics is a branch of optics dealing primarily with optical processes that convert coherent electromagnetic fields from one optical frequency to another optical frequency. This allows one to develop coherent light sources over a broad range of output optical frequencies, from the ultraviolet to the near infrared. The nonlinear optical frequency conversion exploits the nonlinear macroscopic polarization that results from an asymmetric potential well for the electrons bound to heavy nuclei. This asymmetry results in a nonlinear restoring force associated with the bond between the atomic nucleus and the electrons. Only a small subset of materials have the property that allows for nonlinear interactions to occur.

Qualitative Description of Nonlinear Interactions

To see how the nonlinear restoring force can generate new frequencies, consider a mass attached to a spring with a restoring force described by [8]

$$F = -k_1 x \tag{2.1}$$

where k_1 is the spring constant and x is the displacement from equilibrium. This equation can be expanded into a Taylor series to the second order so that

$$F = -k_1 x - k_2 x^2 \tag{2.2}$$

where k_2 is the nonlinear spring constant and $k_2 << k_1$. From Newton's second law, we can write

$$m\frac{d^2x}{dt^2} = -k_1x - k_2x^2 \tag{2.3}$$

Assuming a perturbative solution, where $x = x_1 + x_2 + \textit{higher order terms}$ and $x_2 << x_1$, we can write a series of equations by separating the order of the variable x up to first order so that

$$m\frac{d^2x_1}{dt^2} + k_1x_1 = 0 \tag{2.4a}$$

$$m\frac{d^2x_2}{dt^2} + k_1x_2 = -k_2x_1^2 \tag{2.4b}$$

which can be solved for x_1 and x_2 to obtain

$$x(t) = x_1(t) + x_2(t) = x_0cos(\omega t) + \left(-\frac{k_2x_0^2}{2m\omega^2} + \frac{k_2x_0^2}{6m\omega^2}cos(2\omega t)\right) \tag{2.5}$$

where $\omega^2 = \frac{k_1}{m}$. From this solution we see that the first order perturbation to the restoring force produces a relatively large output that oscillates at ω and a smaller output that oscillates at 2ω.

Mathematical Description
of Nonlinear Interactions

The mass on a spring analogy for nonlinear interactions helps to explain why these interactions can produce new frequencies. But to fully understand the origin of nonlinear optics, we need to model our system starting with Maxwell's equations. The material properties will come into play through the polarization. When the electron in the material is displaced by an electric field, the atom becomes a dipole since the net positive charge from the nucleus is not coincident with the net charge from the

electron cloud. If the electric field interacted with a significant portion of the atoms in the material in the same way, then the material would become polarized.

Following a derivation from Boyd's *Nonlinear Optics* [8], the linear relationship between the polarization of a lossless and dispersionless medium and the applied electric field is

$$P(t) = \epsilon_o \chi_{(1)} E(t) \tag{2.6}$$

where P is the polarization of the material, ϵ_o is the permittivity of free space, $\chi_{(1)}$ is a material constant, and E is the applied electric field. Notice that the polarization, $P(t)$, is linear with respect to the external electric field, $E(t)$. Similar to the treatment of the mass on a spring problem, we can expand the polarization as a Taylor series as follows,

$$\begin{aligned} P(t) =& \epsilon_o \left[\chi_{(1)} E(t) + \chi_{(2)} E^2(t) + \chi_{(3)} E^3(t) + \textit{higher order terms} \right] \\ &= P_{(1)}(t) + P_{(2)}(t) + P_{(3)}(t) + ... \end{aligned} \tag{2.7}$$

where $\chi_{(2)}$, $\chi_{(3)}$, and are the second- and third-order nonlinear susceptibilities, respectively and are material dependent. Most nonlinear materials have $\chi_{(1)} \approx 1$, $\chi_{(2)} \approx 10^{-12} \frac{m}{V}$, and $\chi_{(3)} \approx 10^{-24} \frac{m^2}{V^2}$.

Consider a plane wave incident on a nonlinear material (one in which $\chi_{(2)} \approx 10^{-12} \frac{m}{V}$) that has two distinct frequency components, ω_1 and ω_2. The electric field of this plane wave is described mathematically by

$$E(t) = E_1 e^{-i\omega_1 t} + E_2 e^{-i\omega_2 t} + c.c. \tag{2.8}$$

where $c.c.$ is the complex conjugate. To find the second order nonlinear polarization, $P_{(2)}(t)$, we use

$$P_{(2)}(t) = \epsilon_o \chi_{(2)} E^2(t) \tag{2.9}$$

Inserting equation 2.8 into this expression, we get

$$\begin{aligned} P_{(2)}(t) = \epsilon_o \chi_{(2)} \left[E_1^2 e^{-2i\omega_1 t} + E_2^2 e^{-2i\omega_2 t} + 2E_1 E_2 e^{-i(\omega_1+\omega_2)t} + 2E_1 E_2^* e^{-i(\omega_1-\omega_2)t} + c.c. \right] \\ + 2\epsilon_o \chi_{(2)} \left[E_1 E_1^* + E_2 E_2^* \right] \end{aligned} \tag{2.10}$$

which shows that the nonlinear polarization results in multiple frequencies that were not present in the original plane wave. We can look at each of these individually,

$$P(2\omega_1) = \epsilon_o \chi_{(2)} E_1^2 \tag{2.11a}$$

$$P(2\omega_2) = \epsilon_o \chi_{(2)} E_2^2 \tag{2.11b}$$

$$P(\omega_1 + \omega_2) = 2\epsilon_o \chi_{(2)} E_1 E_2 \tag{2.11c}$$

$$P(\omega_1 - \omega_2) = 2\epsilon_o \chi_{(2)} E_1 E_2^* \tag{2.11d}$$

$$P(0) = 2\epsilon_o \chi_{(2)} (E_1 E_1^* + E_2 E_2^*) \tag{2.11e}$$

along with similar responses at the negative frequencies. From these equations, we can pick out a few common nonlinear processes. Equations 2.11a and 2.11b are second harmonic generation at ω_1 and ω_2, respectively. Equation 2.11c is sum-frequency generation and equation 2.11d is optical parametric amplification, also called difference-frequency generation. Equation 2.11e is optical rectification. One might expect that all these responses could occur simultaneously; however, due to phase-matching (discussed on page 19), generally only one process can occur with reasonable gain for a given set of pumping conditions.

This research focuses solely on optical parametric generation (OPG), optical parametric amplification (OPA), and optical parametric oscillation (OPO). These processes are similar because all of them rely on parametric nonlinear processes. The differences are that OPG starts from spontaneous emission, while OPA is used to amplify a seed laser through the parametric process, and OPO uses an optical cavity to enhance the nonlinear gain. OPG is the most basic of the processes which the other two are built upon. Figure 2.1 shows a virtual energy level diagram for OPG. A pump photon incident on the nonlinear material is converted to a signal photon and idler photon due to the nonlinear polarization. The signal and idler wavelengths are longer than the pump wavelength in order to maintain conservation of energy so that

$$\frac{1}{\lambda_p} = \frac{1}{\lambda_s} + \frac{1}{\lambda_i} \tag{2.12}$$

where λ_p, λ_s, and λ_i are the pump, signal, and idler wavelengths, respectively.

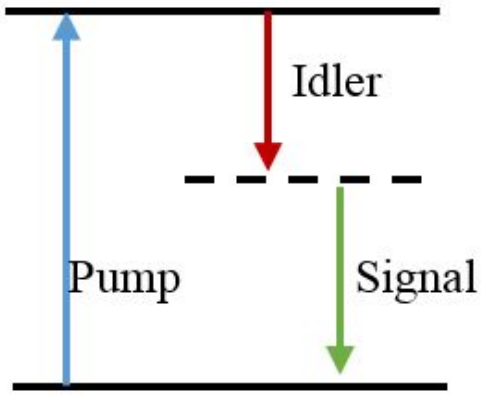


Figure 2.1: Virtual energy level diagram for OPG. At its most basic, the OPG process breaks down a pump photon and two longer wavelength photons are created, one called the signal and one called the idler.

OPG relies on spontaneous generation of the signal and idler photons through conservation of energy, allowing a wide frequency spectrum for both the signal and idler to be generated. OPA is a similar process, but an input beam at the desired signal wavelength is seeded into the crystal to create a preference for the generated wavelength. The seed laser is then amplified via the nonlinear conversion process. OPA is a more efficient process than OPG and has a narrower linewidth dictated by the injection seeding laser, provided the seed laser has enough power to saturate the gain.

An optical parametric oscillator (OPO) uses an optical cavity, created with at least two mirrors, with a nonlinear crystal located inside the cavity acting as the gain medium. The nonlinear conversion process now occurs within the laser cavity and at least one of the wavelengths is resonated and this resonant wavelength will experience an enhanced gain within the optical cavity. OPOs can be seeded or unseeded, where a seeded OPO is like an OPA in that it has an input beam at the signal or idler wavelength in addition to the pump beam, and an unseeded OPO only has the pump beam at the input. Like the OPA, the seeded OPO has a narrower linewidth compared to the unseeded OPO due to the injection seeding.

Derivation of Nonlinear Optical Processes from Maxwell's Equations

To fully understand the mathematics behind nonlinear optics, we need to solve Maxwell's equations with the inclusion of the nonlinear polarization. This will lead to a set of coupled differential wave equations. Following a derivation from Yariv [9], we start with Maxwell's equations in matter,

$$\boldsymbol{\nabla} \cdot \mathbf{E} = \frac{1}{\epsilon_o} \left(\rho_f - \boldsymbol{\nabla} \cdot \mathbf{P} \right) \tag{2.13}$$

$$\boldsymbol{\nabla} \times \mathbf{E} = -\mu_o \frac{\partial}{\partial t} (\mathbf{H} + \mathbf{M}) \tag{2.14}$$

$$\boldsymbol{\nabla} \cdot \mathbf{H} = -\boldsymbol{\nabla} \cdot \mathbf{M} \tag{2.15}$$

$$\boldsymbol{\nabla} \times \mathbf{H} = \mathbf{J_f} + \epsilon_o \frac{\partial \mathbf{E}}{\partial t} + \frac{\partial \mathbf{P}}{\partial t} \tag{2.16}$$

where $\mathbf{E}$ is the electric field vector, $\mathbf{H}$ is the magnetic field vector, $\mathbf{D}$ and $\mathbf{B}$ are the electric and magnetic displacement vectors, $\mathbf{P}$ and $\mathbf{M}$ are the electric and magnetic polarizations, ϵ_o and μ_o are the permittivity and permeability constants, and $\mathbf{J_f} = \sigma \mathbf{E}$ is the electric current density, where σ is the electrical conductivity.

The polarization, $\mathbf{P}$, is defined by

$$\mathbf{P} = \epsilon_o \chi_e \mathbf{E} + \mathbf{P}_{NL} \tag{2.17}$$

where χ_e is the linear electric susceptibility and the nonlinear polarization is defined as

$$(\mathbf{P}_{NL})_i = 2 d_{ijk} E_j E_k \tag{2.18}$$

where $d_{ijk} = \frac{1}{2}\chi_{(2)}$ is a material-dependent tensor. The subscripts i, j, and k in equation 2.18 represent the Cartesian coordinates. The nonlinear polarization is responsible for the origin of the nonlinear frequency terms generated in second-order nonlinear processes like OPG and OPA. To see how these frequencies are generated, we begin by solving for the wave equation in matter. Using $\mathbf{J_f} = \sigma \mathbf{E}$ and equation 2.17, we can rewrite equation 2.16 as

$$\boldsymbol{\nabla} \times \mathbf{H} = \sigma \mathbf{E} + \epsilon \frac{\partial \mathbf{E}}{\partial t} + \frac{\partial \mathbf{P}_{NL}}{\partial t} \tag{2.19}$$

where $\epsilon = \epsilon_o(1 + \chi_L)$. Combining this equation with equation 2.14 and using vector calculus relations, we obtain the wave equation in terms of $\mathbf{E}$ and the nonlinear polarization,

$$\boldsymbol{\nabla}^2\mathbf{E} = \mu_o\sigma\frac{\partial\mathbf{E}}{\partial t} + \mu_o\epsilon\frac{\partial^2\mathbf{E}}{\partial t^2} + \mu_o\frac{\partial^2\mathbf{P}_{NL}}{\partial t^2} \tag{2.20}$$

This is the wave equation that is used for second-order nonlinear processes.

Next consider three plane waves that have distinct frequencies ω_1, ω_2, and ω_3. These plane waves are described by the following equations

$$E_i^{\omega_1}(z,t) = \frac{1}{2}\left[E_{1i}(z)e^{i(\omega_1 t - k_1 z)} + C.C.\right] \tag{2.21a}$$

$$E_j^{\omega_2}(z,t) = \frac{1}{2}\left[E_{2k}(z)e^{i(\omega_2 t - k_2 z)} + C.C.\right] \tag{2.21b}$$

$$E_k^{\omega_3}(z,t) = \frac{1}{2}\left[E_{3j}(z)e^{i(\omega_3 t - k_3 z)} + C.C.\right] \tag{2.21c}$$

where i, j, and k are still the Cartesian coordinates and $k_l = \frac{2\pi n}{\lambda_l}$ is the wavenumber for each wave.

Applying the wave equation from equation 2.20 to each of these electric fields produces the following set of coupled differential equations that define nonlinear processes.

$$\frac{dE_{1i}}{dz} = -\frac{\sigma_1}{2}\sqrt{\frac{\mu_o}{\epsilon_1}}E_{1i} - i\omega_1\sqrt{\frac{\mu_o}{\epsilon_1}}d'_{ijk}E_{3j}E^*_{2k}e^{-i(k_3-k_2-k_1)z} \tag{2.22a}$$

$$\frac{dE^*_{2k}}{dz} = -\frac{\sigma_2}{2}\sqrt{\frac{\mu_o}{\epsilon_2}}E^*_{2k} - i\omega_2\sqrt{\frac{\mu_o}{\epsilon_2}}d'_{ijk}E_{1i}E^*_{3j}e^{-i(k_1-k_3+k_2)z} \tag{2.22b}$$

$$\frac{dE_{3j}}{dz} = -\frac{\sigma_3}{2}\sqrt{\frac{\mu_o}{\epsilon_3}}E_{3j} - i\omega_3\sqrt{\frac{\mu_o}{\epsilon_3}}d'_{ijk}E_{1i}E_{2k}e^{-i(k_1+k_2-k_3)z} \tag{2.22c}$$

The slowly-varying amplitude approximation was made, which says that

$$\left|\frac{d^2E}{dz^2}\right| << \left|k\frac{dE}{dz}\right|$$

It is found in practice that calculating the electric field in the equations presented above can be difficult. However, we can define a variable that represents the photon flux to simplify the calculations, defined as

$$A_l = \sqrt{\frac{n_l}{\omega_l}} E_l \tag{2.23}$$

where l is an integer index for the three plane waves (1, 2, or 3). Making this change of variables, we obtain

$$\frac{dA_1}{dz} = -\frac{1}{2}\alpha_1 A_1 - i\kappa A_2^* A_3 e^{-i(\Delta k)z} \tag{2.24a}$$

$$\frac{dA_2^*}{dz} = -\frac{1}{2}\alpha_2 A_2^* + i\kappa A_1 A_3^* e^{i(\Delta k)z} \tag{2.24b}$$

$$\frac{dA_3}{dz} = -\frac{1}{2}\alpha_3 A_3 - i\kappa A_1 A_2 e^{i(\Delta k)z} \tag{2.24c}$$

where $\Delta k = k_3 - k_1 - k_2$ and is called the phase-matching condition, $\kappa = \frac{1}{2} d'_{123} \sqrt{\left(\frac{\mu_o}{\epsilon_o}\right) \frac{\omega_1 \omega_2 \omega_3}{n_1 n_2 n_3}}$, and $\alpha_l = \sigma_l \sqrt{\frac{\mu_o}{\epsilon_o}}$ is the loss in the system. These equations are known as the coupled wave equations for nonlinear processes and are used to calculate the output of nonlinear systems.

Solutions for Optical Parametric Amplification

We can use the coupled wave equations to describe nonlinear processes associated with the $\chi_{(2)}$ susceptibility. Solutions for optical parametric generation are difficult to calculate since the process starts from spontaneous generation within the nonlinear crystal. In this section, we focus on optical parametric amplification where a known input seed is amplified as it propagates through the nonlinear material. The coupled wave equations are generally solved numerically, but they can be solved directly for

the special case of non-depleted pump allowing one to gain some insight into the nonlinear conversion process.

Non-depleted Pump

In the non-depleted pump approximation, we make the assumption that the pump wave is negligibly depleted through the nonlinear process. We define the waves as follows: 1 is the signal, 2 is the idler, and 3 is the pump. With the non-depleted pump approximation, we assume that $\frac{dA_3}{dz} = 0$, which simplifies the coupled wave equations. In general, crystals which are transparent at the pump, signal, and idler wavelengths are used for conversion processes, so that there are negligible losses and $\alpha_l = 0$. With these simplifications it is straightforward to find the solution for A_1 and A_2 from equations 2.24. That is,

$$A_1(z)e^{i\Delta kz} = A_1(0)\left[cosh(bz) + \frac{i\Delta k}{b}sinh(bz)\right] - \frac{ig}{b}A_2^*(0)sinh(bz) \qquad (2.25a)$$

$$A_2^*(z)e^{-i\Delta kz} = A_2^*(0)\left[cosh(bz) - \frac{i\Delta k}{b}sinh(bz)\right] + \frac{ig}{b}A_1(0)sinh(bz) \qquad (2.25b)$$

where $b = \sqrt{g^2 - (\Delta k)^2}$, $g = \kappa A_3(0) = \frac{1}{2}d'E_3(0)\sqrt{\left(\frac{\mu_o}{\epsilon_o}\right)\frac{\omega_1\omega_2}{n_1n_2}}$. Here g is a gain quantity that depends on the material constants defined by κ and the photon flux of the input pump beam. The equations above are used to describe the process of optical parametric amplification with signal and idler seed beams at the input, $A_1(0)$ and $A_2^*(0)$.

In most cases, only an input seed at the signal wavelength is used, so that $A_2^*(0) = 0$. This simplifies the above equations to

$$A_1(z) = A_1(0)\left(cosh(bz) + \frac{i\Delta k}{b}sinh(bz)\right)e^{-i\Delta kz} \qquad (2.26a)$$

$$A_2^*(z) = \frac{ig}{b}A_1(0)\left(sinh(bz)\right)e^{i\Delta kz} \qquad (2.26b)$$

These equations allow us to find the photon flux of the signal and idler beams at any point z within the crystal and are valid only for parametric amplification in the non-depleted pump approximation. To convert to optical power we use the relation

$$P_l = \frac{1}{2}\sqrt{\frac{\epsilon_o}{\mu_o}}\omega_l a_l |A_l|^2 \tag{2.27}$$

where a_l is the area of the beam.

Notice that from equation 2.26, the maximum output will be obtained when $\Delta k = 0$. This condition is called perfect phase matching and occurs when all three waves are in phase simultaneously within the material. Using this condition in equation 2.26 we get

$$A_1(z) = A_1(0)cosh\left(\frac{gz}{2}\right) \tag{2.28a}$$

$$A_2^*(z) = iA_1(0)sinh\left(\frac{gz}{2}\right) \tag{2.28b}$$

which results in the largest output at the signal and idler wavelength for a given set of input conditions.

Phase-matching

Perfect phase-matching, which occurs when $\Delta k = 0$, results in the highest possible output in a nonlinear process. If $\Delta k = k_1 + k_2 - k_3$ as it does for OPA, then for perfect phase-matching the following equation must be satisfied

$$\frac{n_1\omega_1}{c} + \frac{n_2\omega_2}{c} = \frac{n_3\omega_3}{c} \tag{2.29}$$

Since ω is fixed for each wavelength we need a way to adjust n for each wavelength. In most materials, $n(\omega)$ increases with ω, therefore the equation cannot

be satisfied, since from conservation of energy, $\omega_1 + \omega_2 = \omega_3$. However a certain class of crystals are birefringent, meaning the refractive index that light will experience depends on the direction of polarization and direction of propagation of the light. Therefore, under certain conditions, equation 2.29 can be satisfied.

To satisfy equation 2.29 using birefringent materials, we follow a derivation from Boyd [8]. All materials have an associated index ellipsoid given by

$$\frac{x^2}{n_x^2} + \frac{y^2}{n_y^2} + \frac{z^2}{n_z^2} = 1 \tag{2.30}$$

where x, y, and z are the major axes of the ellipsoid and n_x, n_y, and n_z are the corresponding indices of refraction along the axes. Consider a uniaxial crystal, which is the most common and simplest birefringent material, in which $n_x = n_y = n_o$ and $n_z = n_e$ where z is the optical axis, n_o is the ordinary index of refraction, and n_e is the extraordinary index of refraction. The ordinary index of refraction is the index of refraction that light will experience if the light is polarized perpendicular to the optical axis. Therefore in a uniaxial crystal the index ellipsoid can be written as

$$\frac{x^2}{n_o^2} + \frac{y^2}{n_o^2} + \frac{z^2}{n_e^2} = 1 \tag{2.31}$$

The index of refraction that light will experience depends on the direction of propagation and the direction of polarization, so that the index of refraction is a function of θ: $n_e(\theta)$. To calculate this at any angle θ we use the equation

$$\frac{1}{n_e^2(\theta)} = \frac{cos^2(\theta)}{n_o^2} + \frac{sin^2(\theta)}{n_e^2} \tag{2.32}$$

Perfect phase-matching can be achieved through careful selection of the polarizations of the input waves and the angle of propagation with respect to the optic axis. This method of phase-matching is called angle phase-matching [8].

Another method of phase-matching is temperature tuning. In some crystals, the amount of birefringence is temperature-dependent. This allows the angle of propagation to be held at 90 degrees while only the temperature is adjusted. The temperature required for perfect phase-matching is determined with the Sellmeier equations which depend on the material constants [10].

Under many circumstances, angle phase-matching and temperature tuning cannot be used effectively. Insufficient birefringence in a material can make phase-matching difficult, especially at shorter wavelengths. More often, these techniques cannot be used when trying to access the d_{33} nonlinear coefficient, which is the largest coefficient for lithium niobate [11]. This coefficient can only be accessed if all the interacting waves have the same polarization, and therefore angle phase-matching will not work and it will be difficult to compensate for dispersion.

A technique used to access the d_{33} coefficient is called quasi-phase-matching (QPM). This technique divides the nonlinear crystal into periodic polarization domains where the sign of the polarization is inverted 180 degrees at regular intervals. This effectively inverts the sign of d_{eff} which compensates for a nonzero value of Δk caused by dispersion. Although it is not perfect phase-matching through the entire crystal, the increased gain due to accessing the d_{33} coefficient makes this method more efficient for many materials.

From Boyd [8], quasi-phase-matching is described mathematically as follows. Let $d(z)$ be the nonlinear coupling coefficient as a function of distance along the crystal axis and assume we are trying to access the d_{33} coefficient in lithium niobate. If the

material is periodically poled in a square-wave function then,

$$d(z) = d_{33} sign\left[cos\left(\frac{2\pi z}{\Lambda}\right)\right] \tag{2.33}$$

where $sign(x)$ is a function that outputs -1, 0, or 1 depending on if the output is negative, zero, or positive. Equation 2.33 can be written as a Fourier series so that

$$d(z) = d_{33} \sum_{m=-\infty}^{\infty} G_m e^{ik_m z} \tag{2.34}$$

Here $k_m = 2\pi m/\Lambda$, where Λ is the poling period, m is the order of the conversion process, and G_m are coefficients given by

$$G_m = \frac{2}{m\pi} sin\left(\frac{m\pi}{2}\right)$$

Since first-order processes result in the largest output, we assume that $m = 1$ and therefore the coupling coefficient is

$$d(z) = \frac{2}{\pi} d_{33} e^{i\frac{2\pi}{\Lambda}z} = d_{eff} e^{i\frac{2\pi}{\Lambda}z} \tag{2.35}$$

where $d_{eff} = \frac{2}{\pi} d_{33}$ is the effective nonlinear coefficient, which is not spatially varying. The nonlinear coefficient is reduced by using quasi-phase-matching, but it is the only way to access the d_{33} coefficient of lithium niobate.

Applying equation 2.35 to the coupled wave equations in place of d_{ijk}, we find that the phase-matching condition is

$$\Delta k = k_1 + k_2 - k_3 - \frac{2\pi}{\Lambda} \tag{2.36}$$

Solving for Λ, we find that the poling period needed to satisfy phase-matching is

$$\Lambda = \frac{2\pi}{(k_1 + k_2 - k_3)} \tag{2.37}$$

The value of Λ is generally on the order of microns to tens of microns, depending on the phase-matching condition that one is trying to satisfy. By heating and cooling a periodically poled crystal, the phase-matching condition can be changed slightly due to the temperature-dependent index of refraction in lithium niobate. Quasi-phase-matching is the technique used in this research because we are trying to access the d_{33} coefficient of lithium niobate.

Depleted Pump

The non-depleted pump approximation is only valid for nonlinear processes that have relatively low conversion of the pump photons into signal and idler photons. Therefore if we want to model a high conversion process, we must solve the coupled wave equations numerically.

For OPA with non-negligible depletion of the pump beam, the coupled wave equations must be solved numerically. Starting from the coupled wave equations in equation 2.24 and assuming the general case where the pump can become depleted through the conversion process, a program was written in Matlab (see Appendix A) to perform the task of numerical integration of these equations.

To simplify the integration, it is assumed that $\Delta k = 0$ and the system is lossless, that is transmissive and non-absorbing at the pump, signal, and idler wavelengths. The coupled wave equations assume plane waves at the input to the system and that the beams are not pulsed. In order to model a pulsed pump beam, we took the peak

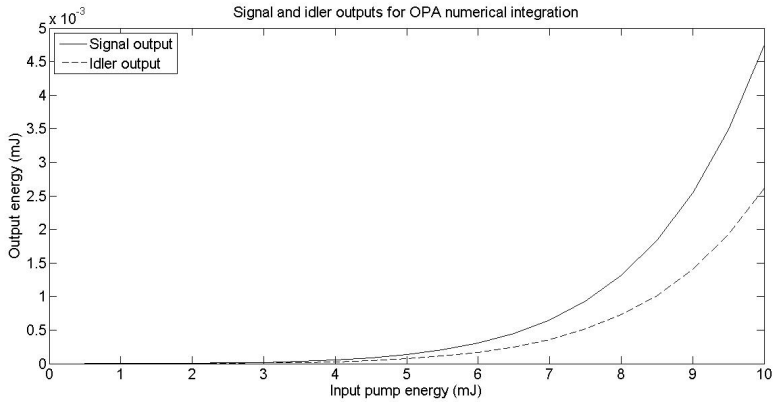
power of the beam as the input to the model using

$$P_{peak} = 0.94 * \frac{E_{pump}}{\Delta t}$$

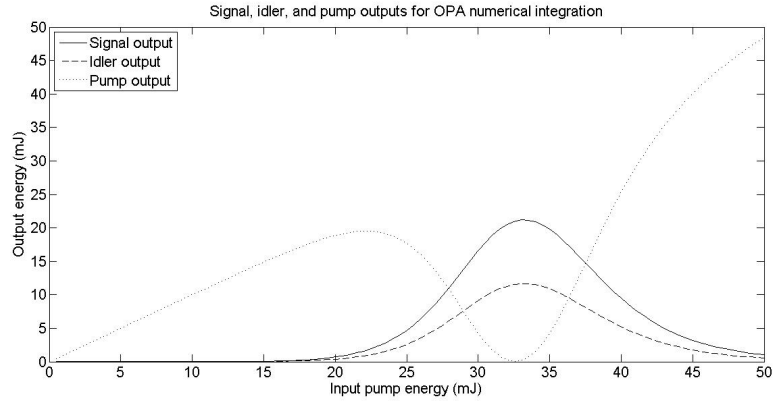
where E_{pump} is the energy of the pulsed pump beam and Δt is the pulse width, which we took to be 10 ns for the model. A 2 cm long nonlinear crystal with d_{eff} =14.8 $\frac{pm}{V}$ was modeled in the program to simulate the output from a periodically poled lithium niobate crystal. The seed laser beam was taken to have an output power of 1 mW with 0.67 mm ($\frac{1}{e^2}$) beam radius. Additionally the pump, signal, and idler wavelengths were chosen to be 1064 nm, 1650 nm, and 2995 nm, respectively.

Figure 2.2 shows the output of the numerical integration for each of the beams. These plots show the output energies from OPA as a function of pump energy as calculated in the Matlab numerical integration program. Figure 2.2a shows the output signal and idler wavelengths at relatively low input pump energies and illustrates the exponential behavior that is seen in the case of the non-depleted pump. This approximation is generally valid at low input energies, which is why this trend is seen in this plot. Figure 2.2b shows the signal, idler, and pump outputs over much higher pump energies. It is clear that the non-depleted pump approximation becomes invalid around 20 mJ of input pump energy, where the pump output no longer has a linear trend. The model even predicts full pump depletion near 27 mJ pump energy. Beyond this level, the pump regains energy through a process called back-conversion, where the conversion process happens in reverse. The output from the numerical integration program works as expected from the coupled wave equations and provides insight on when the non-depleted pump approximation is valid.

The non-depleted pump approximation is valid at relatively low input pump energies, but the level at which considerable pump depletion occurs depends on many



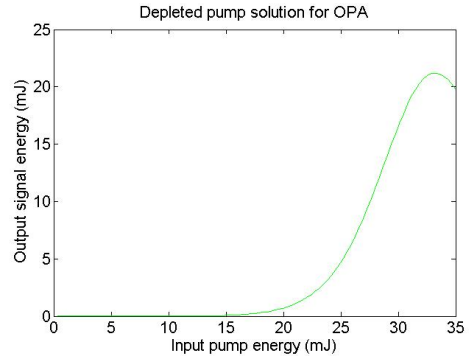
(a) Signal and idler



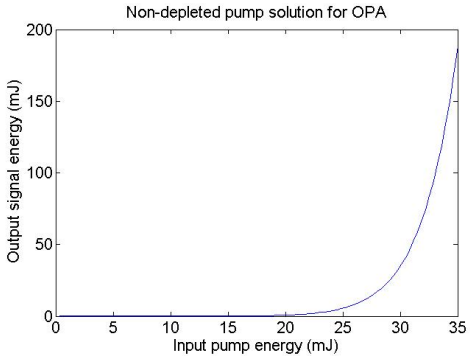
(b) Signal, idler, and pump

Figure 2.2: Signal, pump, and idler outputs from OPA produced in Matlab using the coupled wave equations (see Appendix A). Figure (a) shows the signal and idler outputs that increase exponentially at low pump energies. Figure (b) shows a larger range of input pump energies and full depletion of the pump near 20 mJ, illustrating the limitations of the non-depleted pump approximation.

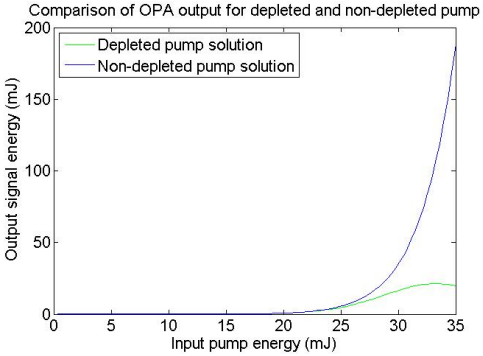
variables. Consider the solution to the coupled wave equations for the case of non-depleted pump. The output photon flux $A_1(L)$ depends on g and L, where $g = \kappa A_3(0)$. The output energy depends on the intensity of the output, which depends on the photon flux and the area of the beam. Taking all of this together, the variables that determine the limit where the non-depleted pump approximation is valid are: beam intensity, length of crystal, input signal power, and d_{eff}.



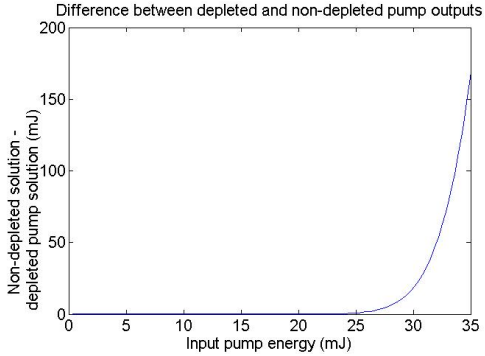
(a) OPA signal out (depleted pump)



(b) OPA signal out (non-depleted pump)



(c) Depleted and non-depleted pump



(d) Difference between depleted and non-depleted pump

Figure 2.3: Comparison of the signal output from OPA in the depleted and non-depleted pump approximation. Figure (a) shows the output from the OPA model in the case of a depleted pump input. Notice that the output signal energy reaches a peak value then begins to drop due to the conversion process working in reverse. Figure (b) shows the OPA signal output in the non-depleted pump approximation. The signal energy reaches unrealistic values where it gains significantly more energy than the input pump, demonstrating why the non-depleted pump approximation is only valid for small pump inputs. Figure (c) shows both the depleted and non-depleted pump solutions plotted together. It is evident that the two results begin to diverge from each other near 25 mJ of pump energy, and various factors determine where this divergence occurs. Figure (d) shows the difference between the two solutions.

Figure 2.3 compares the solutions for the depleted pump and the solutions for the non-depleted pump at the signal wavelength with all of the parameters constant. The plots in a and b show the OPA signal output for the depleted pump case and

non-depleted pump case, respectively. To get a sense of the scale, the two are plotted together in c. It is apparent that the results begin to diverge near 25 mJ of input pump energy. The difference between the results is shown in d, further showing where the case of the non-depleted pump breaks down.

These plots show the result for one choice of variables. However a small change in one of the variables, such as input pump beam diameter, will result in a significant change to these results and will change the point where the two solutions diverge. This point must be known before attempting to use the non-depleted pump approximation since it can produce inaccurate results at high pump energies. When possible, it is best to use the depleted pump solutions since it makes a more accurate model, but non-depleted pump is faster and more straightforward to solve.

Solutions for Optical Parametric Oscillation

Just like for OPA, the coupled wave equations are used to model OPO, but here the losses, α_l, must be considered due to the losses in the cavity mirrors. Following a derivation from Yariv [9], we look at the case of non-depleted pump and assume that the pump beam is negligibly depleted through the conversion process, so that $\frac{dA_3}{dz} = 0$ and we can define $g = \kappa A_3(0) = 2\sqrt{\left(\frac{\mu_o}{\epsilon_o}\right)\frac{\omega_1\omega_2}{n_1 n_2}}d' E_3(0)$. Rewriting the coupled wave equations to include losses, we get

$$\frac{dA_1}{dz} = -\frac{1}{2}\alpha_1 A_1 - igA_2^* e^{-\frac{i\Delta kz}{2}} \tag{2.38a}$$

$$\frac{dA_2^*}{dz} = -\frac{1}{2}\alpha_2 A_2^* + igA_1 e^{\frac{i\Delta kz}{2}} \tag{2.38b}$$

where α_l are the distributed losses at each wavelength. If the loss per pass through the cavity is small, we can say that $\alpha_l L = 1 - R_l$, where L is the length of the

cavity. Ultimately, we want to consider steady-state oscillation in the cavity, where $\frac{dA_1}{dz} = \frac{dA_2}{dz} = 0$. Therefore the equations for steady-state oscillation are

$$-\frac{\alpha_1}{2}A_1 - igA_2^* = 0 \tag{2.39a}$$

$$igA_1 - \frac{\alpha_2}{2}A_2^* = 0 \tag{2.39b}$$

These equations have a nontrivial solution, where

$$g_t^2 = \frac{\alpha_1\alpha_2}{4} \tag{2.40}$$

which is the threshold for oscillation. Considering that g depends on the magnitude of the electric field of the pump beam, this equation states that the pump field must reach a certain magnitude before the gains from the nonlinear conversion can balance the losses due to the cavity mirrors.

Modeling Nonlinear Proceeses

Unless the non-depleted pump approximation is employed, more advanced methods of obtaining solutions for OPA and OPO are necessary. Generally this involves numerical integration of the coupled wave equations. Numerical integration for OPA is relatively straightforward; however, OPO is a complex process that is difficult to model without a program made to do this calculation. Many factors come into play in the model of an OPO, including: cavity mirror reflectivities, input beams including the shape of the pulse if using a pulsed input, length of the cavity, and curvature of the mirrors and the beam.

SNLO [12] is a program developed at Sandia National Laboratory particularly for calculation of the performance of nonlinear optical processes. SNLO contains information for most nonlinear crystals including index of refraction along each crystal axis, nonlinear coefficients, and temperature data among others. It can calculate OPA and OPO outputs for plane wave and gaussian inputs. SNLO cannot accurately calculate outputs for OPG because it does not account for spontaneous generation.

We have used this program extensively for modeling the expected performance of our system. It is most useful for modeling OPO since writing a numerical integration program to do this would be very time-consuming. To ensure that SNLO produces outputs on the order of what we expect from the coupled wave equations, we compared the outputs of OPA from the Matlab numerical integration program to the outputs from SNLO.

Comparison of Matlab Numerical Integration to SNLO Model

To get a better understanding of SNLO, the Matlab numerical integration program used before was compared to the output generated by SNLO for the case of OPA. All of the relevant parameters were the same for each program. These parameters are shown in figure 2.4. Here, the 2D (gaussian) model was used for the SNLO model and the Matlab program assumes a plane wave. In the SNLO model, a plane-wave is simulated in the 2D model by setting the radius of curvature of each beam to a very large value.

Figure 2.5 shows the output from the Matlab program and SNLO for the signal, idler, and pump beams in plots a, b, and c, respectively. The signal and idler outputs from each program agree within about 10%, and the pump outputs show no discernible difference. The discrepancy in the signal and idler outputs could be due to the difference in how SNLO handles pulsed beams compared to Matlab program.

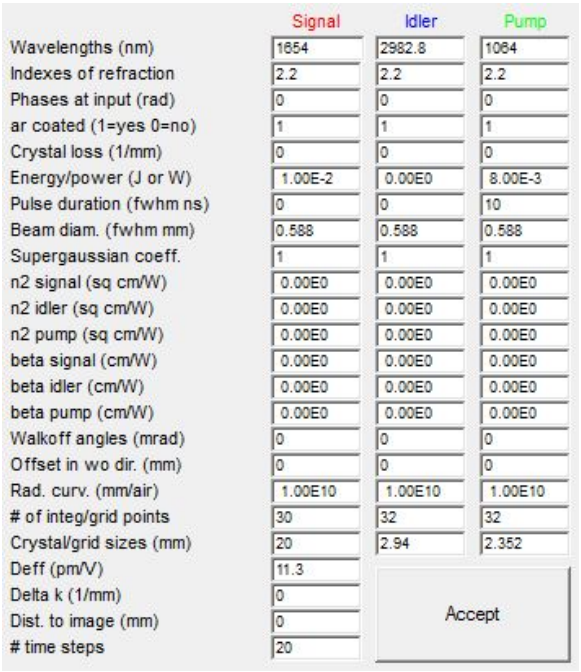
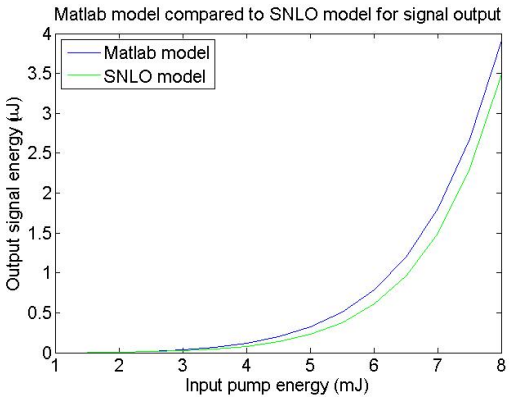
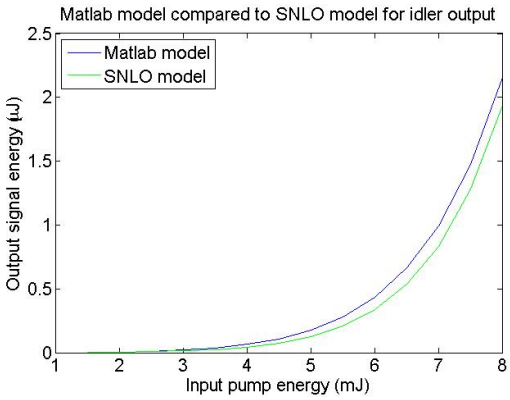


Figure 2.4: Image of the SNLO interface for modeling the output from OPA for a 2D (gaussian) beam. A plane wave was modeled by setting the radius of curvature of the beams to very large values in order to compare the SNLO model to the numerical integration of the coupled wave equations.

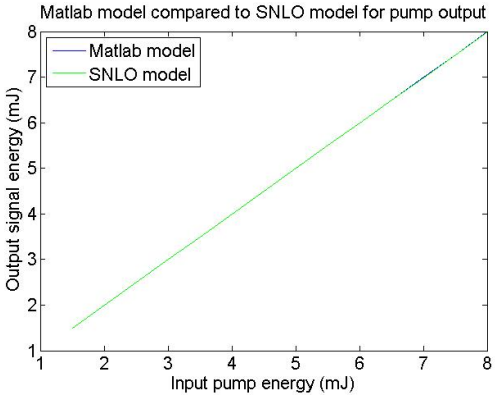
By comparing SNLO with the Matlab program for numerical integration of the coupled wave equations, we see that the two solutions have comparable results. The small differences could be due to the differences in how each program handles the pulsed pump beam at the input. These differences are small so we are confident that SNLO will provide reliable results for more complicated models of OPO. SNLO is used extensively in this research to model expected performance of OPA and OPO. These results will be discussed in the following chapters in which the data from the OPA and OPO are presented.



(a) Matlab and SNLO signal



(b) Matlab and SNLO idler



(c) Matlab and SNLO pump

Figure 2.5: Comparison of the Matlab program to SNLO for OPA with the same parameters for each of the waves at the output. As seen in figures (a) and (b), the outputs for each of the programs are slightly different but follow the same trend. In figure (c), the pump output calculated with each program shows no discernible difference between the two methods. Overall, the two methods provide comparable results.

OPTICAL PARAMETRIC AMPLIFICATION

Before building the OPO, we must have an understanding of the properties of the crystal, in particular an estimate of the value of d_{eff} and Δk, where d_{eff} acts as a gain term and Δk acts as a loss term to account for mismatch between the seed and pump focusing. OPG and OPA have fewer variables than the OPO and is therefore much simpler to compare to theory and through this we can estimate d_{eff}. Measuring the output produced from OPG and OPA allows us to test how well the SNLO model works and will provide a baseline for what to expect from the OPO. Comparing the OPO output to the OPA and OPG output will show if the cavity is actually increasing the output. This section describes the experiment and the results to show how OPG and OPA are different and the variables that are involved. We also compare results to the plane-wave theory and SNLO's gaussian beam OPA theory and use this information to estimate d_{eff} and Δk.

Methods and Setup

Figure 3.1 shows the setup for the experiment for measuring the output from OPA. A diode laser that emits 1654 nm light up to about 5 mW is used as the seed laser (Eblana Photonics EP1654-DM-B01-FM). The beam is nominally collimated into the crystal with a beam radius of approximately 0.46 mm ($\frac{1}{e^2}$). For the OPG measurements, the seed laser is turned off. The pump laser used is a flashlamp-pumped, Q-switched Nd:YAG operating multi-spatial mode with 10 ns pulse duration, a pulse repetition rate of 20 Hz, and an operating wavelength of 1.064 μm (Big Sky Laser ULTRA series). The beam profile was measured and the results are shown in figure 3.2a and an image of the beam at the focus is shown in figure 3.2b to illustrate the high spatial mode of the beam.

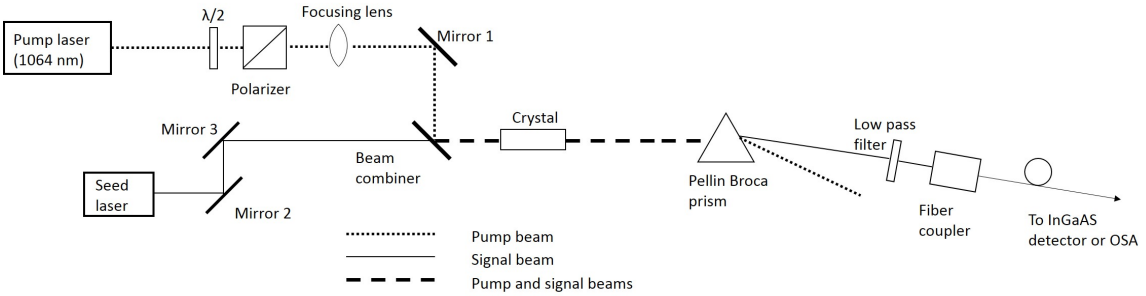
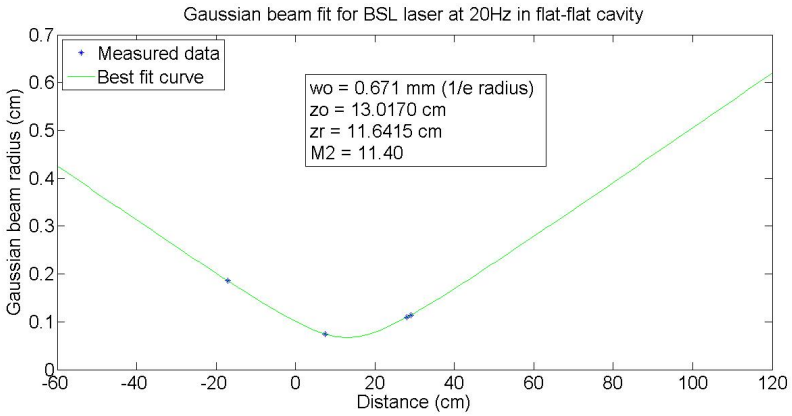


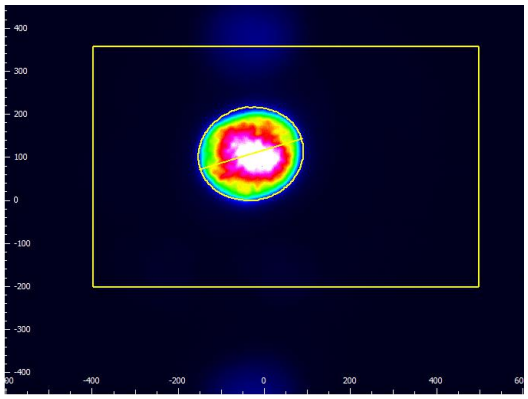
Figure 3.1: Setup for the OPA and OPG measurements. Note that for the OPG measurements, the seed laser is turned off. The half-wave plate and polarizer in the pump beam path are used to adjust the pump energy. For the highest conversion in OPA, the pump and seed beams need to be collinear within the crystal. Two Pellin-Broca prisms (one shown) after the crystal separate the signal beam from the pump beam and any other generated wavelengths.

The crystal used for this experiment is a 5% magnesium-oxide-doped lithium niobate crystal (Mg:LiNb0$_3$) with a poling period of 31.447 μm. The crystal is 30 mm long with a 2 mm square aperture and anti-reflection (AR) coatings on both faces of the crystal at the pump, signal, and idler wavelengths. The crystal is mounted in a brass heater that surrounds the crystal to minimize temperature gradients within the crystal. The heater increases the temperature of the crystal, thereby changing the index of refraction based on the temperature-dependent Sellmeier equations. This changes the phase-matching condition, and therefore the generated signal wavelength. Figure 3.3 shows the crystal mounted inside the heater.

To show the differences between the output of OPG and OPA, we set up an experiment so that we could measure the output spectra and the output peak signal power for each. As shown in figure 3.1, the pump beam is directed to the crystal using two steering mirrors. A half wave plate and a polarizer allow us to change the energy out of the pump laser without changing the properties of the beam. The pump beam is focused with a lens in order to increase the intensity inside the crystal. For



(a) Gaussian beam profile of the focused Nd:YAG beam. The points in blue represent measured values of the beam radius, and the green line represents the best-fit to these points based on the gaussian beam propagation equations. The M^2 value indicates that this is a high spatial mode gaussian beam.



(b) Image of the Nd:YAG beam at the focus. The high-intensity center of the spot further indicates the high-spatial mode of this beam.

Figure 3.2: Gaussian beam profile and image of pump beam at the focus.

OPG, only the pump beam is incident on the crystal and the signal beam is generated inside the crystal. For OPA, the seed laser is collinear with the pump beam into the crystal. The output from the crystal is separated using two Pellin-Broca prisms (one shown) to separate the light by wavelength. A low-pass optical filter before a fiber coupler ensures that any remaining pump light is extinguished before entering the multimode fiber. The fiber can be connected to an optical spectrum analyzer (OSA)

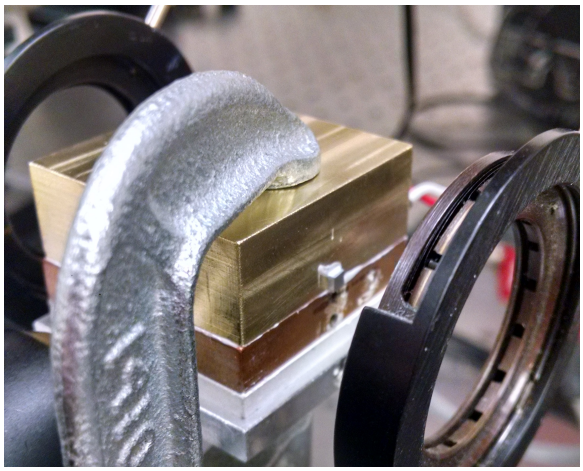


Figure 3.3: The nonlinear crystal is shown inside the brass heater. The heater completely encloses the crystal except the input and output faces in order to ensure minimal temperature gradients within the crystal.

to measure the spectrum of the output or to an indium gallium arsenide (InGaAs) detector connected to an oscilloscope to measure the peak signal power.

Measurement of the peak signal power out of the crystal relies on the assumption that the pump and seed beams are collinear along the entire beam path. To do this, the fiber coupler was adjusted so that the maximum output of OPG was coupled into the fiber. This guarantees that the generated signal is coupled into the fiber. Irises were placed around the pump beam at various points along the beam path and the seed laser was aligned to pass through the center of these irises. By doing this, the seed laser should also be coupled into the fiber. Small adjustments were then made to the seed laser angle to maximize the OPA output. With both beams coupled into the fiber and collinear along the entire beam path a measurement of the peak output power at the signal wavelength can be made.

The output from the InGaAs detector sends a voltage that is proportional to the power of the measured light to the oscilloscope. Since the OPA and OPG output passes through many optical elements with some losses, we had to make a

measurement to determine the voltage to power conversion just after the crystal. To do this, the power of the seed laser was measured before entering the crystal. The DC voltage on the oscilloscope from the detector provides a conversion from voltage to power. The signal out of the crystal is pulsed light and therefore we want to measure the peak power, which is proportional to the energy in the pulse. The peak power is determined by triggering on the pump laser Q-switch and measuring the height of the output signal pulse on the oscilloscope. For OPG in particular, the signal pulses have significant variation due to spontaneous generation in the crystal. Our measurements therefore consist of an average of hundreds of pulses with error bars corresponding to the minimum peak power and the maximum peak power. Therefore our error bars are very large since they account for the full range of variability in the measurement. In order to remove systematic error between the OPG and OPA power measurements, the OPA data were collected and then the seed laser was turned off and the OPG data were collected. This was repeated for each pump energy value.

The two most important aspects of this measurement are ensuring that the pump and seed laser are collinear in the crystal that the system is phase-matched. As discussed in the theory section, the phase-matching condition for a periodically poled crystal is adjusted by heating or cooling the crystal. The goal is to heat the crystal to a temperature that produces an OPG output centered about the seed laser wavelength. This is done using an OSA to look at the output spectra of OPG and the seed laser. Poor spectral overlap occurs when the peak wavelength of the seed laser spectrum and the OPG spectrum are not coincident. When there is good spectral overlap, this means Δk is close to its minimum value. This will result in a narrower OPA spectrum.

When the pump and seed laser are not collinear, then the beams have poor spatial overlap. This limits the amount of conversion to the signal wavelength due

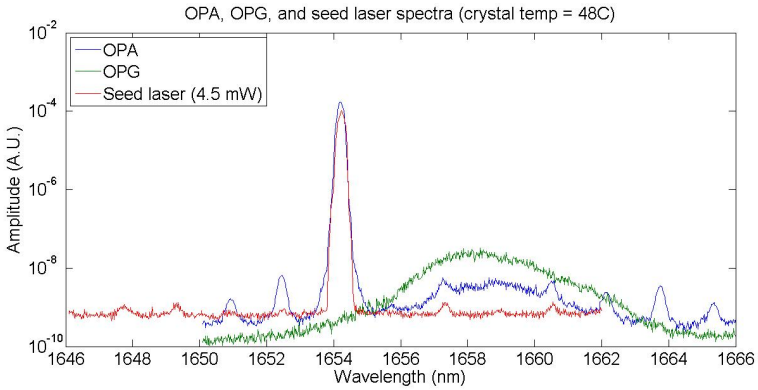
to the decreased spatial overlap between the two beams. Poor spatial overlap shows up differently in the spectra than poor spectral overlap. When the spatial overlap is not optimized, then the OPG and seed laser spectra are still centered, but the OPA spectrum is very wide. Adjusting the positioning of the seed laser until the OPA spectrum is narrow indicates the spatial overlap is optimized.

Results

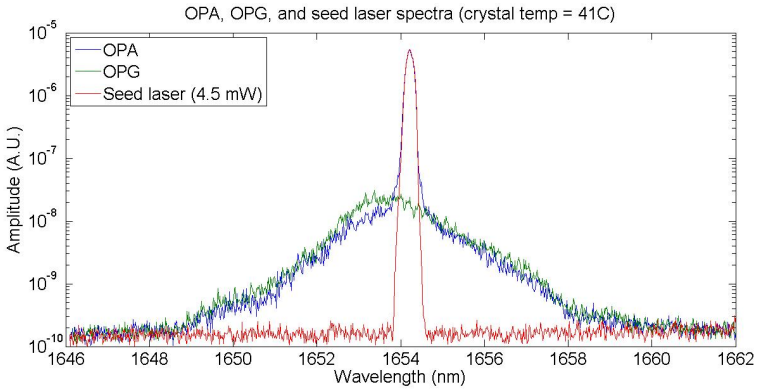
We begin by looking at the output spectra for three cases of the OPA. Figures 3.4a and 3.4b show how the spectra change for poor spectral overlap, poor spatial overlap, and good spectral and spatial overlap. OPA will be more efficient in the case of good spatial and good spectral overlap.

Spectral overlap is how well the center of the OPG spectrum matches the center of the seed laser spectrum. The crystal poling and crystal temperature determine the central wavelength of the OPG output spectrum through quasi-phase-matching, discussed in section 2 of chapter 2. Good spectral overlap increases the efficiency of the OPA because there is more gain available at the center wavelength of the OPG than at the sidebands. The OPG spectrum at the signal wavelength is broadband because the signal arises from spontaneous generation in the crystal. For ideal spectral overlap, the center wavelength of the OPG output will overlap with the center of the seed laser spectrum. Figure 3.4a shows the OPA, OPG, and seed laser spectra for the case of poor spectral overlap. It is clear that the center of the OPG spectrum does not coincide with the seed laser center wavelength. Figure 3.4b demonstrates good spectral overlap but poor spatial overlap.

Spatial overlap defines how well the pump and seed beams are aligned in space as they propagate through the nonlinear crystal. When these beams are collinear



(a) Output spectra showing poor spectral overlap of the OPG and seed laser along with the resulting OPA spectra. Notice how the peak of the OPG spectrum does not line up with the peak of the seed laser spectrum. This causes a broad side feature in the OPA spectrum.



(b) Output spectra showing poor spatial overlap of the seed and pump laser in the OPA spectrum. When the seed beam is not collinear with the pump, the output OPA spectrum becomes broad with a narrow peak on top. The system does have good spectral alignment, since the peak of the OPG is near the peak of the seed.

Figure 3.4: Output spectra showing poor spectral overlap (a), and poor spatial overlap (b). Poor spectral overlap occurs when the peak of the OPG spectrum does not coincide with the peak of the seed laser spectrum. Poor spatial overlap broadens the output OPA spectrum so that it is nearly as broad as the OPG spectrum. Ideally the OPA spectrum should be narrow.

through the crystal, also called injection seeding, the OPA efficiency is increased because it creates a longer interaction length of the two beams in the crystal. The pump beam sets up a volume of gain that can be converted to the signal wavelength,

as long as the seed beam coincides with that volume and has enough power to saturate the gain. If not, the remaining gain will allow spontaneous generation at any wavelength that is phase-matched (as shown in the OPG spectrum). Figure 3.4b demonstrates this with the wide sidebands on the OPA spectrum due to spontaneous emission throughout the crystal from poor spatial overlap.

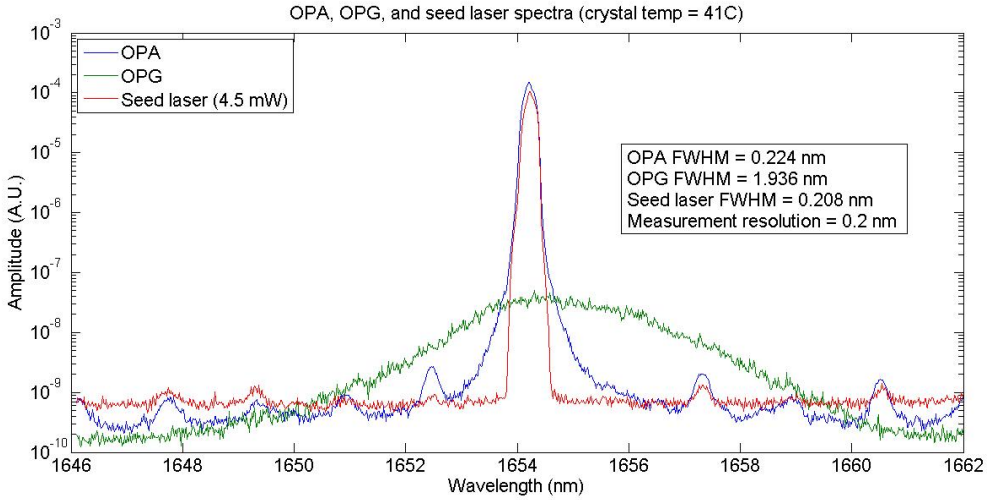
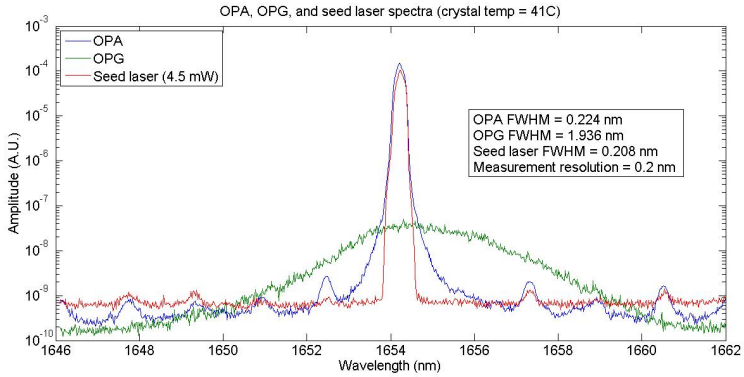
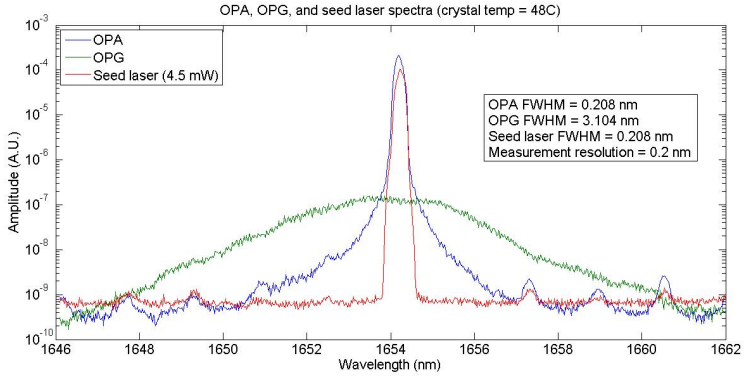


Figure 3.5: Output spectra showing good spectral and spatial overlap. The peak of the OPG spectrum (green) coincides with the peak of the seed laser spectrum (red), resulting in a narrow OPA output spectrum (blue). The FWHM of the OPA spectrum is on the order of the measurement resolution of the OSA.

Figure 3.5 shows the spectral outputs for the case of good spatial and good spectral overlap. The OPA output spectrum is narrow, with minimal sidebands. The OPG spectrum aligns well with the seed laser spectrum creating a narrow and symmetric OPA spectrum. This is the ideal case for alignment of the OPA. Notice that the resolution of the OSA for this measurement is 0.2 nm and the FWHM of the OPA spectrum is 0.224 nm. Higher resolution on the OSA is needed to determine the actual width of the OPA spectrum. However it is apparent from this plot that the use of the seed laser makes the OPA spectrum much narrower than the OPG spectrum.



(a) Output spectra showing good spatial and spectral overlap. The input pump energy is 3 mJ and the OPA spectrum appears narrow with minimal side modes.



(b) Output spectra with 3.5 mJ of input pump energy. The OPA spectrum still demonstrates good spatial and spectral overlap, but the increased pump energy has widened the spectrum. Although the FWHM of the OPA spectrum is still on the order of the measurements resolution, the size of the side modes in the OPA spectrum has increased

Figure 3.6: Notice how the OPA spectra in (b) is wider than in (a). This is due to the increased pump energy and the seed power, which isn't high enough to saturate the gain at higher pump energies. Increased seed laser power is expected to make the spectrum narrow again.

Next we look at how increasing the pump energy changes the OPA spectrum. Figure 3.6 shows how the OPA spectrum changes with an increase in the pump energy into the crystal. The plot in figure 3.6a is the same plot from figure 3.5, placed here for comparison to figure 3.6b. The pump energy in figure (a) is 3 mJ, and is 3.5 mJ in

figure (b). The OPA spectrum has larger sidebands when the energy is increased due to the increased gain from the pump beam, but since the seed laser is still 4.5 mW, it doesn't have enough power to saturate the additional gain in the system, leading to amplification of spontaneous emission. A higher-power seed laser is necessary to maintain the narrow OPA spectrum at high pump energies.

As a side note, from figure 3.6 it appears that the OPA signal output increases negligibly due to the increase in pump energy. This, however, is an artifact of the measurement on the OSA. Due to the pulsed OPA output, it is difficult to capture the relative size of the pulsed output compared to a CW output. Therefore we need a measurement of the actual output energy of the signal beam to make this comparison.

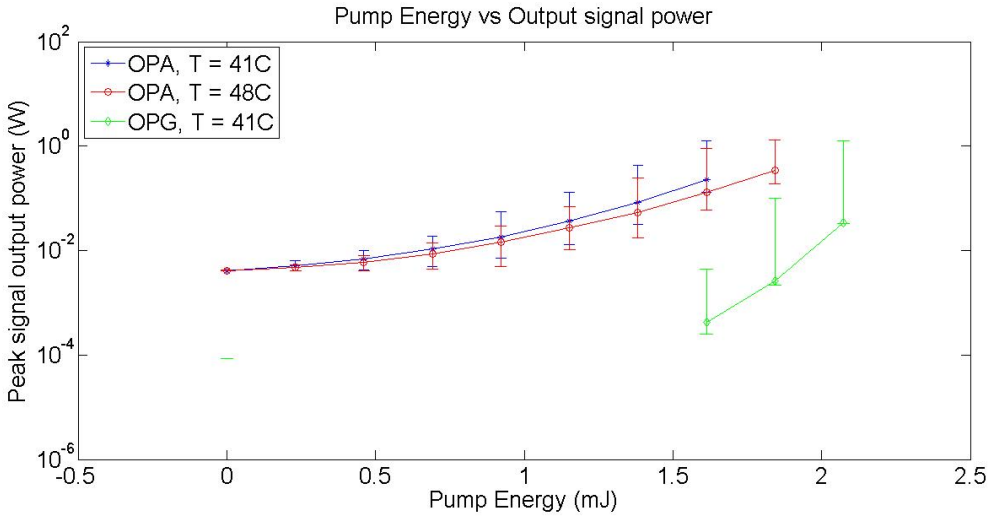


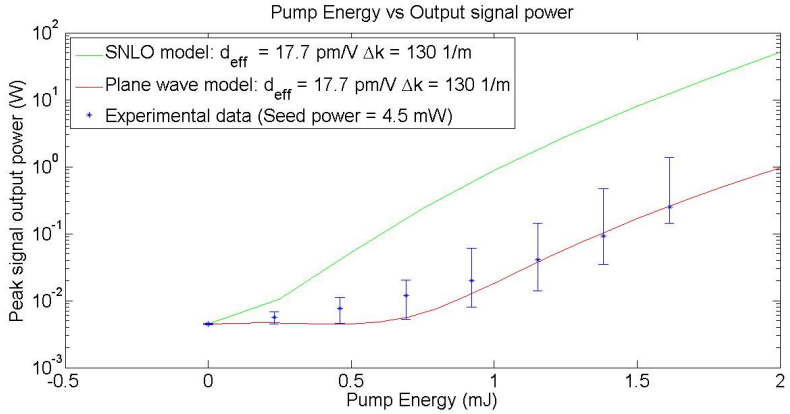
Figure 3.7: OPA and OPG peak power outputs at 41°C and 48°C plotted on a log scale. The OPA output at 41°C, where it is phase-matched, has the largest output of the three. The output from OPA is always larger than OPG since OPA is an amplification process and OPG arises from spontaneous generation.

The plot in figure 3.7 shows the peak output power at the signal wavelength, which is proportional to the output energy. At low input pump energies the OPA output is significantly larger than OPG, since the seed laser amplifies the output.

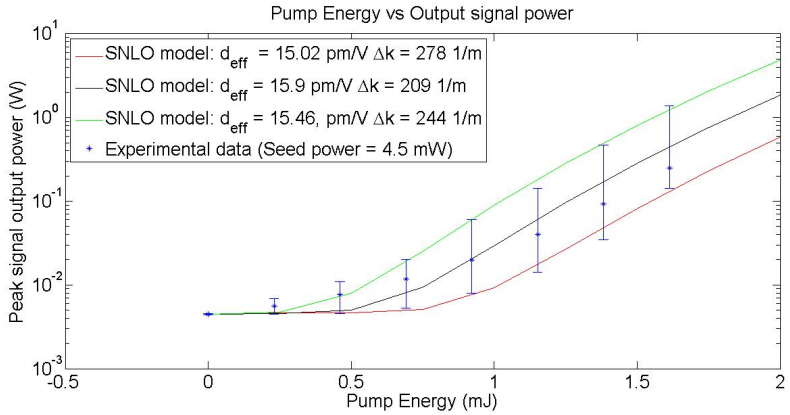
The plot also shows how crystal temperature changes the output power. The large error bars on the OPG output is due to the spontaneous emission, and because the output is generated through random processes, the output power has significantly more variation than we see with OPA. These data show that on average the OPA output is higher than the OPG output and that when the system is phase-matched, the OPA output is higher than when it is not phase-matched.

Finally we want to use the OPA data in order to estimate d_{eff} and Δk for this system. Here d_{eff} is a gain term while Δk is used as a loss term, even though its role in the model is for phase-matching. In theory the system is phase-matched because of QPM, but we do not expect to achieve maximum efficiency because the pump beam isn't well matched to the seed beam. By looking at the OPA data and fitting to the theory using d_{eff} and Δk as parameters, we can estimate these values. Considering the large uncertainty in the output, we expect a large range in these values as well. These values will be used later when modeling the output of the OPO.

Figure 3.8 includes two plots that illustrate how we can estimate d_{eff} based on the OPA data. This plot shows the best-fit from the plane-wave model to the experimental data. The best-fit was based on the coupled wave equations from the theory section and the parameters were d_{eff} and Δk. The results from the best-fit indicate that: $d_{eff} = 17.7$ pm/V and $\Delta k = 130$ 1/m. These values, along with all of the known parameters were used in the SNLO model, with the result shown. We see very poor agreement between the plane-wave model and SNLO. This is most likely due to the use of a gaussian beam in the experiment. The gain of the signal beam depends on the intensity of the pump beam, and since the plane-wave model used here does not take into account focusing of the pump beam, we should expect the plane-wave model to not accurately predict the output from experiment.



(a) Measured peak output power from OPA is plotted with a best-fit to the plane-wave model and a model produced in SNLO. The data points in blue represent the measured peak output power with error bars that represent the largest and smallest values measured at each pump energy. The red line shows the best-fit from the non-depleted pump solution, which has d_{eff} =17.7 $\frac{pm}{V}$ and $\Delta k = 130\frac{1}{m}$. Using these values in the SNLO model produces the data shown in green. The discrepancy between the plane-wave model and SNLO indicates that focusing plays a large role in the output power produced at the signal wavelength.



(b) Using the SNLO model, d_{eff} and Δk were treated as parameters and adjusted until the output fit the measured data within error. Through this method an upper and lower limit on d_{eff} and Δk were found, which will be used in the SNLO model for the OPO.

Figure 3.8: Use of the plane-wave model to fit to experimental data can create inaccuracies due to the fact that the beam is actually focusing as it propagates through the crystal. Therefore the SNLO model will provide more accurate data since it accounts for focusing of the pump and seed beams. The plot in (b) shows three models from SNLO that are used to estimate d_{eff} and Δk that will be used as inputs for the SNLO model of the OPO.

Figure 3.8b shows the resutls from three SNLO models that use a gaussian beam in the calculations, along with the experimental data. Three models are shown, using different values for d_{eff} and Δk to match the upper and lower error of the measurements along with a result near the experimental average. In an ideal scenario, d_{eff} would be on the order of 17 $\frac{pm}{V}$ assuming perfect poling, and Δk would be zero. From these models, we can reasonably assume that d_{eff} has a value between 15 and 16 pm/V and Δk has a value between 200 and 300 1/m. Values within these ranges will be used when modeling the output from the OPO.

The question arises of why Δk is nonzero, even though in the theory section we stated that maximum conversion occurs when $\Delta k = 0$. SNLO has an input field for Δk to account for phase mismatch; however, we use this input for accounting for losses in our system and various factors that may reduce the gain. Some factors include: mismatch of the focusing between the pump and seed beams as they propagate through the crystal, the high-spatial mode pump beam has different phase-fronts than the seed beam, and imperfect overlap between the pump and seed beams. The nonzero Δk value takes these factors and others into account in the SNLO model in order to get a better match to our data. By using the Δk value determined from this fit, we hope to get a more accurate model from SNLO to compare to our OPO output.

Before building the OPO, we need a baseline for the minimum output we should expect from the OPO. At the very least we expect the OPO to at least perform at the level of OPA or OPG, depending if the OPO is seeded or unseeded. This is the minimum performance we expect, but with the OPO cavity the output should theoretically be higher because of the multiple passes within the cavity. Figure 3.9 shows the output signal energy as a function of input pump energy for the case of OPG and OPA. At low energies, the OPA output is noticeably higher than the OPG output,

however this difference vanishes at higher pump energies. This is expected since at low input energies, the seed laser has a much greater impact on the amplification because it can saturate the gain, but at higher pump energies the seed laser cannot saturate the gain. These data will be compared to the OPO output energies in chapter 5.

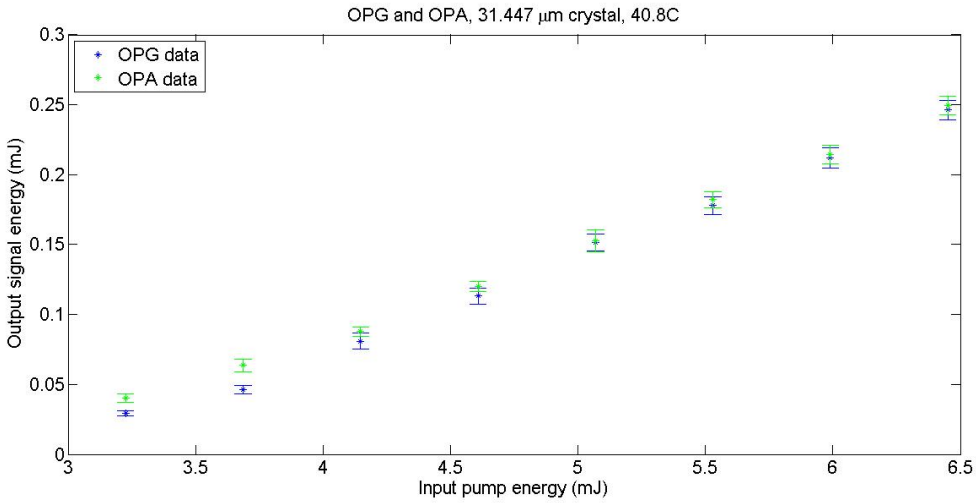


Figure 3.9: Output energy for OPA and OPG at high pump energies. These data show the OPG data in blue and the OPA data in green. Notice the relatively large difference between the OPG and OPA output at low energy, which decreases as the pump energy is increased. This is due to the relatively large impact of seeding the crystal at low pump energies.

Figure 3.10 shows the conversion efficiency of OPG and OPA as a function of input pump energy. Conversion efficiency is defined as the output signal energy divided by the input pump energy. Again, the difference between OPG and OPA is noticeable at low input pump energies, but fades at higher input energies. The conversion efficiency reaches a maximum near 4%, so we expect the OPO to have larger conversion efficiency than this.

In conclusion, with measurements of OPG and OPA, we confirmed that OPA has higher energy and a narrower spectral output than OPG due to the amplification of the seed which would otherwise be emitted at a broad range of wavelengths. This is

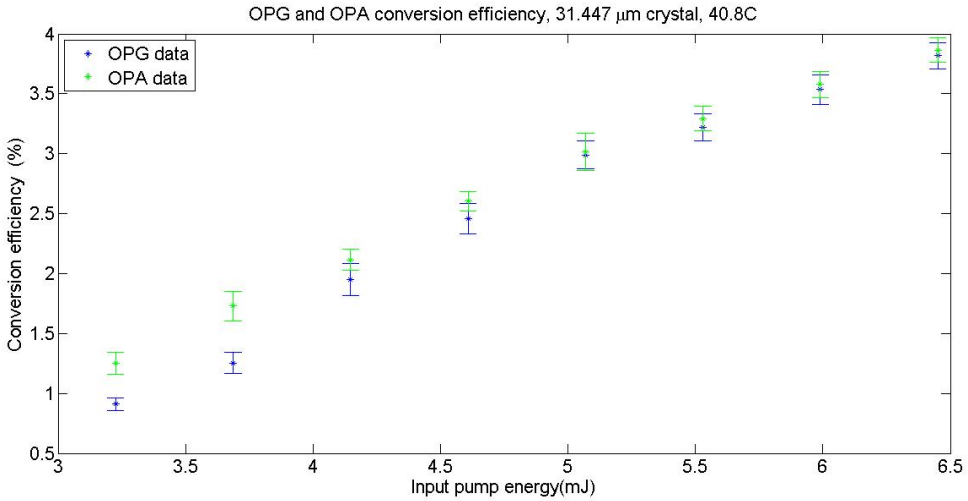


Figure 3.10: Conversion efficiency for OPA and OPG at high pump energies. The OPG data are shown in blue and the OPA data are shown in green. As in the output energy plot of figure 3.9, the difference between OPG and OPA is larger at lower energies due to the larger impact of seeding at low pump energies.

under the assumption that both spectral and spatial overlap of OPG and the seed laser is achieved. Seed power is an important consideration since at high pump energies a low-power seed laser may not be able to saturate the gain in the OPA. A low-power seed laser with 4.5 mW of power may only saturate the gain at pump energies up to about 3 mJ.

The SNLO model was used to fit the data and to estimate the values of d_{eff} and Δk from the output of the OPA at low input pump energies. We found that d_{eff} has a value between 15 and 16 pm/V and Δk has a value between 200 and 300 1/m, based on the SNLO model. These values will be used for modeling the OPO in SNLO in order to get a more accurate model to the OPO.

Finally, the output data from OPG and OPA were taken at higher pump energies so that a direct comparison can be made to the OPO output in order to set a baseline

performance for the OPO to meet. These data show that OPA and OPG reached a conversion efficiency of about 4%.

LOCKING THE OPO CAVITY

OPA is a parametric process and therefore an infinite number of signal and idler wavelengths can be found that can satisfy conservation of energy from equation 2.12. Periodic poling and phase-matching sets a bandwidth of possible signal and idler wavelengths that can be generated through the nonlinear process. However, even with perfect poling and temperature stability, the bandwidth can be very broad, on the order of tens of nanometers. Such a wide spectral linewidth has little use for the DIAL system we want to build because the output of the laser transmitter can cover many absorption features of the molecule of interest. A narrow linewidth on the order of 3 MHz is necessary from the laser transmitter to guarantee that the laser linewidth can be contained within a single absorption feature of the molecule.

One method of reducing the spectral linewidth is through the use of a cavity around the nonlinear material, which is called an OPO. An OPO has the added complexity compared to OPG and OPA because of the inclusion of an optical cavity, which is highly sensitive to temperature fluctuations that can change the length of the cavity due to thermal expansion. An optical cavity has a transmission curve that has peaks separated by the free spectral range (FSR) of the cavity. Just a small change in cavity length can easily prevent the cavity from transmitting the desired wavelength. To understand the magnitude of cavity length change that can seriously affect the trasmission, assume cavity is 12 cm in length with an index of refraction of 1 and the cavity resonates at a wavelength of 1654 nm. From *Laser Engineering* [13], the change in cavity length ΔL needed to shift the resonant mode by a frequency $\Delta\nu$ is given by

$$\Delta L = \frac{pc}{2n(\nu + \Delta\nu)} - L \tag{4.1}$$

where $p = int\left(\frac{2nL}{\lambda}\right)$ is an integer equal to 145103 based on the defined constants, L is the length of the cavity, ν is the optical frequency of the laser, n is the index of refraction inside the cavity, and c is the speed of light. To determine how much the cavity length needs to change in order to move the resonant mode by half of a FSR, we use $\Delta\nu = \frac{1}{2}\frac{c}{2nL}$. Using this and doing some algebra, we get

$$\Delta L = \frac{-L}{2p+1} \tag{4.2}$$

where ΔL is the change in cavity length. We therefore find that $\Delta L = 413$ nm, which is the cavity length change needed to change the resonant mode by half of a FSR. A change in cavity length this small can occur with minor temperature fluctuations near the optical cavity. Even a cavity length change of this magnitude will cause the transmission from the cavity to go from 100% transmission to nearly 0% transmission. We therefore need a method of adjusting the cavity length to account for the temperature fluctuations.

Locking a laser cavity so that it will always have maximum transmission at a certain wavelength is often accomplished using a mirror that can translate along the optical axis in small increments and a feedback loop to determine if the cavity length has changed and which direction the mirror needs to move if the cavity length has changed. For the OPO, we want to have maximum transmission at the generated signal wavelength and we want the seed laser field to build up inside the cavity and increase the nonlinear conversion. Therefore the optical cavity will be locked to the seed/signal wavelength. The process we use to do this is called dither locking.

Dither Locking Theory

The dither locking method involves dithering the output wavelength of the seed laser and measuring the signal transmitted through the cavity to determine if the optical cavity is on-resonance or off-resonance. We chose the seed laser since we want the OPO to be singly-resonant at the seed/signal wavelength, which means the optical cavity only resonates the seed/signal wavelength. To do this, a sinusoidal signal with a frequency ω_d from a function generator is fed into an acousto-optic modulator (AOM) that modulates the output wavelength of the light passing through it with a Doppler shift. This sinusoidally oscillates the output wavelength of the seed laser between $\lambda_o - \Delta\lambda$ and $\lambda_0 + \Delta\lambda$. Here $\lambda_0 = 1654$ nm and is the wavelength we want to lock

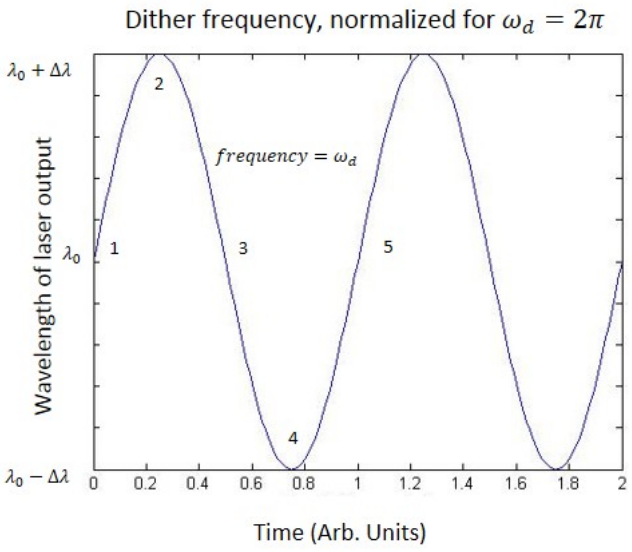


Figure 4.1: Output wavelength of the laser diode as a function of time. The dither signal from the function generator sinusoidally changes the output wavelength of the laser diode at frequency ω_d.

the cavity to and $\Delta\lambda$ is the maximum wavelength change due to the dithering. We want $\Delta\lambda$ to be much smaller than the FWHM of the resonant peak of the cavity.

The dither signal V_{dith} is a sinusoidal function that describes how the laser diode wavelength changes as a function of time, such that

$$V_{dith} = Bsin(\omega_d t) \tag{4.3}$$

where B is a constant and V_{dith} oscillates at frequency ω_d. The plot in figure 4.1 shows the dither signal as a function of time with λ_o and the maximum and minimum wavelengths labeled.

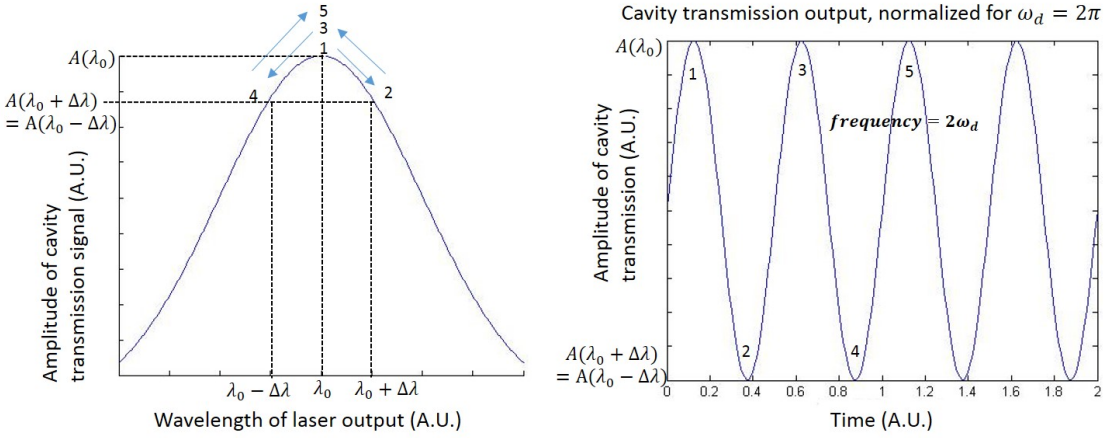


Figure 4.2: When the cavity is resonant at λ_0, the cavity transmission signal will oscillate at $2\omega_d$ because of the dithering of the laser diode. This is verified by following the sequence of numbers in figure 4.1 and in the left and right images.

Next we want to consider how dithering has an impact on the measured output. Consider the situation in which the OPO cavity is resonant at λ_o, the seed laser wavelength, so that $\lambda = \lambda_0$, where λ is the resonant wavelength of the OPO cavity at any given time. This is shown in figure 4.2. While the seed laser wavelength is dithering in time, the cavity transmission also changes in time due to the resonant condition of the cavity. The resonant peak is an Airy function with a width that is dependent on the properties of the cavity from equation 5.3. To simplify the theory,

we estimate the peaks of the Airy function to have a gaussian shape. As the seed laser wavelength dithers, the cavity transmission signal traces out this gaussian function, as shown on the left side of figure 4.2. When the seed laser dithers away from the resonant peak, the cavity transmission amplitude $A(\lambda)$ decreases. If we measure the cavity transmission amplitude in time, a plot shown in the right half of figure 4.2 is produced.

Based on the image on the right side of figure 4.2, the output cavity transmission has an equation of the form

$$V_{cav} = \Delta A sin(2\omega_d t) + (A(\lambda_0) - \Delta A) \tag{4.4}$$

where ΔA is half of the peak-to-peak amplitude of the output voltage and depends on λ_o and $\Delta\lambda$. We can see from the figure above that when the laser diode dithers its output wavelength at a frequency of ω_d (left image), the detected cavity transmission power oscillates at frequency $2\omega_d$ (right image). The numbers in the images correspond to the numbers in the dither frequency plot of figure 4.1. At 1, the laser diode wavelength is at λ_0, then at 2 it increases to $\lambda_0 + \Delta\lambda$, and so on. Using this same technique we can also look at what happens when the cavity is off resonance (when $\lambda \neq \lambda_0$).

Next, consider when $\lambda > \lambda_0$ and therefore the seed laser is off-resonance in the cavity. The cavity transmission plot is shown in figure 4.3. The figure on the left side shows how the cavity transmission changes as the seed laser wavelength is dithered. When plotted as a function of time, the cavity transmission has a form like that on the right side of the image, which is in phase with the dither signal.

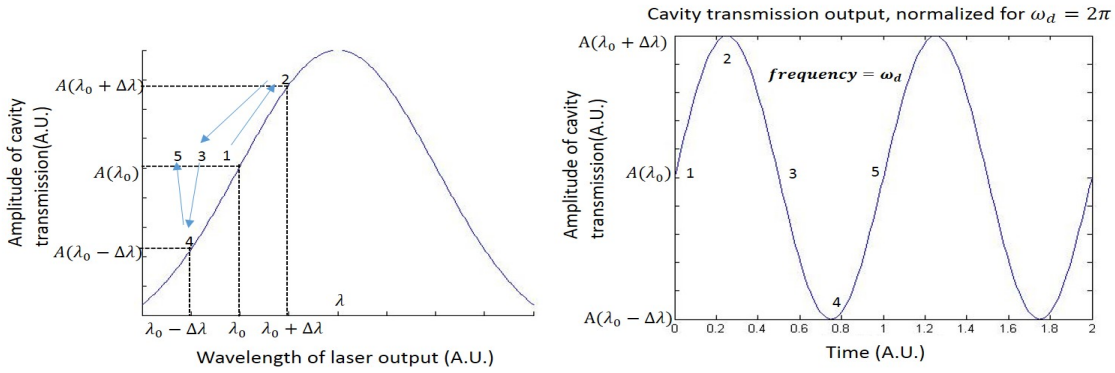


Figure 4.3: When the cavity is off resonance, the cavity transmission signal will oscillate at ω_d. In this case, where $\lambda > \lambda_0$ the cavity transmission signal is in phase with the dither signal.

In this case, the cavity transmission would have an equation of

$$V_{cav} = \Delta A sin(\omega_d t) + A(\lambda_0) \tag{4.5}$$

which oscillates at ω_d.

Similarly, when $\lambda < \lambda_0$, the cavity transmission as a function of time oscillates at ω_d. The plot on the left side of figure 4.4 shows how the cavity transmission signal is produced in this case. As the laser diode signal dithers in time at frequency ω_d, the cavity transmission changes in time at frequency ω_d. Here the cavity transmission is out of phase with the dither signal.

In this case, the cavity transmission equation is

$$V_{cav} = \Delta A sin(-\omega_d t) + A(\lambda_0) = -\Delta A sin(\omega_d t) + A(\lambda_0) \tag{4.6}$$

where we see that when $\lambda < \lambda_0$ the output cavity transmission also has a frequency of ω_d but has a π phase shift as well. This is a useful feature because we will be able to

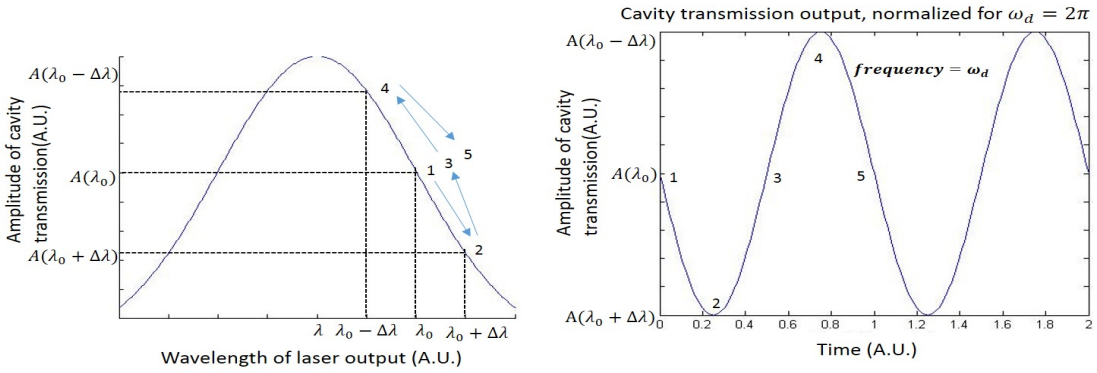


Figure 4.4: Again when the cavity is off-resonance, the cavity transmission signal oscillates at ω_d, however since $\lambda < \lambda_0$, the output is out of phase with the dither signal. This is useful because we can determine the side of the resonant peak where λ_o is located.

determine if the cavity is resonating at a higher or lower wavelength than the desired wavelength of λ_0.

Another important note is that as λ approaches λ_0, the amplitude of the oscillating cavity transmission, ΔA, decreases and has the smallest value when $\lambda = \lambda_o$. Additionally, the frequency of oscillation of V_{cav} will have a component at ω_d except when $\lambda = \lambda_o$ where it then oscillates at $2\omega_d$. From these examples we see that the cavity transmission changes in a predictable way based on how far from resonance the cavity is. When the cavity is on-resonance at λ_0, the magnitude of the terms that oscillate at ω_d is zero. When off-resonance, the magnitude of the terms oscillating at ω_d is ΔA and depends on the difference between λ_o and λ and the size of $\Delta\lambda$. The size of ΔA is a relative measure of how far off resonance the cavity is and therefore is proportional to the length the cavity must change to be resonant at λ_o.

Experimentally, the magnitude of the terms that oscillate at ω_d is measured using a lock-in amplifier. This signal out of the lock-in amplifier is called the error signal $\epsilon(\lambda)$ and is proportional to ΔA. Based on the three cases of resonance discussed

previously, we can predict the shape of the error signal as a function of λ. This is shown in the plot in figure 4.5. When on-resonance ($\lambda = \lambda_0$), the error signal is zero. When off-resonance in one direction ($\lambda > \lambda_0$) then the error signal is positive and increases as $\Delta\lambda$ increases. And when off-resonance in the opposite direction ($\lambda < \lambda_0$) the error is negative and decreases as $\Delta\lambda$ increases. Based on this, the error signal as a function of λ should look like the derivative of the resonance feature. To simplify the theory, we assumed the resonance feature has a gaussian shape and therefore the error signal is the derivative of a gaussian, as shown in figure 4.5.

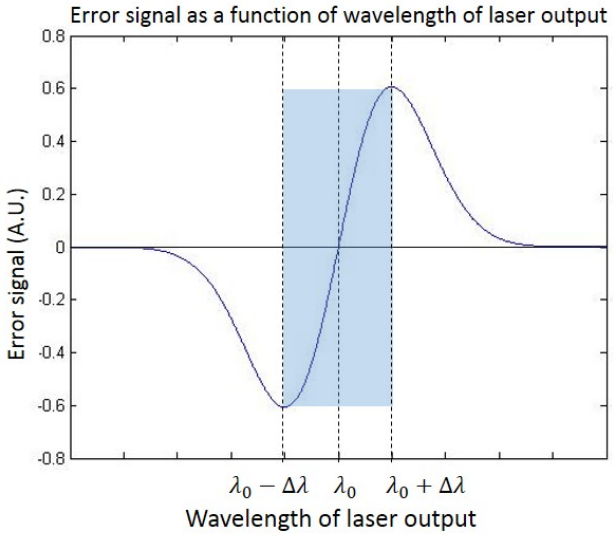


Figure 4.5: Error signal as a function of cavity resonance. Notice when the cavity is resonant at λ_0 ($\lambda = \lambda_0$) the error signal is zero. Inspection of the previous images reveals that in order for the locking system to be able to maintain resonance, the wavelength must stay within the shaded region, which corresponds to $\Delta\lambda$ of less than the half width of the resonance feature.

Figure 4.5 shows how the error signal changes as the resonant wavelength of the cavity changes. As the cavity approaches the desired resonant wavelength λ_0, the error signal approaches zero. Also we want the cavity to stay within the shaded

region on the plot because the system will not know which way it needs to adjust to go back to resonance if it passes out of the shaded region.

Methods for Dither Locking

For locking the cavity, one important piece of equipment we need for this system is a piezo-electric transducer (PZT). The PZT is made of a special kind of ceramic that has a known dependence of applied voltage on length. Generally a PZT will expand a few nanometers with a few kilovolts of applied voltage and we can use it to achieve precise length changes that we need to counteract the temperature effects on cavity length. One of the cavity mirrors is mounted to the PZT so that the cavity length can be changed by precise amounts, which is proportional to the magnitude of the error signal.

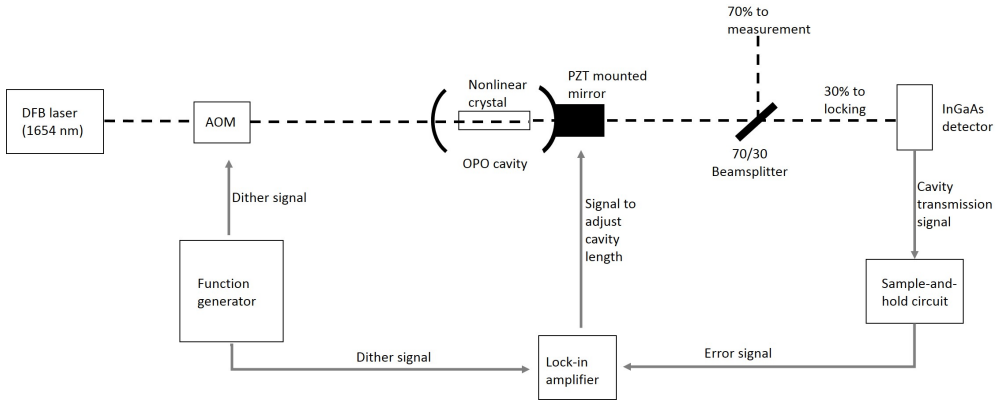
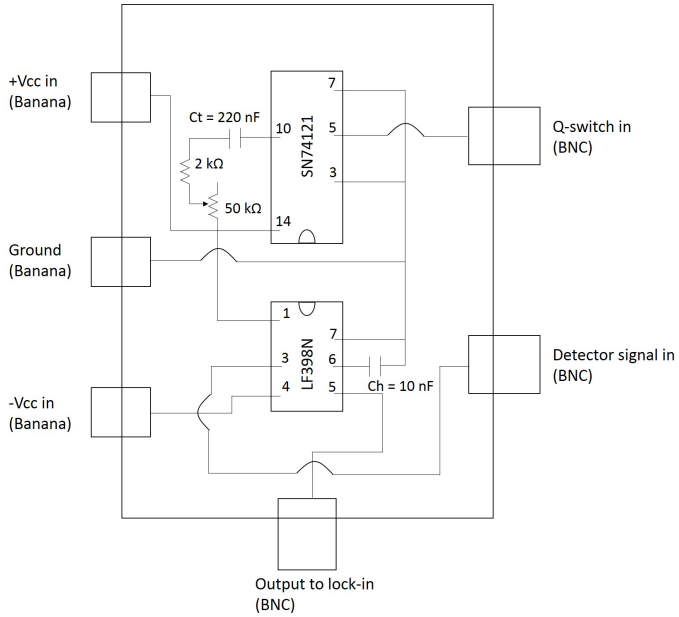


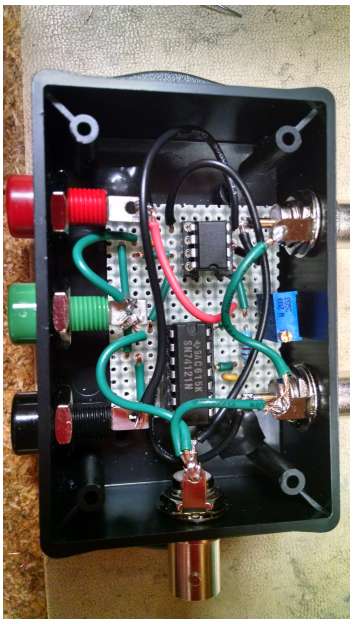
Figure 4.6: Block diagram of the dither locking setup for the OPO. The seed laser operates at 1654 nm and the wavelength is dithered with an AOM and function generator. One mirror of the cavity is mounted on a PZT for fine adjustment of the cavity length. The signal transmitted through the cavity is measured on an InGaAs detector. This information is sent to a lock-in amplifier which extracts the amplitude of signals oscillating at the dither frequency to create the error signal. The error signal is proportional to the cavity length change required to keep the cavity on resonance at 1654 nm.

A block diagram for dither locking is shown in the following figure 4.6. The DFB laser shown is the seed laser at 1654 nm and is incident on an AOM (Isomet 620C-80 driver and 1205C-2 modulator) that oscillates the seed laser wavelength at the dither frequency through the use of a function generator. The modulated seed laser is incident on the OPO cavity and the amount of light that is transmitted through the cavity depends on the wavelength of the seed laser as it modulates and the cavity resonance. The output from the cavity is split by a beamsplitter and a small amount of the light is sent to a very sensitive InGaAs detector (New Focus 2011) that measures the cavity transmission signal. This detector has sufficient bandwidth to detect signals that oscillate at ω_d. The cavity transmission signal is fed into a lock-in amplifier which filters at the dither frequency ω_d, and generates an output called the error signal that is proportional to the distance the PZT needs to move in order for the cavity to be on-resonance again. A large amplitude oscillating at ω_d indicates that the cavity length needs a large adjustment and a small amplitude indicates a small adjustment is necessary. The error signal is zero when the seed laser is on-resonance.

In order to achieve effective locking, we need a circuit to process the detector signal so that it is in a usable form for the lock-in amplifier. The major issue with the detector output is that it will have strong peaks due to the incoming signal wavelength that was generated through the pulsed OPO process. When the relatively high-intensity signal pulse reaches the locking detector, the detector can oversaturate, which can create a small valley in the detector output. This small valley can be mistaken for a peak while locking, since it will also produce an output at $2\omega_d$. This makes locking especially difficult, since it occasionally locks onto this valley. If we develop a circuit that can ignore this valley, then locking will be significantly easier.



(a) Circuit diagram for the shutter circuit used to ignore the large signal pulses that are present at the detector that measures the cavity transmission signal. A Schmitt trigger is used in conjunction with a sample-and-hold in order to time the arrival of the large signal pulse and to set how long to ignore this pulse. A variable resistor is used to fine-tune this hold time.



(b) Image of the shutter circuit used in the locking system. The Schmitt trigger (top) and sample-and-hold (bottom) chips are shown. Power is supplied at ± 5 volts and ground with banana plug sockets (left). Input and output signals are supplied via BNC cables (bottom and right).

Figure 4.7: Image of the packaged shutter circuit with the connections for the locking circuit. The circuit is powered with a standard power supply and three coaxial connectors are used for the inputs and outputs, which include the Q-switch (input), detector signal (input), and the corrected cavity transmission signal (output) which is used as the input to the lock-in amplifier.

To make this circuit, we used a Schmitt trigger (SN74121) along with a sample-and-hold (LF398N). The Schmitt trigger looks for an edge of a TTL signal and produces a square wave that starts at the beginning of the rising edge and ends after a time t_w determined by a resistor and capacitor, where

$$t_w = (0.7)C_t R_t$$

This sets the length of time we want the lock-in to ignore the signal from the detector. The time needs to be long enough to block out the valley from the detector signal, but short enough so that the cavity doesn't change too much over the time.

As shown in the circuit diagram in figure 4.7a we used a 50 kΩ variable resistor and a 2 kΩ resistor for R_t with a 220 nF capacitor for C_t. The resulting pulse width from the Schmitt trigger is therefore 6 ms when the variable resistor is set to 25 kΩ. Figure 4.7b shows an image of the shutter circuit packaged for use with the locking system.

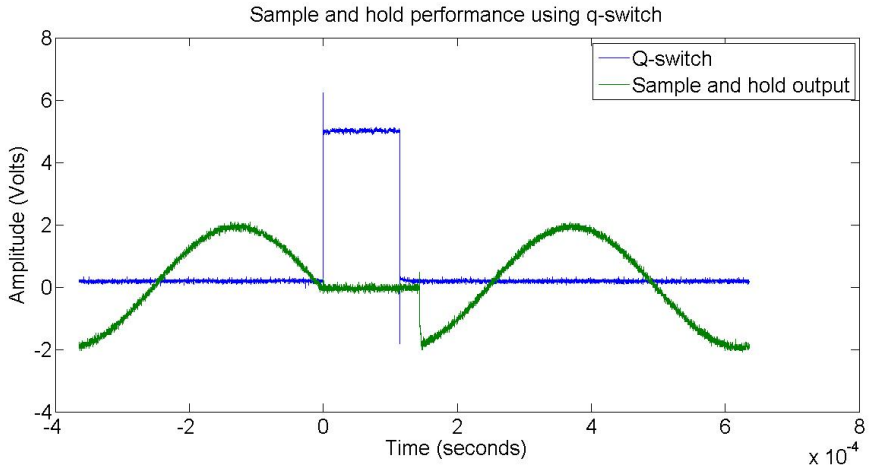


Figure 4.8: Output from the shutter circuit with a sine wave input. The circuit triggers on the Q-switch pulse (blue) and the output from the shutter circuit (green) holds the input at the value that occured at the start of the Q-switch pulse. The amount of time that the output is held at this value depends on the resistance and capacitance in the circuit. This plot shows that the shutter circuit works as expected.

The Schmitt trigger receives a TTL signal from the Q-switch of the pump laser, which occurs just before the arrival of the large signal pulse at the detector. The output from the detector is sent to the shutter circuit so that the large pulse can be removed from the signal before sending it to the lock-in amplifier. The sample and hold uses the output from the Schmitt trigger and holds the value of the input for the

duration of the square wave from the Schmitt trigger. By using the sample and hold, we prevent the system from making changes to the cavity length while the Schmitt trigger is on. Figure 4.8 shows the effect of the sample and hold circuit on a sinusoidal input. The output from the shutter circuit is the corrected cavity transmission signal and is used as the input to the lock-in amplifier.

Results from the Locking System

The output from the lock-in amplifier is a DC voltage that corresponds to how far from resonance the cavity is. We call this the error signal for the locking circuit. Since the process of dither locking produces an error signal that is proportional to the slope of the cavity resonance feature, then the error signal is the derivative of resonance feature. A plot of the error signal produced when scanning a 90% - 90%, flat-flat cavity is shown in figure 4.9. The green line represents the PZT voltage, showing how the cavity length is changing, and the blue line represents the cavity transmission signal.

Many parameters come into play when dither locking that affect the stability and quality of the lock. An unstable lock on the cavity can easily fall off resonance with the seed laser, and a low-quality lock results in a broad linewidth of the resonance. The parameters involved in the quality and stability of the locking include: dither frequency (must be fast enough to be detected by the lock-in and fast enough to respond to changes in the cavity length), amplitude of the dither signal (sets how far from the input wavelength the AOM can modulate the wavelength of the seed laser), lock-in sensitivity (sets the size of the voltage of the error signal out of the lock-in which affects stability and quality), detector gain and laser power (coupled with the lock-in sensitivity, these contribute to the size of the error signal), among others.

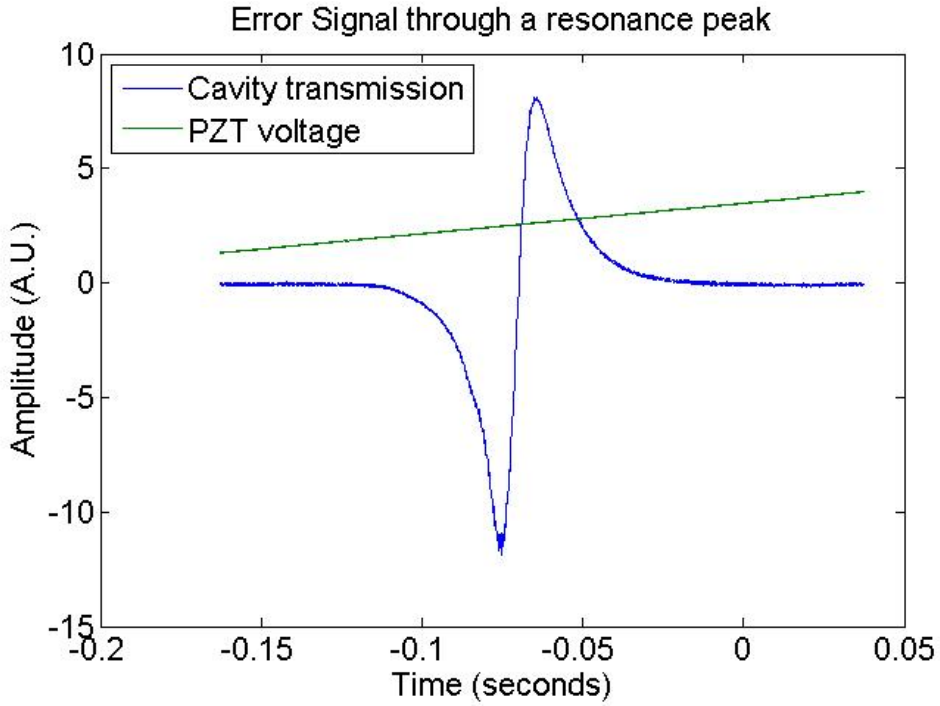


Figure 4.9: As the cavity length is changed by changing the PZT voltage (green) the cavity transmission (blue) moves through a resonant feature. The cavity begins off-resonance, then to the side of the resonant feature, through zero (which indicates the peak of the resonant feature), to the other side of the resonant feature, and finally back to zero where it is off-resonance again.

Most of the parameters are dependent, and careful adjustment of these parameters is necessary to achieve a stable and high-quality lock. Figure 4.10 shows a long time scan of cavity locking while the stability was tested by touching the mirror mounts or pressing on the optical table. This plot shows that even over long times and with external disturbances, the locking circuit can keep the cavity locked to the resonance feature.

The shutter circuit is a major reason for our success with locking the laser. Without this circuit, locking was impossible or short-lived. Because of this circuit we were able to observe the error signal as it passed through a resonant feature of the cavity. Overall, the dither locking circuit is working as intended and can counteract

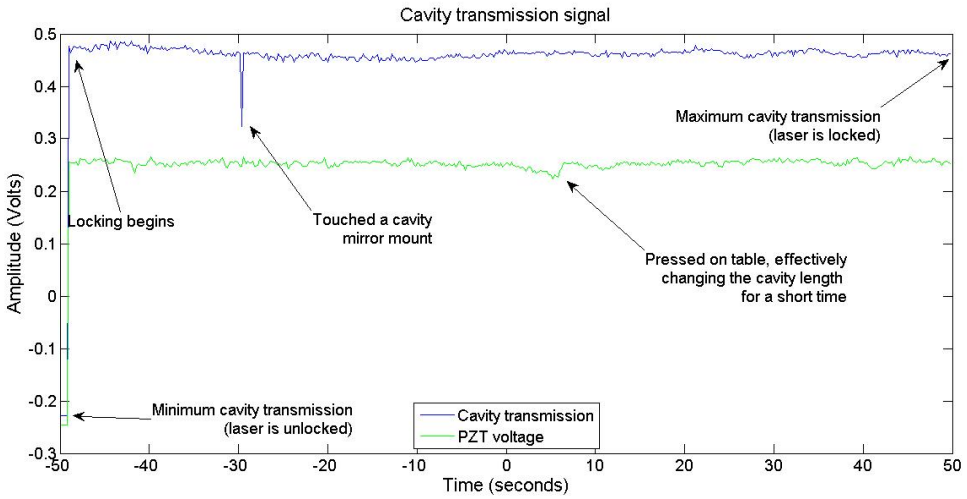


Figure 4.10: Test of the locking system showing the cavity transmission and PZT voltage over a long time scan with external disturbances. The cavity transmission (blue) starts off-resonance and quickly moves to its maximum value, indicating it is on-resonance. With external disturbances like touching a mirror mount or pressing on the optical table, the locking circuit is able to recover and maintain locking.

external effects like temperature swings and mechanical disturbances. We have been able to lock the optical cavity for lengths of time on the order of hours, which is more than enough time necessary to collect data from the system.

Limitations of the System and Future Work

A common method of laser locking is the Pound-Drever-Hall (PDH) method [14], which allows for precision laser locking and initially we considered using this method. However the downfall of this method for this application is that it utilizes polarization changes to determine if the laser is on- or off-resonance. Unfortunately, nonlinear optics are dependent on the polarization, and to access the high-conversion coefficients requires certain polarization of the incoming beams. The PDH method would alter the necessary polarization to achieve high conversion and would therefore result in little or no conversion to 1654 nm. Dither locking is much simpler than methods

like PDH; however, it has limitations on the speed of locking and the narrowness of the resonance feature that can be locked to. For the purposes of this OPO, these limitations shouldn't be a problem since the finesse of the OPO is relatively small, on the order of 10.

Another limitation is the simple feedback loop used in this system. The feedback loop only checks for the current state of the locking without any consideration for how the cavity is changing in time. Therefore if the system was constantly heating, the locking system will continue to lock until a limit in the PZT voltage is reached. At this point, the system cannot lock unless the PZT bias is adjusted. Implementation of a proportional-integral (PI) feedback loop for this system will allow us to circumvent this issue. The PI circuit will be built in future efforts for this project, which will help the cavity stay locked for longer periods of time.

OPTICAL PARAMETRIC OSCILLATOR

As seen in the OPA/OPG section, the use of injection seeding increases the conversion of the parametric nonlinear process and makes a narrower spectral output, both of which are necessary for the DIAL laser transmitter discussed in chapter 1. The same concept can be applied to an OPO with similar results expected. To draw a parallel to OPG and OPA, where OPG has just the pump beam at the input to the crystal and OPA has the pump and a seed laser at the input, an OPO can be defined in a similar way as an unseeded OPO and a seeded OPO. The only difference between these is that the seeded OPO has a seed laser beam at the input to the cavity in addition to the pump beam.

An OPO has the added complexity compared to an OPG and OPA because of the inclusion of an optical cavity, which is highly sensitive to temperature fluctuations and external vibrations that can change the length of the cavity due to thermal expansion. As discussed in chapter 4, the cavity length is locked using a process called dither locking so that the seed laser resonates and allows the seed laser field to build up inside the cavity and therefore increases the efficiency of the conversion process.

Methods and Setup

Measurements of the OPO included in this section are performed when the OPO is either locked or unlocked. Therefore the OPO measurements can be one of the following: seeded locked, unseeded unlocked, or seeded unlocked. Note that the OPO cannot be unseeded locked because the seed laser is required to achieve locking.

For the singly-resonant OPO, the seed/signal wavelength must be resonant in the optical cavity. Under the best-case scenario, we want the seed laser to perfectly match the lowest-order mode of the cavity and we want the pump to nominally have

the same shape. This is a difficult task that involves focusing the seed laser to have a specific profile at a certain location in space in addition to focusing the pump in the same way. If the seed laser matches this lowest order mode, then the output from the optical cavity as a function of wavelength will be an Airy function with peaks separated by the free spectral range (FSR) of the cavity. In terms of optical frequency, the FSR ($\Delta\nu$) is

$$\Delta\nu = \frac{c}{2nL} \tag{5.1}$$

and the finesse $\mathcal{F}$ is defined as the FSR divided by the width of the peaks ($\delta\nu$), where

$$\mathcal{F} = \frac{\Delta\nu}{\delta\nu} = \frac{\pi(R_1R_2)^{1/4}}{1-\sqrt{R_1R_2}} \tag{5.2}$$

The Airy function is the theoretical cavity transmission from a Fabry-Perot that is described with the following equation [15]

$$T = \frac{1}{1+(4\mathcal{F}^2/\pi^2)sin^2(\delta/2)} \tag{5.3}$$

where $\delta = 2kL$ is the round-trip phase shift in the cavity and $k = \frac{2\pi}{\lambda}$ is the wavenumber. These equations are used to plot the theoretical cavity transmission based on the parameters of the cavity.

The OPO cavity consists of two mirrors and the nonlinear crystal. The mirror configuration is a flat mirror with nominally 95% reflectivity at 1654 nm as the input mirror and nominally 45% reflectivity (at 1654 nm) curved mirror at the output with a radius of curvature of 0.5 m. Both mirrors are assumed to have no absorption at the pump, signal, or idler wavelengths. The reflectivity of the mirrors at the idler wavelength is estimated to be 30%. At the pump wavelength the reflectivity for each

mirror is estimated to be 30% for the flat mirror and 20% for the curved mirror. The flat mirror is mounted on a piezo-electric transducer (PZT), as shown in figure 5.1. A PZT is a device made of a special ceramic material which under an applied voltage expands a length proportional to that voltage and is used in this system both for aligning the cavity and for locking the cavity. When a sawtooth-like voltage signal is applied to the PZT, the cavity length will change in a proportional manner. This effectively scans the cavity so that the cavity transmission curve can be observed, which is useful for alignment of the cavity. The PZT is used for the locking system in order to maintain the cavity length that resonates the seed laser.

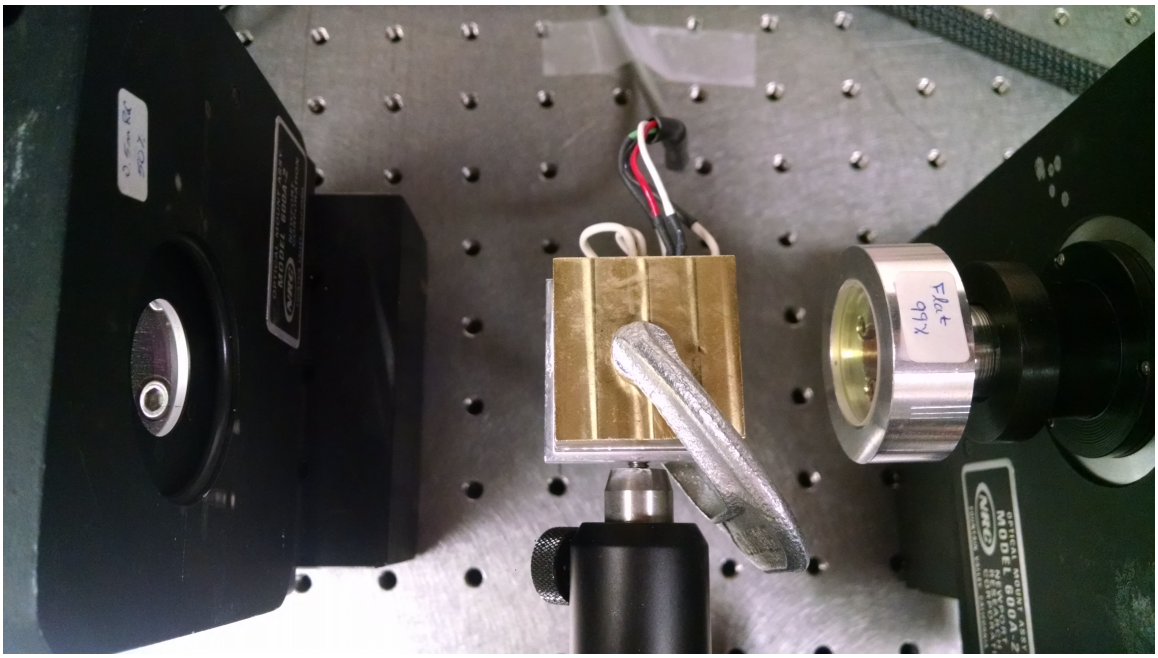


Figure 5.1: Image of the OPO cavity. The flat mirror (right) is mounted on a PZT and has nominally 95% reflectivity at the signal wavelength. The output mirror (left) is a curved mirror with radius of curvature 0.5 m and 45% reflectivity at the signal wavelength. The nonlinear crystal is enclosed in a brass heater (center) with only the input and output faces of the crystal exposed.

As in the OPG and OPA measurements, the crystal is a 30 mm long magnesium-oxide-doped lithium niobate crystal (MgO:$LiNbO_3$) that has a poling period of 31.447

μm. The input and output faces are 2 mm square with anti-reflection coatings for the pump, signal, and idler wavelengths. A brass heater encloses the crystal except for the input and output faces and allows for even temperature distribution in the crystal. This is shown in figures 5.1 and 3.3.

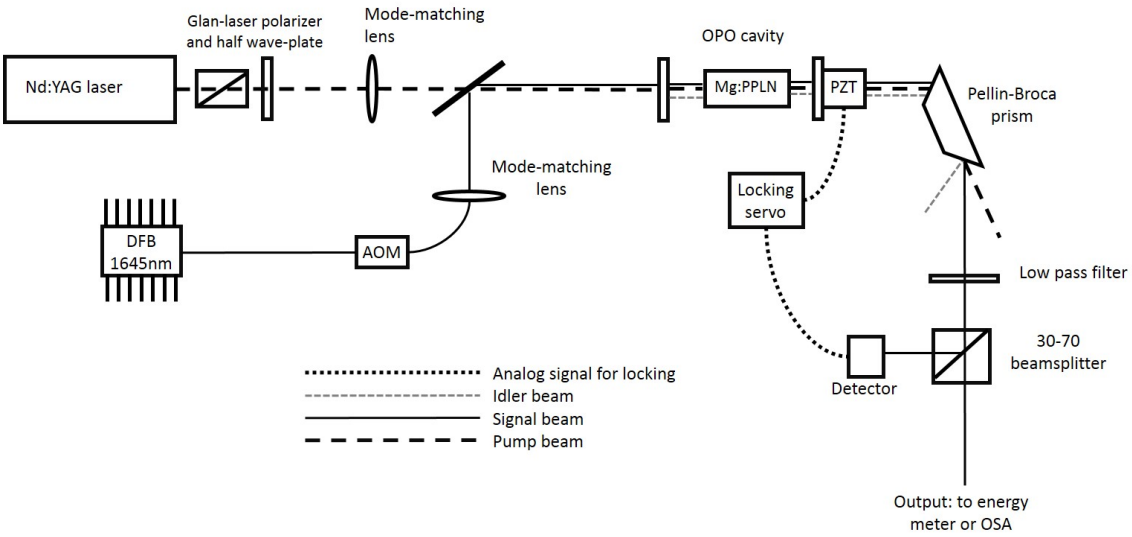


Figure 5.2: Block diagram of the OPO setup. The Nd:YAG laser at 1064 nm is the pump for the OPO and a glan-laser polarizer and half wave-plate are used to set the energy. The pump beam is focused into the optical cavity with the goal of matching the seed laser profile. A DFB diode laser at 1654 nm is used as the seed laser, which passes through an AOM to modulate the wavelength for the locking circuit. The beam is focused into the cavity with the goal of matching the lowest-order mode of the cavity. The Mg:PPLN crystal is located inside the cavity and a PZT is mounted onto one of the cavity mirrors for the locking circuit. A Pellin-Broca prism separates the outputs from the OPO by wavelength and a filter is used to ensure all pump light is extinguished. A beamsplitter sends 30% of the signal beam to the locking circuit with the remainder used for measurements of the OPO performance.

Figure 5.2 shows a block diagram of the entire OPO setup. As in chapter 3, a flashlamp-pumped, Q-switched Nd:YAG laser with a maximum output energy of 75 mJ at 1064 nm and 10 ns pulses is used as the pump laser (Big Sky Laser ULTRA series). The output energy is varied using a glan-laser polarizer and a half-wave plate.

The seed laser is a DFB laser diode with an output of 1654 nm and has a peak output power of 5 mW (Eblana Photonics EP1654-DM-B01-FM). An AOM (Isomet 620C-80 driver and 1205C-2 modulator) modulates the output wavelength of the seed laser for laser locking. Mode-matching lenses are used to focus the beams approximately to the lowest-order mode of the optical cavity. The beams are collinear into the cavity, determined through the use of an IR camera. The various beams at the output are separated by wavelength with two Pellin-Broca prisms (one shown) and filtered to extinguish any scattered pump light. Through the use of the prisms and the filter, only the signal wavelength should be present at the 30-70 beamsplitter, which splits 30% of the signal light to use for the locking circuit while the remaining 70% is used for the measurement. The output is either measured on an optical spectrum analyzer (OSA) to measure the spectrum or with an energy meter to measure the energy out of the system. Figure 5.3 shows a picture of the full setup including all of the equipment used.

The primary measurements needed to test the performance of the OPO are measurements of the output signal energy and spectra of the signal output. The block diagram of figure 5.2 shows the output where these measurements are made. Energy measurements are made with a Thorlabs energy meter (model number PM100D meter and ES111C head) placed at the output. Spectra are collected by coupling the output into a multimode fiber at the output. The fiber is then connected to the OSA which is an Agilent system with model number 86142B. The OSA has an optical resolution limit of 0.06 nm.

The energy out of an OPO can have variation from pulse to pulse and we account for this variation by measuring over 100 output pulses for each input energy value. The energy meter calculates the mean and standard deviation (σ) and the error is

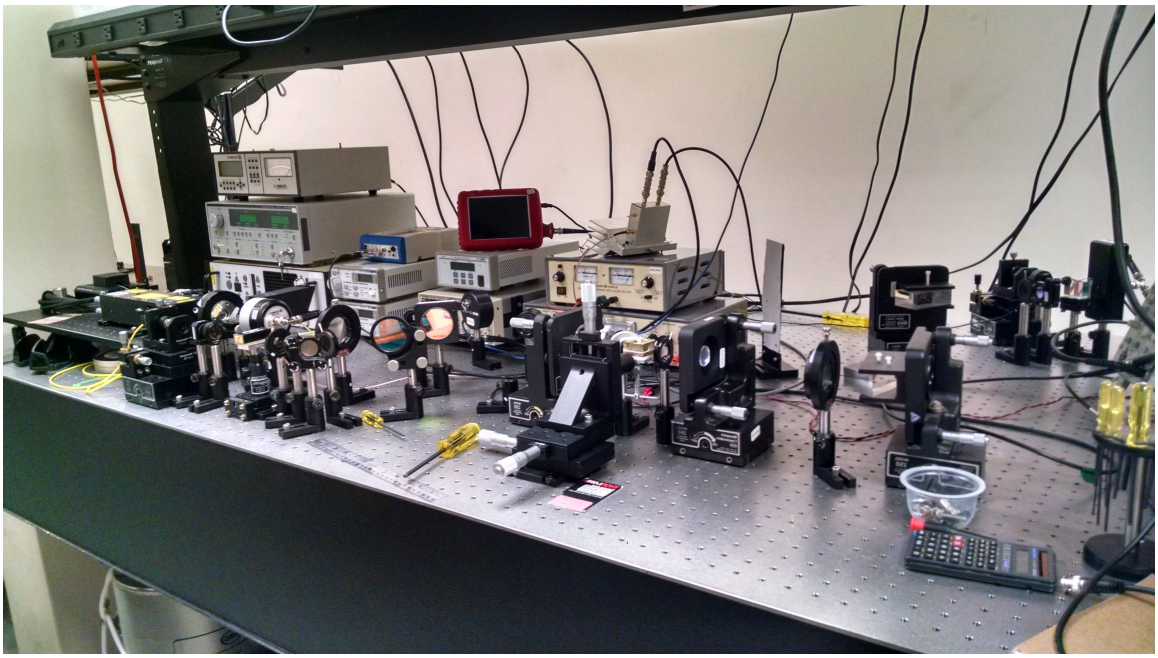


Figure 5.3: Image of the full setup used for the OPO measurements. The pump and seed lasers are located on the left side of the image, along with the controls for the lasers and the crystal heater. Various optical components, shown in more detail in figure 5.2, direct the beams to the OPO cavity, pictured near the center of the image. Prisms and filters separate the various output beams by wavelength so that only the signal wavelength is measured at the output, shown on the right side of the image.

calculated with $\frac{3\sigma}{\sqrt{N}}$, where N is the number of samples per point and is usually 100 for the data collected. The errors are shown as errorbars on the energy output plots.

Spectra of the OPO output are taken at the maximum resolution of the OSA (0.06 nm) with a high sensitivity between -80 and -85 dBm. Measuring the spectrum of a pulsed laser is difficult with a scanning OSA like the one used in this experiment. The issue is that the pulses are so short (about 10 ns) that it is very likely for the OSA to 'miss' the output while it is scanning. The high sensitivity makes the OSA scan much slower and makes it more likely to catch the pulse. The spectra are also averaged over 10 to 20 scans to reduce noise. However, the amplitude of the spectral outputs for the pulsed OPO is still somewhat arbitrary, especially when compared to

a CW output like the seed laser. We must take caution when making comparisons of the two.

Results

Measured and Expected Cavity Transmission

The seed laser power into the cavity is 1.0 ± 0.1 mW and the seed laser out of the cavity is 0.25 ± 0.03 mW when the cavity is locked. The loss of power through the cavity indicates poor coupling into the cavity. Since the seed laser doesn't match the lowest-order mode of the cavity, some of the power cannot transmit through the cavity. Future work will include optimization of the coupling into the cavity.

Cavity FSR Plot with Comparison to Theory

The PZT voltage can be scanned in such a way that the voltage in time traces out a sawtooth function. Doing this while the seed laser is on will scan through the cavity lengths where the seed laser can be transmitted, similar to a scanning Fabry-Perot. This method of scanning is used to align the seed laser into the cavity and optimize the coupling.

The plot shown in figure 5.4 shows the data from the optimized 50% - 99% cavity that makes up the OPO. The green function is the PZT voltage and the blue function shows the cavity transmission measured on the InGaAs detector from the locking circuit. The large peaks show that the seed laser is resonating at the lowest-order mode of the cavity. However the peaks on the left of the large peaks indicate that the seed laser is also resonating at higher-order modes as well. Better mode-matching into the cavity would help prevent the seed from resonating at these higher-order modes. Ideally, we want a transmission curve that only includes the one resonant peak.

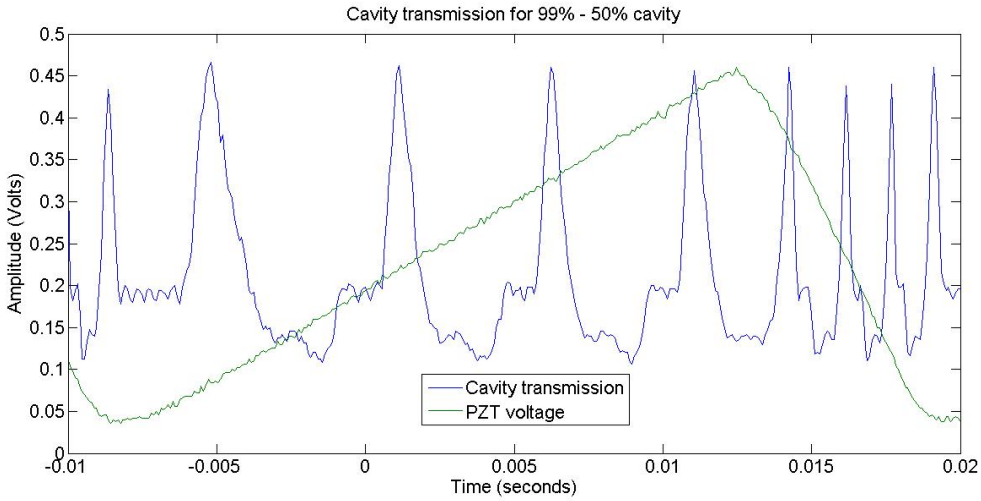


Figure 5.4: Cavity transmission from the OPO cavity with the seed laser coupled. The smaller peaks in the plot indicate imperfect coupling and the seed laser resonating at modes other than the lowest-order mode. Ideal coupling would result in a cavity transmission plot that only included the tallest peaks.

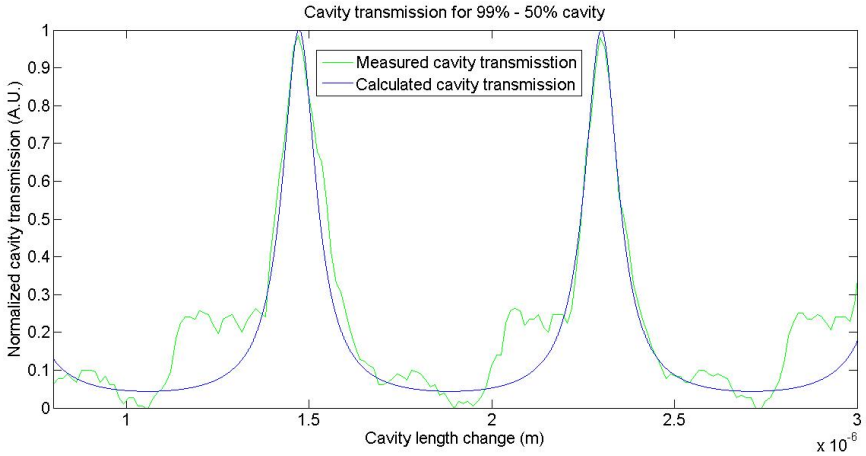


Figure 5.5: Measured cavity transmission from the OPO plotted with the theoretical cavity transmission from the Airy function. The theoretical cavity transmission shows what the output would look like if only the lowest-order mode was resonant in the OPO cavity.

To compare the cavity transmission to what is expected from theory, equations 5.2 and 5.3 were used to plot an Airy function that has peaks seaparated by

the FSR, $\Delta\nu$, and FWHM width of $\delta\nu$. Figure 5.5 shows the Airy function plotted with the cavity transmission from figure 5.4. This figure shows the theoretical cavity transmission curve in green, which assumes only the lowest-order mode of the cavity resonates. The blue curve shows the measured cavity transmission curve. The two curves have been normalized for comparison. This further illustrates the additional modes that are present in the measured cavity transmission. Although the coupling into the cavity is not ideal, this setup was used for the OPO and future work will include optimizing the cavity mode-matching to better resonate the lowest order mode.

Unseeded Unlocked OPO
Data with OPG Comparison

The unseeded unlocked OPO is equivalent to OPG but with an optical cavity around the nonlinear crystal. Therefore only the pump beam is incident on the cavity for the case of the unseeded unlocked OPO. Without the seed laser in the cavity, locking is not possible with dither locking.

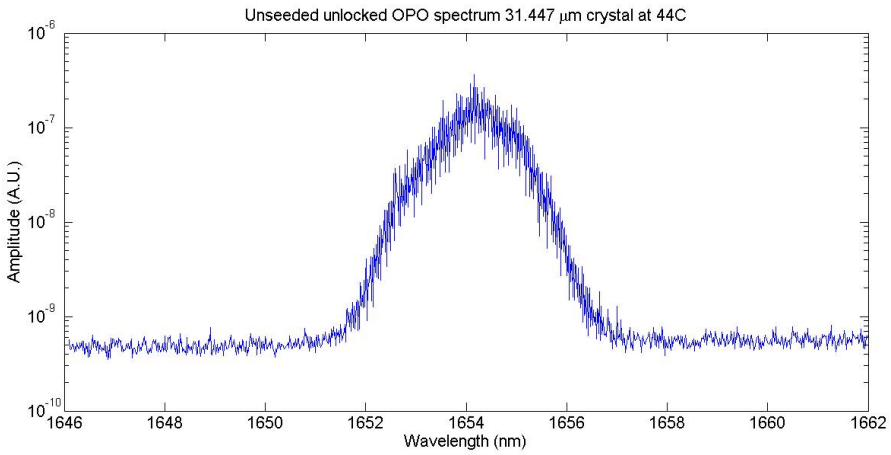


Figure 5.6: Spectrum from the unseeded unlocked OPO with pump energy of 1.5 mJ. Since the signal wavelength in an unseeded OPO is generated through spontaneous emission, the output is broadband.

Much like OPG, the unseeded unlocked OPO spectrum shows the bandwidth of signal wavelengths that can be generated based on phase-matching. Figure 5.6 shows the spectrum of the unseeded unlocked OPO with the input pump energy at 1.5 mJ. To see how the unseeded unlocked OPO spectrum changes when the pump energy is increased, figure 5.7 shows the spectrum from the unseeded unlocked OPO with the pump energy at 2.5 mJ. It is clear that the spectrum is broadened in comparison to the spectrum from figure 5.6.

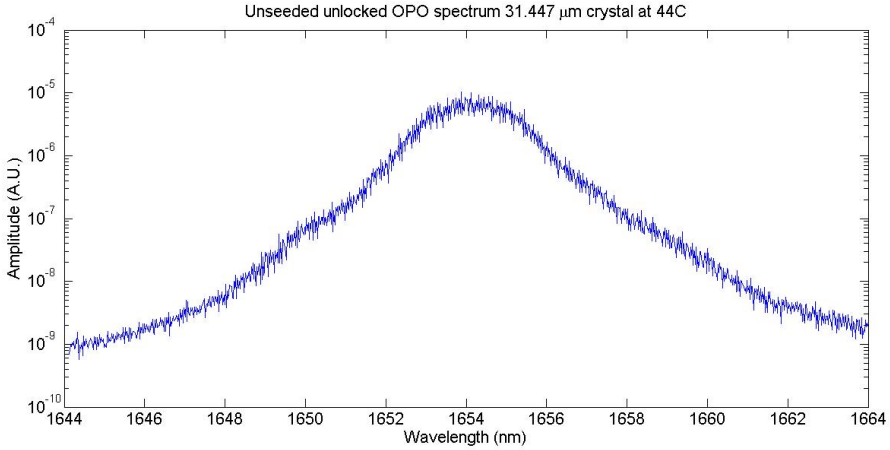


Figure 5.7: Spectrum from the unseeded unlocked OPO with pump energy of 2.5 mJ. The spectrum shown here is much broader than the spectrum in figure 5.6 due to the increased pump energy.

The spectrum from the unseeded unlocked OPO in figure 5.6 is plotted with a spectrum of the OPG output from chapter 3 as shown in figure 5.8 with the OPO spectrum shown in blue and the OPG spectrum shown in green. The OPG data were taken at 2.8 mJ of input pump energy with the crystal heated to 42°C, and the OPO data were taken at 2.5 mJ of input pump energy with the crystal heated to 44°C. The two spectra do not have the same peak wavelength, but this could be due to the optical cavity changing the path of the pump beam through the crystal so that it

experiences a different effective poling period. The FWHM of the OPO spectrum is 1.32 nm and is 7.67 nm for the OPG spectrum.

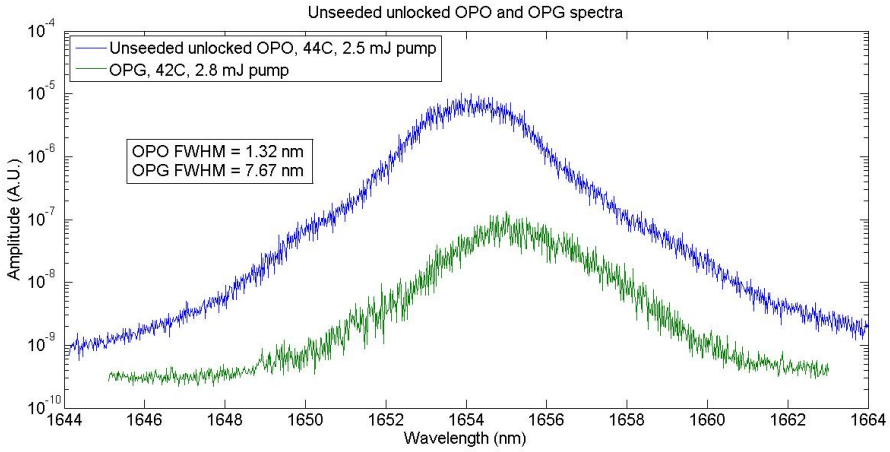


Figure 5.8: Unseeded unlocked OPO spectrum with 2.5 mJ pump energy and OPG spectrum with 2.8 mJ pump energy. The crystal temperature for OPG is 42°C and 44°C for the OPO. Both spectra show the bandwidth of signal wavelengths that can be generated based on phase-matching.

The output energy data from the unseeded unlocked OPO are shown in figure 5.9 along with the output energy data from OPG. The output energy from the unseeded unlocked OPO is larger than from OPG due to the optical cavity. Data shown in red represents the OPO output and blue represents the OPG output. The OPG data are from the data in chapter 3. The data in figure 5.9 indicate that the OPO cavity is increasing the efficiency of the nonlinear conversion process, which is what we expected.

The unseeded unlocked OPO performs better than the OPG as far as having more conversion to the signal wavelength. We saw about double the energy out of the OPO than the OPG, meaning that the optical cavity is having a significant impact on the conversion. The spectra are very similar, but the OPO spectrum is narrower than the OPG spectrum which may also be due to the cavity.

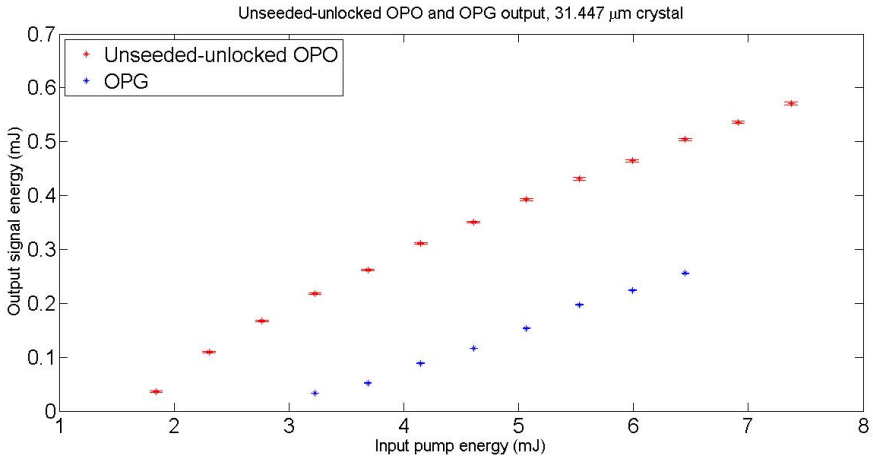


Figure 5.9: Unseeded unlocked OPO and OPG output energy. The OPO energy is about two times larger than the OPG energy, indicating that the optical cavity is causing an increase in output energy.

Seeded Unlocked OPO Data

In the case of the seeded unlocked OPO, the cavity is unlocked and the seed laser is turned on. Therefore we expect higher energy output at the seed laser wavelength at 1654 nm due to amplification in the nonlinear crystal compared to the unseeded OPO. However with the cavity still unlocked we still see a broadened spectrum from the OPO, as shown in figure 5.10. This plot shows the spectrum of the seeded unlocked OPO output (blue) compared to the spectrum of the seed laser (green). The OPO spectrum is narrower in this case than it was for the unseeded unlocked OPO with a FWHM of 0.16 nm for the seeded OPO compared to 1.32 nm for the unseeded OPO. However, we still see side modes on the OPO output due to the unlocked cavity.

An interesting feature of this spectrum is the dip in the OPO spectrum at the seed laser wavelength. Additional testing is needed to determine the cause of this feature; however, we suspect that it may be due to gain saturation or the shape of the seed laser spectrum. Seeding the unlocked OPO narrows the output of the

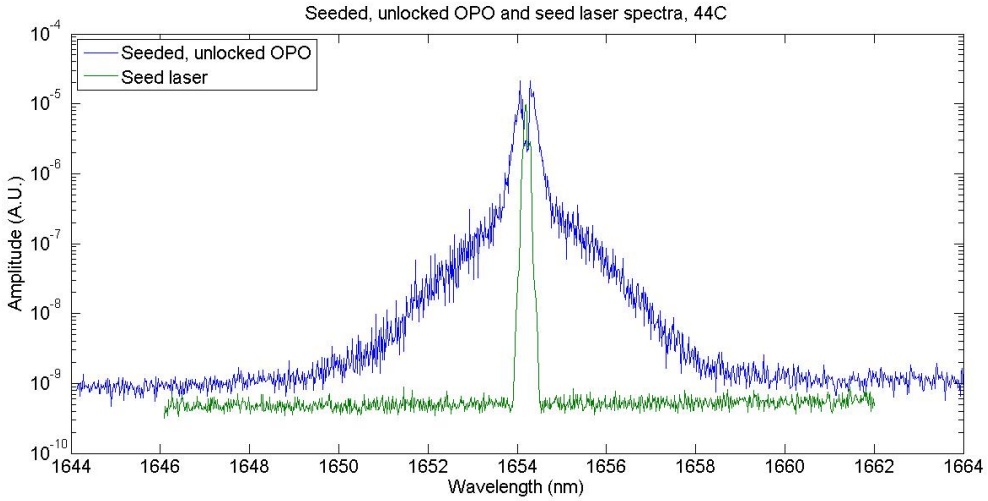


Figure 5.10: Seeded unlocked OPO spectrum. The output is narrower at the center than the unseeded OPO, but is still broad because the cavity is not locked and therefore the cavity length can change due to temperature fluctuations. Here the pump energy is 2.5 mJ and the FWHM of the OPO spectrum is 0.16 nm

spectrum, but the spectrum still shows unwanted side modes on the output. The output energy is comparable and is shown later in figure 5.18.

Seeded Locked OPO Data
with OPA Data Comparison

The seeded locked OPO uses the dither locking process described in chapter 4 to lock the OPO cavity so that it remains resonant with the seed laser. The four spectra shown in figures 5.11, 5.12, 5.13, and 5.14 show the unseeded OPO spectrum (green) to illustrate the bandwidth of signal wavelengths that are phase-matched, the seed laser spectrum (red), and the seeded locked OPO spectrum (blue) plotted together with input pump energies of 1.5 mJ, 2.5 mJ, 4.5 mJ, and 7 mJ, respectively. These spectra demonstrate how the output changes with increased pump energy.

From these figures we see that the increased pump energy tends to broaden the unseeded OPO spectrum and the seeded locked OPO spectrum. The seeded locked

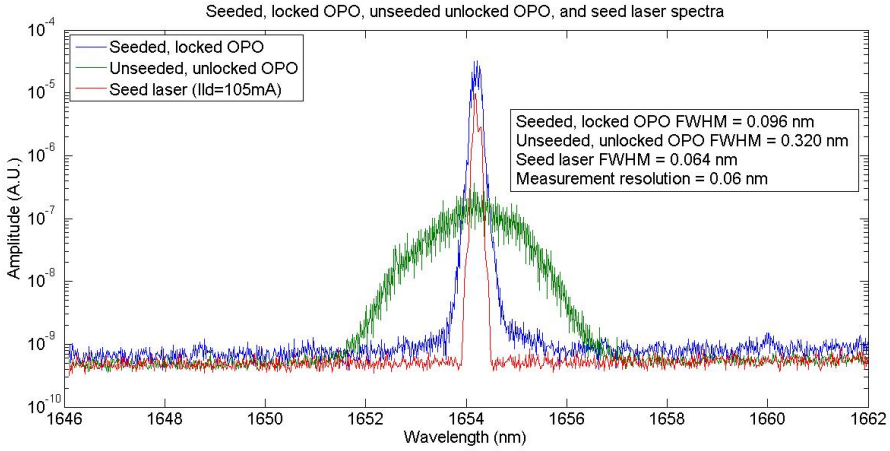


Figure 5.11: Seeded locked OPO output (blue), unseeded unlocked OPO output (green), and seed laser (red) spectrum. The pump energy into the OPO for both the seeded locked and unseeded unlocked output spectra is 1.5 mJ. By locking the OPO cavity, a very narrow spectral output can be achieved. The FWHM of the seeded OPO spectrum is 0.096nm, which is near the 0.06 nm resolution of the OSA.

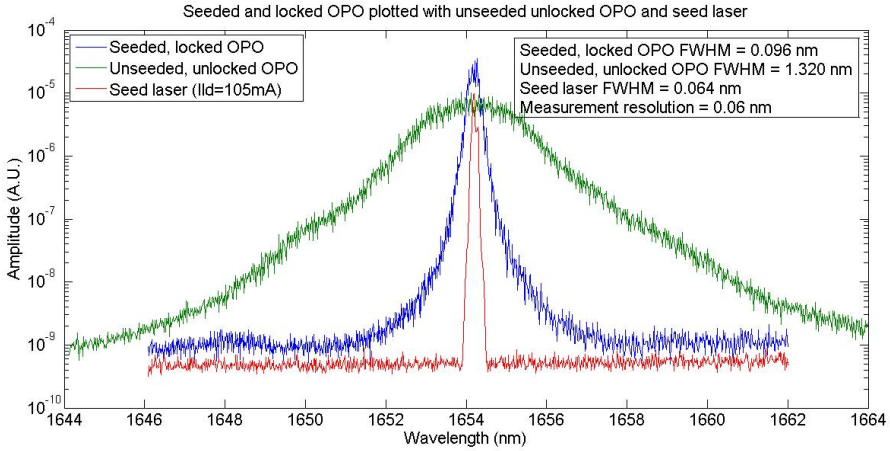


Figure 5.12: Seeded locked OPO output (blue), unseeded unlocked OPO output (green), and seed laser (red) spectrum. The pump energy into the OPO for both the seeded locked and unseeded unlocked output spectra is 2.5 mJ. The FWHM of the unseeded OPO is 1 nm larger than in figure 5.11 because of the increased pump energy. The FWHM of the seeded OPO is the same as in figure 5.11 at 0.096 nm, which is near the 0.06 nm resolution of the OSA.

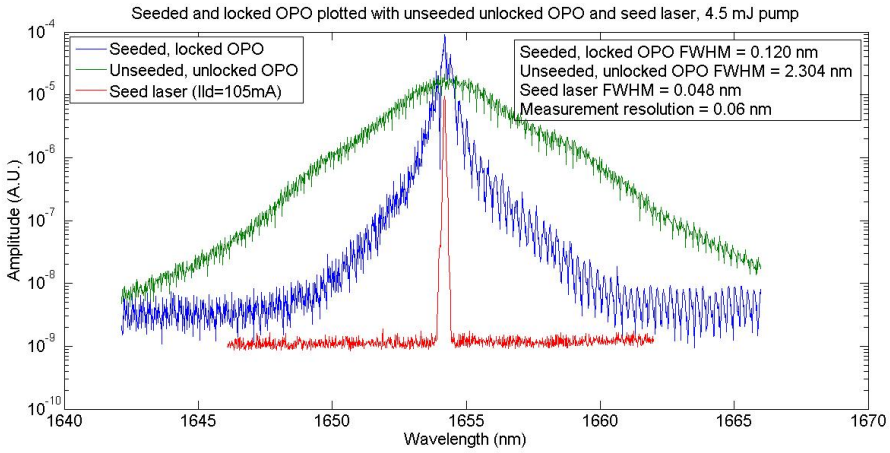


Figure 5.13: Seeded locked OPO output (blue), unseeded unlocked OPO output (green), and seed laser (red) spectrum. The pump energy into the OPO for both the seeded locked and unseeded unlocked output spectra is 4.5 mJ. Both the seeded and unseeded OPO spectra are broader at this higher pump energy. Here the unseeded OPO FWHM is 2.304 nm and the seeded OPO FWHM is 0.120 nm.

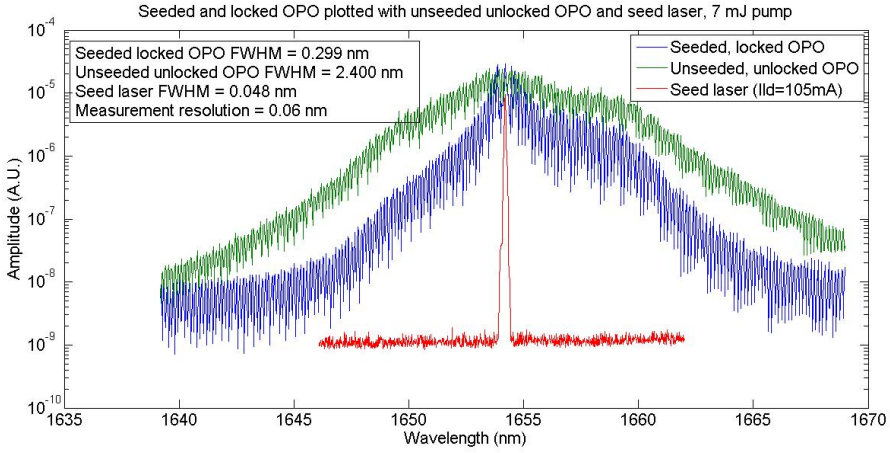


Figure 5.14: Seeded locked OPO output (blue), unseeded unlocked OPO output (green), and seed laser (red) spectrum. The pump energy into the OPO for both the seeded locked and unseeded unlocked output spectra is 7 mJ. The seeded OPO spectrum is beginning to broaden like the unseeded OPO spectrum. Higher seed power is necessary to keep the seeded OPO spectrum narrow.

OPO FWHM increased from 0.096 nm when the pump energy was 1.5 mJ to 0.299 nm when the pump energy was 7 mJ. The broadening of the seeded OPO spectrum is

due to the relatively low seed power used for the OPO (1 mW), which is not enough power to saturate the gain. More seed laser power is needed to saturate the gain produced by the pump beam at these higher energies, and will therefore results in a narrower output spectrum.

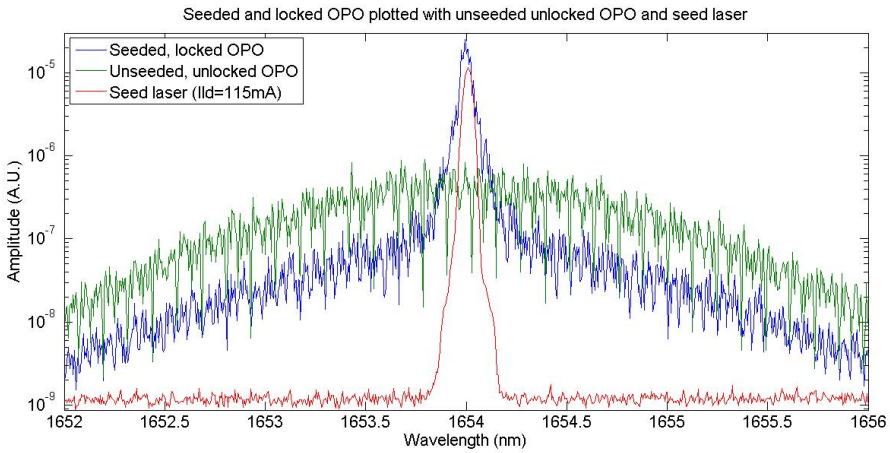


Figure 5.15: Seeded OPO spectrum shown with poor spatial overlap of the seed and pump beams. The result of poor spatial overlap is seen in the seeded locked OPO spectrum (blue), where the side mode suppression is small. Good spatial overlap would result in a narrow output at the seed laser wavelength. In this case however, there is good spectral overlap since the peak of the unseeded OPO spectrum (green) coincides with the peak of the seed laser spectrum (red).

As shown in chapter 3, we can look at the spectral output from the OPO to determine if the OPO is well-aligned. Figure 5.15 shows the output from the OPO when the pump and seed laser have poor spatial overlap. Good overlap would result in a very narrow spectrum for the seeded OPO, which is not the case here. From the spectrum it appears that only a small amount of the gain is used for conversion at the seed laser wavelength. We can see that this is a spatial overlap issue and not a spectral overlap issue because the peak of the unseeded OPO spectrum coincides with the peak of the seed laser spectrum.

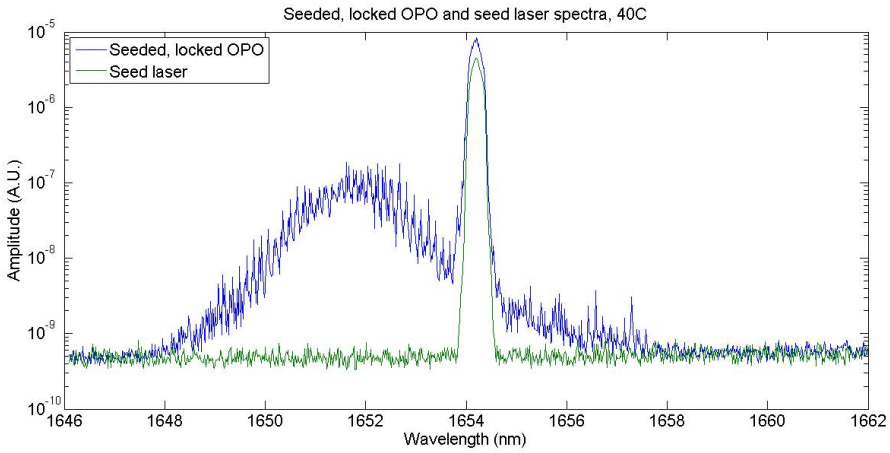


Figure 5.16: Seeded locked OPO spectrum exhibiting poor spectral overlap. The peak of the unseeded unlocked OPO spectrum (not shown) does not line up with the peak of the seed laser spectrum, resulting in a seeded locked OPO spectrum that has a broad side feature. The asymmetry in the seeded locked OPO spectrum demonstrates the poor spectral overlap in the setup.

Figure 5.16 shows how the output changes when the crystal is not heated to the right temperature to get good phase-matching at the seed laser wavelength. The figure shows the seed laser spectrum in blue and the seed laser spectrum in green. The seeded OPO spectrum has a tall, narrow peak along with a broad side mode. The fact that the tall peak is located on the side of the broad signal indicates that this is poor spectral overlap. With good spectral overlap, the peak would occur at the center of the broad signal. Changing the crystal temperature will correct this which will increase the conversion at the seed laser wavelength.

The spectral output from the system at 1654 nm is highly dependent on the input pump energy and the seed laser power, as well as the spatial and spectral overlap in the system. A higher-power seed laser would make a narrower spectrum at higher pump energies, which may be necessary for use of the OPO as the DIAL laser transmitter in order to maintain the narrow linewidth as the signal energy increases.

	Signal	Idler	Pump
Wavelengths (nm)	1654	2982.8	1064
Indexes of refraction	2.204863	2.159973	2.228959
Crystal left reflectivity	0	0	0
Crystal right reflectivity	0	0	0
Crystal loss (per mm)	0	0	0
Enrgy/Pwr left (J/W)	0.0005	0	8E-3
Enrgy/Pwr right (J/W)	0	0	
Pulse duration (ns)	0	0	10
Pulse delay (ns)	0	0	
Beam diameter (FWHM mm)	0.871	0.871	0.871
Supergaussian coefficient	1	1	3
Walk off angle (mrad)	0	0	0
Beam offset (mm)		0	0
Beam radius of curv. (mm)	3.08E2	3.08E2	3.08E2
Left mirror reflectivity	0.95	0.3	0.3
Right mirror reflectivity	0.45	0.3	0.2
Phase L-C (radians)	0	0	0
Phase C-R (radians)	0	0	0
Phase R-L (radians)	0	0	0
Mirror roc L R (mm)	1.00E10	5.00E2	
Dist. L-C C-R R-L (mm)	20	70	0
Grid numbers z x y	30	32	32
Crystal/grid sizes (mm)	30	4.355	4.355
Cavity type/inversion	1	0	
deff (pm/V)/delta k (1/mm)	15.9	0.209	Accept

Figure 5.17: Inputs for the SNLO modeling program for 2D gaussian beam mixing in an OPO cavity. The supplied parameters were determined with the best measured and estimated data from the system. The values for d_{eff} and Δk were found from the best-fit to the OPA data from chapter 3.

Finally, we looked at the energy that the OPO produces at 1654 nm. Figure 5.18 shows the energy output for the unseeded unlocked OPO, seeded unlocked OPO, and seeded locked OPO. These data are plotted with the SNLO model using the known parameters from the system as shown in the SNLO inputs table in figure 5.17. The parameters used in the program are determined from the nominal values and from measured values. For instance, the beam diameter was measured for the pump beam, but we do not have the equipment to measure the signal beam diameter, so we assumed they were the same as the pump. Also, the mirror reflectivities are inferred from the datasheets from the mirror manufacturer. The values of d_{eff} and Δk were taken from the best-fits in figure 3.8b on page 43. The SNLO model is shown as a

solid line, the unseeded unlocked OPO is shown in blue, the seeded unlocked OPO is shown in green, and the seeded locked OPO is shown in red.

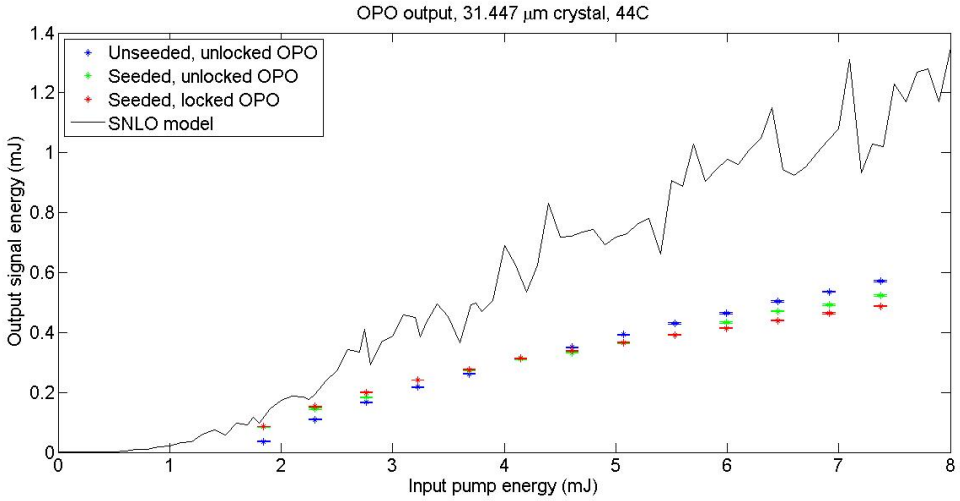


Figure 5.18: Measured output signal energy as a function of input pump energy for the three OPO's. The SNLO model is also shown as the solid line. Initially the seeded locked OPO has the highest output energy, but at higher input pump energies it has the lowest output energy. This is likely due to the broadening of the spectra at higher pump energies, which may be corrected with a higher-power seed laser. The SNLO model is about two times larger than the measured outputs, which is reasonable since SNLO assumes a best-case output based on the supplied parameters.

An important feature to note from figure 5.18 is that the seeded locked OPO has the highest output energy at low pump inputs but at higher pump inputs it has the lowest energy of the three OPOs. The reason for this may be found from the spectra shown in figures 5.11, 5.12, 5.13, and 5.14. Around 4.5 mJ of input pump energy, the spectrum of the unseeded unlocked OPO changes significantly and becomes much more broadband and only gets more broadband as the pump energy is increased. With the cavity locked to the signal wavelength, not all of the generated signal light can transmit through the cavity. However, in the case of the unlocked OPO, nearly all of the generated signal light can leave the cavity, resulting in more energy out of

the cavity. A higher-power seed laser may help with this problem because it could saturate the gain at higher pump energies and result in more signal light to leave the cavity in the case of the locked OPO. More testing is needed to determine if a higher-power seed laser would correct this problem.

It is clear that the SNLO model doesn't match the OPO data within error and it is nearly a factor of 2 greater than the actual data. Some reasons for this mismatch could include that SNLO assumes a best-case scenario, the fact that we don't have perfect coupling of the seed laser into the optical cavity, the high-spatial mode pump beam isn't modeled properly in SNLO, mirror absorption, and crystal losses. Understanding this mismatch is part of the future work for this project, but as a proof of concept we take the factor of 2 difference to be reasonable.

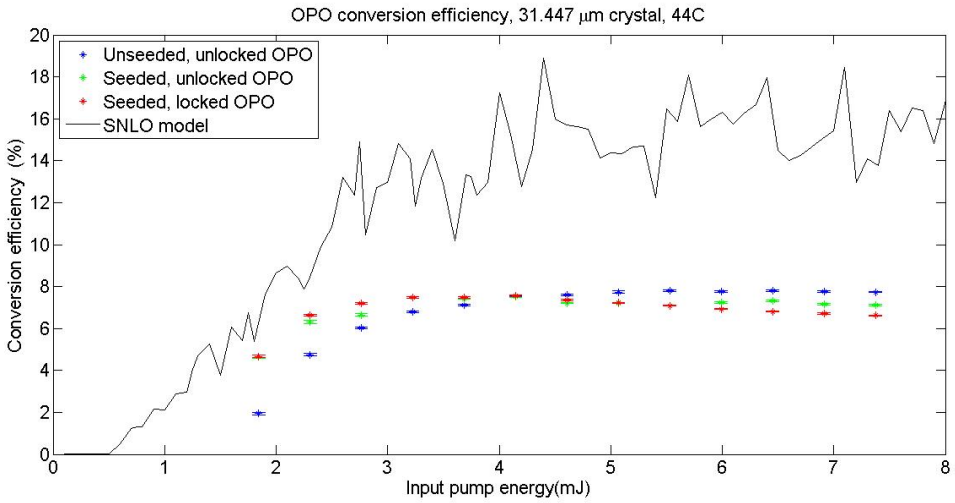


Figure 5.19: Measured conversion efficiency of the unseeded unlocked OPO, seeded unlocked OPO, and seeded locked OPO compared to the SNLO model. Conversion efficiency was calculated from the data from figure 5.18. Here we see the SNLO conversion efficiency reaches about 16% and the experimental results reach about 8%, which is reasonable since SNLO provides a best-case output.

Figure 5.19 shows the conversion efficiency determined from the same data. Conversion data are calculated by dividing the output energy by the input energy to

get a percentage of efficiency for the conversion. These data show that the OPO is achieving about 8% conversion efficiency. Again the SNLO model is about twice the output of the measured results due to SNLO assuming a best-case scenario.

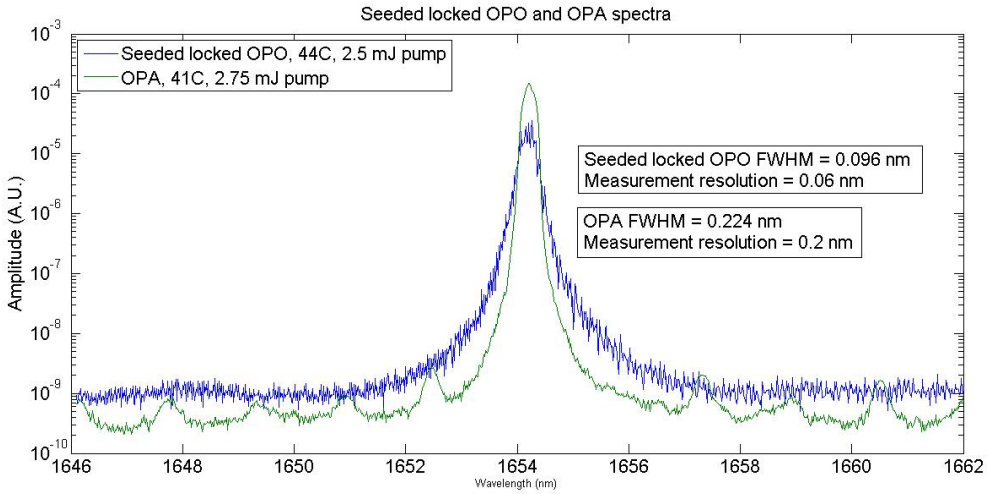


Figure 5.20: Seeded locked OPO spectrum (blue) and OPA spectrum (green). The FWHM of each spectrum is on the order of the measurement resolution. Note that the seed laser power for OPA is 4.5 mW and only 1 mW for the OPO, which may indicate that the OPO requires less seed power to achieve a narrow spectrum. The input pump energy for the OPO is 2.5 mJ and is 2.75 mJ for the OPA.

The spectrum of the OPO compared to the spectrum from OPA is shown in figure 5.20. The OPA spectrum was taken from the data shown in chapter 3. The FWHM from the seeded locked OPO is 0.096 nm (0.06 nm measurement resolution), while the FWHM from OPA is 0.224 nm (0.2 nm measurement resolution), corresponding to 10.5 GHz and 24.5 GHz, respectively. The FWHM from each spectrum is on the order of the measurement resolution of the OSA. Therefore, more precise equipment is needed to determine the actual width of these spectra and if the OPO spectrum is narrower than the OPA spectrum. The OPO spectrum was taken at pump energy of 2.5 mJ, while the OPA spectrum had an input pump energy of 2.75 mJ. An important difference between the data shown is that the seed laser

power for OPA was 4.5 mW while it was only 1 mW for the OPO data. (The loss in the seed laser power is due to the addition of the AOM.) Therefore both spectra have widths on the order of the OSA resolution, but the OPO had only 20% of the seed laser power of the OPA had, which may indicate that the OPO requires less seed power to get a narrow spectrum. More research and an OSA with higher resolution is required to confirm this.

The main reason for building the OPO was to try to get higher output than the OPA. The OPO generates a narrow spectrum like the OPA, but it also produces more energy as shown in figure 5.21. This figure shows the output energy at the signal wavelength for the seeded locked OPO compared to the OPA output energy taken from chapter 3. Here we see that the output energy from the OPO is about two times higher than the OPA output energy, indicating that the optical cavity increases the amount of conversion in the nonlinear process.

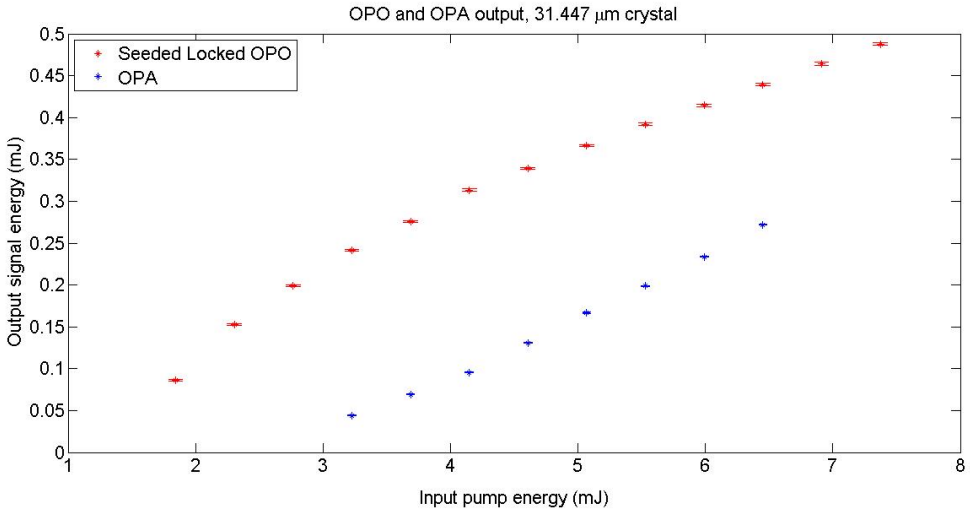


Figure 5.21: Measured output energy from the seeded locked OPO (red) and the OPA (blue). The OPO output energy is about two times greater than the OPA energy, indicating that the optical cavity leads to increased conversion at the signal wavelength.

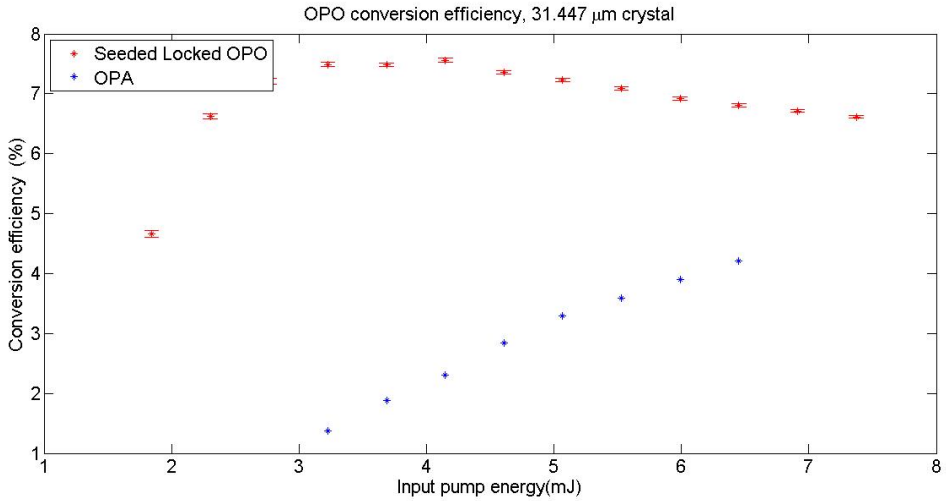


Figure 5.22: Measured conversion efficiency of the seeded locked OPO and the OPA, taken from the data in chapter 3. The conversion efficiency of the OPO reaches a maximum near 7% and levels out, while the OPA conversion efficiency reaches a maximum near 4%. Higher input pump energies are necessary to determine the maximum level that the OPA can achieve.

Figure 5.22 shows the conversion efficiency from the same data. The OPA data are taken from chapter 3. Conversion efficiency is calculated by dividing the output signal energy by the input pump energy. From this plot we see that the OPO conversion efficiency levels out near 7% and the OPA conversion efficiency reaches a maximum near 4% conversion. To determine the steady-state conversion efficiency of the OPA, data at higher pump energies are necessary.

From this data it is clear that the OPO cavity results in higher conversion to 1654 nm than the OPA. The maximum energy achieved from the OPO is about 0.5 mJ, while the maximum energy from the OPA is about 0.25 mJ. This makes the OPO a much better choice for the DIAL laser transmitter. Additionally, the spectral output from the OPO had a FWHM of 0.096 nm, which is close to the resolution of the OSA of 0.06 nm. The OPA spectral output has a FWHM of 0.224 nm with an input pump energy of 2.75 mJ, where the OSA resolution was 0.2 nm. Therefore both the

OPO FWHM and OPA FWHM are on the limit of the resolution of the measurement and equipment with higher resolution is needed to determine if the OPO results in a narrower spectrum compared to OPA.

The seeded locked OPO has the narrowest spectrum when the pump energy is low, on the order of 1.5 mJ. At this input pump energy, the energy at the signal wavelength is less than 0.1 mJ and is too low to be useful as a DIAL laser transmitter. Use of a higher-power seed laser would keep the spectrum narrow, even at high pump energies. Additionally, further optimization of the cavity including better mode-matching and choice of cavity mirrors could also assist in generating more output energy while keeping the spectrum narrow.

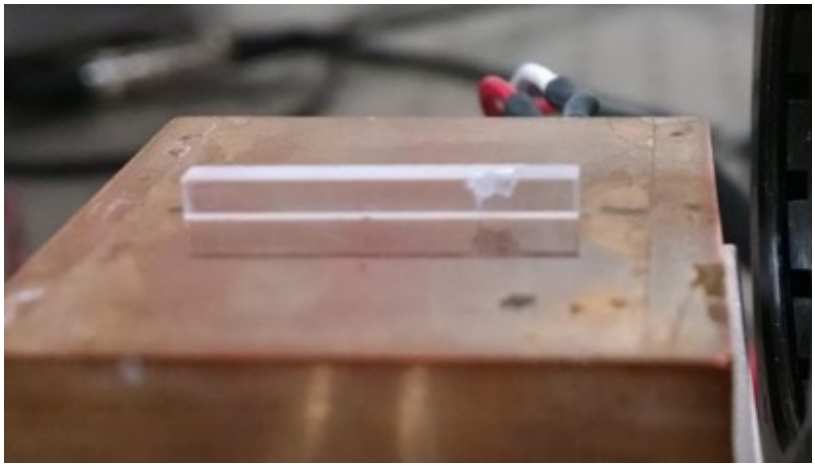


Figure 5.23: Optical damage to the PPLN crystal in an OPO. The input pump energy was about 15 mJ when the damage occured.

The OPO output needs to increase by about 6 times in order to meet the levels needed for DIAL measurements. Improvements include better mode-matching of the seed laser into the cavity and testing at increased pump energies. We must however be careful of damaging the crystal with increased energy. Previous testing of an OPO at high input pump energies resulted in optical damage to a PPLN crystal. This damage

is shown in figure 5.23, which was caused when the OPO was pumped at about 15 mJ. Crystal damage occurs from high intensities in the PPLN crystal, which depends on the area of the beam. Future work in optimization of the OPO will also focus on selecting beam diameters that will generate enough output energy at 1654 nm and also avoid damage to the crystal.

CONCLUSION

The goal of this work was to develop and test the potential of an OPO for use as the laser transmitter in a DIAL system. Requirements for the system includes an output energy of 3 mJ at 1654 nm with a repetition rate of 1 kHz and a linewidth of 3 MHz. Our results indicate that an OPO will be the best choice for the laser transmitter due to its high output energy at 1654 nm and narrow linewidth.

Nonlinear optical processes can be modeled through the use of the coupled wave equations, which can be solved with numerical integration or directly through the use of the non-depleted pump approximation. This is relatively straightforward for calculating OPA and OPG, but becomes significantly more challenging when trying to model how the optical cavity changes the conversion in the case of the OPO. A nonlinear modeling program called SNLO was used extensively in this project because it calculates the outputs from nonlinear conversion processes, including the OPO, even with focused beams. We tested the SNLO model by comparing its output of the OPA to the plane-wave output from the coupled wave equations. We found that the two models resulted in outputs that differed by less than 10%, which could be due to differences in how each model handles the supplied parameters. However, we are confident that SNLO will provide accurate results for which to compare the measured OPO results.

To understand the performance of the OPO, the outputs from OPG and OPA were first studied. We observed that injection seeding an OPG, which results in OPA, increases the output energy and reduces the spectral linewidth, especially at low input pump energies. The importance of good spatial and spectral overlap in the nonlinear crystal was also observed. Fitting the SNLO model to OPA data also generated estimates of d_{eff} and Δk that could be used for the OPO model. We found

from this fit that d_{eff} is between 15 and 16 pm/V and Δk is between 200 and 300 1/m.

Locking the optical cavity is required to maintain a narrow spectral output from the OPO. This was done with a process called dither locking, where the seed laser wavelength is dithered and the amount of seed laser light that exits the cavity is measured to determine if the laser is on-resonance or off-resonance of the optical cavity. With the addition of a shutter circuit, which ignores large signal pulses from the nonlinear conversion process, we were able to achieve cavity locking for long periods of time even with mechanical disturbances. This is important since the OPO will need to lock for long periods of time for DIAL measurements.

The OPO was tested and compared to the data from the OPG and OPA. Testing was performed while the OPO was seeded locked, seeded unlocked, and unseeded unlocked. The seeded locked OPO produced the narrowest spectral output, even at high input pump energies, making it the most promising for use as a DIAL laser transmitter. It also produced the highest output energy, but only at low input pump energies, which may be due to the broadening of the spectral output. Increased seed laser power may help with this issue. When the seeded locked OPO is compared to the results of OPA, we find that the OPO produces about two times the output energy than OPA, indicating that the optical cavity is increasing the conversion to the signal wavelength. The seeded locked OPO produced a maximum measured output energy near 0.5 mJ, but increasing the input pump energy could potentially result in output energies closer to the 3 mJ necessary for the DIAL laser transmitter.

Future work includes optimization of the OPO cavity to increase the conversion to the signal wavelength. Better mode-matching with the seed laser as well as increased input pump energies may be enough to generate the output energy needed for the DIAL laser transmitter. Additionally, a narrower spectral output is needed,

which may be achieved with a higher-power seed laser. This requires further testing as well as new equipment that has enough resolution to measure linewidths on the order of 3 MHz. The OSA used to measure the spectral linewidth has a maximum resolution of 0.06 nm, corresponding to 66 GHz linewidth, which isn't enough to measure the 3 MHz linewidth needed. Additionally, the OPO we built operated at a 20 Hz repetition rate and a 1 kHz repetition rate is needed for the laser transmitter. Future work will also require a 1 kHz pump laser for the OPO.

Overall, the results from the OPO show promise for its use as a DIAL laser transmitter. With the improvements mentioned above, the system has potential to meet the requirements of the DIAL system.

REFERENCES CITED

[1] "Inventory of U.S. greenhouse gas emissions and sinks: 1990 - 2013," tech. rep., U.S. Environmental Protection Agency, April 2015.

[2] S. Solomon, D. Qin, M. Manning, Z. Chen, M. Marquis, K. B. Averyt, and M. T. H. M. (eds.), "IPCC, 2007: Climate change 2007: The physical science basis. contribution of working group I to the fourth assessment report of the intergovernmental panel on climage change," tech. rep., Cambridge University Press, Cambridge, United Kingdom and New York, NY, USA, 2013.

[3] J. Butler and S. Montzka, "The NOAA annual greenhouse gas index (AGGI)," tech. rep., NOAA Earth system research laboratory, 2015.

[4] C. Nagasawa, M. Abo, Y. Shibata, T. Nagai, and M. Tsukamoto, "Direct detection of 1.6 μm dial for measurements of CO_2 concentration profiles in the troposphere," in *Proceedings SPIE 8182, Lidar Technologies, Techniques, and Measurements for Atmospheric Remote Sensing VII, 81820G, doi:10.1117/12.898784*, 2011.

[5] W. Johnson, K. S. Repasky, and J. L. Carlsten, "Micropulse differential absorption lidar for identification of carbon sequestration site leakage," *Applied Optics*, vol. 53, pp. 2994 – 3003, 2013.

[6] L. Rothman, A. Barbe, D. Benner, L. Brown, C. Camy-Peyret, M. Carleer, K. Chance, C. Clerbaux, V. Dana, V. Devi, A. Fayt, J. Flaud, R. Gamache, A. Goldman, D. Jacquemart, K. Jucks, W. Lafferty, J. Mandin, S. Massie, V. Nemtchinov, D. Newnham, A. Perrin, C. Rinsland, J. Schroeder, K. Smith, M. Smith, K. Tang, R. Roth, J. V. Auwera, P. Varanasi, and K. Yoshino, "The HITRAN molecular spectroscopic database," *Journal of Quantitative Spectroscopy and Radiative Transfer*, vol. 82, pp. 5 – 44, 2003.

[7] T. Refaat, S. Ismail, A. Nehrir, J. Hair, J. Crawford, I. Leifer, and T. Shuman, "Performance evaluation of a 1.6 μm methane dial system from ground, aircraft and UAV platforms," *Optics Express*, vol. 21, pp. 30415 – 30432, 2013.

[8] R. Boyd, *Nonlinear Optics*. Academic Press, third ed., 2008.

[9] A. Yariv, *Quantum Electronics*. John Wiley and Sons, Inc., third ed., 1989.

[10] D. H. Jundt, "Temperature-dependent Sellmeier equation for the index of refraction, n_e, in congruent lithium niobate," *Optics Letters*, vol. 22, pp. 1553 – 1555, 1997.

[11] P. Hermet, M. Veithen, and P. Ghosez, "First-principles calculations of the nonlinear optical susceptibilities and raman scattering spectra of lithium niobate," *Journal of Physics: Condensed Matter*, vol. 19, 2007.

[12] A. V. Smith, "How to select nonlinear crystals and model their performance using SNLO software," tech. rep., Sandia National Laboratories.

[13] K. Kuhn, *Laser Engineering*. Prentice Hall, first ed., 1998.

[14] E. Black, "An introduction to Pound-Drever-Hall laser frequency stabilization," *American Journal of Physics*, vol. 69, January 2001.

[15] F. L. Pedrotti, L. S. Pedrotti, and L. M. Pedrotti, *Introduction to Optics*. Prentice Hall, third ed., 2007.

APPENDIX A

MATLAB OPA PROGRAM

```
%Program that numerically integrates the coupled wave equations
    and finds the output energy of each wave as a function of
    input pump energy for OPA. The program also compares the
    results of the numerical integration to the case of non-
    depleted pump.
%Briana Jones
%Last edit: September 18, 2015

format long
%Parameters----------------------------------
numsteps = 100000; %number of steps in the numerical integration
numpass  = 1; %number of passes through crystal
d = numsteps/numpass; %number of divisions of crystal (for loop
    calculations)
                          %must be greater than one

As = zeros(numsteps,1);       %Vector of zeros for signal amplitude
Aistar = zeros(numsteps,1); %Vector of zeros for complex idler
    amplitude
Ap = zeros(numsteps,1);       %Vector of zeros for pump amplitude
time = zeros(numsteps,1);     %Vector of zeros for time
EsDep = zeros(1,100);         %Vector of zeros for output signal
    energy
PsDep = zeros(1,100);         %Vector of zeros for output signal
    power
EiDep = zeros(1,100);         %Vector of zeros for output idler
    energy
```

```
PiDep = zeros(1,100);          %Vector of zeros for output idler
    power
EpDep = zeros(1,100);          %Vector of zeros for output pump
    energy
PpDep = zeros(1,100);          %Vector of zeros for output pump
    power
Epump = [0.04:0.04:4];         %Input pump energy (must be 100
    elements)
%-----------------------------------------
```

```
%Constants-------------------------------
u0 = 1.26e-6;    %Vacuum permeability (Js2/mC2)
e0 = 8.85e-12;   %Vacuum permittivity (C2/Jm)
c = 3.0e8;       %Speed of light (m/s)
deff = 1.31e-22;%d effective (C3/J2) (to convert to m/V, divide
    by e0)
pulsewidth = 10e-9; %Width of laser pulse (s)
L    = .02;      %length of crystal (m)
n = 2.2; %index of refraction, assumed constant for each
    wavelength

lambdas = 1.65e-6;  %Wavelength of signal beam (m)
lambdai = 2.995e-6; %Wavelength of idler beam (m)
lambdap = 1.064e-6; %Wavelength of pump beam (m)

ws = (2*pi*c)/lambdas; %Angular frequency for signal (1/s)
```

```
wi = (2*pi*c)/lambdai; %Angular frequency for idler (1/s)
wp = (2*pi*c)/lambdap; %Angular frequency for pump (1/s)

k=deff*(sqrt((u0*ws*wi*wp)/(e0*n^3))); %Gain term, kappa (C/Js
    ^.5)

Abs = (pi)*(0.000671)^2; %Signal beam area (m2)
Abp = (pi)*(0.000671)^2; %Pump beam area (m2)
%-----------------------------------------------------

%Initial conditions-----------------------------------------------
Ps0 = 0.001;      %Input signal power (W)
Pi0 = 0.00;       %Input idler power (W)
As(1) = sqrt(((2*Ps0)/(Abs*ws))*(sqrt(u0/e0)));      %Starting
    amplitude for signal (Js^.5/mC)
Aistar(1) = sqrt(((2*Pi0)/(Abs*wi))*(sqrt(u0/e0))); %Starting
    amplitude for idler (Js^.5/mC)
%-----------------------------------------------------------------

%Code that calculates the output energies for all waves
for E = 1:1:100 %Index for energy increments

Ppeak = 0.94*(Epump(E)/1000)/pulsewidth; %Convert from energy to
    power (W)
```

```
Ap(1) = sqrt(((2*Ppeak(1))/(Abs*wp))*(sqrt(u0/e0))); %Initial
    value of Ap
%This 'for loop' calculates the output energy as a function of
    input pump
%energy
for z = 2:1:numsteps
    dt      = L/(d*c); %breaks up the crystal into time integers
        for integration
    time(1) = dt;
    time(z) = z*dt;

    dAs     = (-1i*k*c*Ap(z-1)*Aistar(z-1)*dt);
    dAistar = 1i*k*c*conj(Ap(z-1))*As(z-1)*dt;
    dAp     = -1i*k*c*As(z-1)*conj(Aistar(z-1))*dt ;

    As(z)     = As(z-1) + dAs;
    Aistar(z) = Aistar(z-1) + dAistar;
    Ap(z)     = Ap(z-1)  + dAp;

    %This 'for loop' numerically integrates the coupled wave
        equations through
%the crystal. The output energy can be determined from this.
end


PsDep(E) = (abs(As(z)^2))*(Abs*ws/2)*(sqrt(e0/u0));              %
    Output signal power (W) (depleted pump approx)
```

```
EsDep(E) = PsDep(E)*pulsewidth*1000;                                    %
    Output signal energy (mJ) (depleted pump approx)

PiDep(E) = (abs(conj(Aistar(z)))^2)*(Abs*wi/2)*(sqrt(e0/u0));           %
    Output idler power (W) (depleted pump approx)
EiDep(E) = PiDep(E)*pulsewidth*1000;                                    %
    Output idler energy (mJ) (depleted pump approx)

PpDep(E) = (abs(Ap(z)^2))*(Abp*wp/2)*(sqrt(e0/u0));                     %
    Output pump power (W) (depleted pump approx)
EpDep(E) = PpDep(E)*pulsewidth*1000;                                    %
    Output pump energy (mJ) (depleted pump approx)
end
%-------------------------------------------------------------------


%This part of the code calculates the output for the signal and
    idler in the case of non-depleted pump approximation
PpeakNondep = 0.94*(Epump./1000)./pulsewidth;                           %
    Conversion from input pump energy to peak pump power (W)
ApNondep = sqrt(((2*PpeakNondep)./(Abs*wp))*(sqrt(u0/e0)));  %Pump
     amplitude input (Js^.5/mC)
AsNondep = As(1).*(cosh(k.*ApNondep.*L));                               %
    Signal amplitude output (Js^.5/mC)
AiNondep = 1i*As(1).*(sinh(k.*ApNondep.*L));                            %
    Idler amplitude output (Js^.5/mC)
```

```
PsNondep = (abs(AsNondep.^2))*(Abs*ws/2)*(sqrt(e0/u0)); %
    Signal power output (W)
EsNondep = PsNondep*pulsewidth*1000; %
    signal energy output (mJ)
%-----------------------------------------------------------------


%Figures-----------------------------------------------------------
figure
plot(Epump, EsDep, 'green', Epump, EsNondep, 'blue')
title('Comparison of OPA output for depleted and non-depleted
    pump calculations')
xlabel('Input pump energy (mJ)')
ylabel('Output signal energy (mJ)')
legend('Depleted pump solution','Non-depleted pump solution')
legend('location','northwest')

difference = EsNondep - EsDep;

figure
plot(Epump, difference)
title('Difference between depleted and non-depleted pump outputs'
    )
xlabel('Input pump energy (mJ)')
ylabel('Non-depleted pump solution - depleted pump solution (mJ)'
    )
```

```
figure
plot(Epump, EsDep, 'green')
title('Depleted pump solution for OPA')
xlabel('Input pump energy (mJ)')
ylabel('Output signal energy (mJ)')

figure
plot(Epump, EsNondep, 'blue')
title('Non-depleted pump solution for OPA')
xlabel('Input pump energy (mJ)')
ylabel('Output signal energy (mJ)')
%-------------------------------------------------------------------------
```